

**Characterizing Electrode-Level Oxygen Transport in Polymer Electrolyte Fuel
Cells**

Submitted in partial fulfillment of the requirements for
the degree of
Doctor of Philosophy
in
Mechanical Engineering

William K. Epting

B.S., Mechanical Engineering, University of Pittsburgh (2009)

M.S., Mechanical Engineering, Carnegie Mellon University (2011)

Carnegie Mellon University
Pittsburgh, PA

August 2015

© Copyright by William K. Epting 2015

All Rights Reserved

Carnegie Mellon University

CARNEGIE INSTITUTE OF TECHNOLOGY

THESIS

SUBMITTED IN PARTIAL FULFILLMENT OF THE REQUIREMENTS

FOR THE DEGREE OF Doctor of Philosophy

TITLE Characterizing Electrode-Level Oxygen Transport in Polymer
Electrolyte Fuel Cells

PRESENTED BY William K. Epting

ACCEPTED BY THE DEPARTMENT OF

Mechanical Engineering

ADVISOR, MAJOR PROFESSOR

DATE

DEPARTMENT HEAD

DATE

APPROVED BY THE COLLEGE COUNCIL

DEAN

DATE

Abstract

Polymer electrolyte fuel cells (PEFCs) are a promising technology for environmentally friendly automobiles, among other applications. However, performance losses due to oxygen transport hindrances in the PEFC's cathode continue to be an issue in widespread commercialization. This dissertation focuses on the transport of oxygen through the thickness of the PEFC cathode, and the effect of the cathode's microstructure on that transport. In order to react in the cathode, oxygen travels from gas flow channels down through a diffusion medium, through the pores of a catalyst layer, and finally, into and through the ionomer covering the catalyst particles. Transport resistances throughout this path lead to oxygen starvation at some of the catalyst particles. Due to these transport resistances, much of the platinum is underutilized when the fuel cell is operating at appreciable currents.

This dissertation aims to characterize the transport resistance in each of these phases. We study (1) oxygen transport throughout the diffusion medium using a commercial electrochemical microsensor at multiple points, (2) oxygen transport through the entire diffusion medium using a thin film oxygen microsensor at one point, (3) transport through the catalyst layer pores using a device that allows oxygen microsensors to contact the side of the catalyst layer at multiple points, (4) the effect of the catalyst layer's microstructure on oxygen transport using x-ray computed tomography, and (5) transport into and through ionomer-covered catalyst agglomerates using ex-situ experiments. We go on to discuss the application of similar methods to solid oxide fuel cells.

Using the methods developed in this work, we determine that the two dominant oxygen transport resistances are the diffusion medium, and a "local" resistance at the interface of the platinum catalyst and the ionomer binder that has previously generated some controversy in the field. The oxygen transport resistance of the diffusion medium in this work (defined as the ratio of the drop in concentration across a component to the flux through it) is 65 s/m, with about 2/3 of that coming from its microporous layer. This value can rise to double or more in the case of liquid water condensation in the diffusion medium's pores. We find that the oxygen transport resistance in the catalyst layer's pores is an order of magnitude less than that of the diffusion medium. That value, too, can change depending on liquid water flooding.

In previous works, the “local” oxygen transport resistance at the level of the platinum catalyst and ionomer binder was of unclear origin. We have determined that it arises at the Pt|ionomer interface – it does not originate from the ionomer|gas interface, nor is it due to nanoscale confinement effects. In our investigation of the catalyst layer’s morphology, we find that a popular approach to modelling PEFC performance – the agglomerate model – changes significantly when one incorporates a realistic distribution of agglomerate sizes instead of assuming a uniform agglomerate size. This effect, however, is small compared to the oxygen transport resistance of the diffusion medium oxygen resistance and the Pt|ionomer interfacial oxygen resistance.

Acknowledgements

First and foremost, I gratefully acknowledge my advisor, Prof. Shawn Litster, for the unending positive support, wisdom, creative input, and productive and energizing back-and-forth brainstorming sessions throughout my time at Carnegie Mellon University.

My colleagues within Shawn's Transport Phenomena in Energy Systems research group also deserve recognition for frequent, productive discussions and helpful guidance. Every member of this group deserves recognition, but in my particular case, Katherine C. Tully (née Hess), Hang Liu, Siddharth K. Babu, Pratiti Mandal, Seong Jin An, Iryna Zenyuk, and Michael B. Burkholder provided many useful discussions and productive collaboration. I also would like to acknowledge additional co-authors and collaborators from the work in this dissertation: Jeff Gelb, Joseph Suhan, Yu-Ting "Tim" Hsu, Prof. Kunal Karan, Zachary Mansley, Prof. Paul A. Salvador, Kirk Gerdes, David Menasche, Peter Kenesei, and Prof. Robert M. Suter. I also acknowledge the productive advice and guidance offered by my thesis committee, Prof. Jonathan A. Malen, Prof. Paul J. Sides, and Prof. Laura A. Schaefer.

I also thank the mechanical engineering department machinists Edward R. Wojciechowski, James Dillinger, and John Fulmer for assistance, advice, and fabrication of some of the experimental equipment in this work. All of the administrative staff at Carnegie Mellon University has also been extremely helpful throughout my time here as well.

I gratefully acknowledge the financial support of the National Science Foundation, the Department of Energy, the National Energy Technology Laboratory, and the Environmental Protection Agency for a 3-year EPA-STAR fellowship. None of these institutions have formally reviewed this publication; the views expressed in it are solely those of the author. The NSF, DOE, NETL, and EPA do not endorse any products or commercial services mentioned herein.

Finally, I could never have made it to where I am today without the unending support of my loving family and friends. Thank you all.

Table of Contents

Abstract.....	iii
Acknowledgements.....	vii
Table of Contents.....	viii
List of Tables.....	xi
List of Figures.....	xii
1 Introduction.....	1
1.1 Background: Polymer Electrolyte Fuel Cells.....	2
1.1.1 Oxygen Transport in PEFC Cathodes.....	5
1.2 Background: Solid Oxide Fuel Cells.....	8
1.3 Relevant Work.....	9
1.3.1 Electrode-level Oxygen Transport: Experimental Characterization.....	9
1.3.2 Local Resistance at the Ionomer Film.....	10
1.3.3 Catalyst Layer Morphology.....	11
1.3.4 Catalyst Layer Morphology and the Agglomerate Model.....	12
1.4 Scope of This Dissertation.....	13
1.4.1 Characterizing Oxygen Losses in the Diffusion Medium.....	14
1.4.2 Characterizing Oxygen Transport Resistance in the Catalyst Layer.....	14
1.4.3 Catalyst Layer Morphology and Oxygen Transport.....	15
1.4.4 Solid Oxide Fuel Cell Morphology.....	15
1.5 References for Chapter 1.....	16
2 In-Situ Measurement of Oxygen Transport Resistance Through the Thickness of a PEFC Diffusion Medium.....	23
2.1 Introduction.....	23
2.2 Experimental Methods.....	23
2.2.1 Physical Setup for Microsensor Insertion.....	23
2.2.2 Electrochemical Characterization of PEFC.....	26
2.2.3 Oxygen Concentration Measurement using Oxygen Flux Interrupt.....	27
2.2.4 Micro-CT of Diffusion Medium.....	30
2.3 Results and Discussion.....	31
2.3.1 Micro-CT of Diffusion Medium.....	31
2.3.2 Electrochemical Characterization of PEFC.....	32
2.3.3 Oxygen Concentration Measurements.....	33
2.4 Summary.....	43
2.5 References for Chapter 2.....	44
3 In-situ Thin-Film Microsensor for Characterizing Oxygen Transport in the Diffusion Medium	45
3.1 Introduction.....	45
3.2 Sensor Concept.....	45
3.3 Zero-Dimensional Sensor Model.....	47
3.4 Experimental.....	49
3.5 Results and Discussion.....	49
3.5.1 Sensor Characterization.....	49
3.5.2 Oxygen Flux Interrupt Measurements during PEFC Operation.....	50

3.6	Summary	55
3.7	References for Chapter 3	55
4	In-Situ Oxygen Concentration Measurement Through the Thickness of a Cathode Catalyst Layer	57
4.1	Introduction	57
4.2	Experimental	58
4.2.1	MES Fabrication	58
4.2.2	Experimental Setup	59
4.3	Results and Discussion	60
4.3.1	Fuel Cell and UME Characterization	60
4.3.2	Concentration Measurement with Potentiostatic Chronoamperometry	61
4.3.3	Concentration Distribution Measurement with PAD	63
4.4	Summary	67
4.5	References for Chapter 4	67
5	Resolving the 3D Catalyst Layer Microstructure Using Nanoscale X-ray Computed Tomography	69
5.1	Introduction	69
5.2	Experimental	70
5.2.1	Sample preparation	71
5.2.2	Porosimetry and electron microscopy	72
5.3	Nano-CT Data Collection	72
5.3.1	Image processing	72
5.4	Results and discussion	73
5.5	Summary	82
5.6	References for Chapter 5	83
6	Effects of an Experimental Agglomerate Size Distribution on the PEFC Agglomerate Model	85
6.1	Introduction	85
6.2	Theory	88
6.3	Results and Discussion	92
6.4	Implementing the Local Pt Nafion Oxygen Resistance	97
6.4.1	Derivation in the General Agglomerate Model Framework	97
6.4.2	Impact of Local Resistance	99
6.5	Summary	101
6.6	References	102
7	Oxygen Transport Resistance in Thin Nafion Binder Films in the Catalyst Layer	104
7.1	Introduction	104
7.2	Methods	106
7.3	Results and Discussion	107
7.4	Summary	114
7.5	References for Chapter 7	114
8	Modelling Through-Plane Oxygen Transport's Effect on PEFC Performance	116
8.1	Introduction	116
8.2	Model Framework	116
8.3	Results and Discussion	121
8.4	Summary	124
8.5	References for Chapter 8	125

9 Resolving Heterogeneous 3D Microstructures in Commercial Solid Oxide Fuel Cells using Nanoscale X-ray Computed Tomography	126
9.1 Introduction	126
9.2 Experimental	127
9.2.1 Synchrotron Micro-CT	128
9.2.2 Nano-CT	128
9.3 Results and Discussion.....	129
9.3.1 3D Image Reconstruction and Segmentation	129
9.3.2 Characterization of Heterogeneity	137
9.4 Summary	142
9.5 References for Chapter 9.....	142
10 Conclusions, Contributions, and Future Directions	145
A. Derivation of Volumetric Current Density in Agglomerate Model.....	150

List of Tables

Table 2.1: Summary of K_{form} and R_{O_2} Values	41
Table 8.1: Table of parameters used in model.....	120
Table 9.1: TPB Densities and Phase Fractions from Segmented Nano-CT Data.....	136

List of Figures

- Figure 1.1: Schematic of a PEFC in operation, with detail on cathode catalyst layer (CL) and further detail on a “three-phase” reaction site..... 3
- Figure 1.2: SEM images of (a) a composite DM with a carbon paper (labeled by source authors as “GDL”) and MPL,²¹ (b) carbon paper viewed from above,²² (c) TEM close-up of Pt/C catalyst used in CL,²³ and (d) SEM of ionomer-bound CL material.²⁴ All images taken from cited sources..... 4
- Figure 1.3: Different types of oxygen transport resistances present in a PEFC cathode, illustrated schematically as a network of resistors leading from the channel (O₂ “source”) to multiple sites of reaction. Detail of agglomerate-level resistances on right shows the local or “interfacial” resistance, which is not a function of geometry, and intra-agglomerate diffusion resistances. Electrode not to scale..... 6
- Figure 2.1 a) Schematic of oxygen microsensor penetrating into PEFC cathode. b) Photograph of physical setup for sensor and PEFC experiments. c) Photograph of the OX-25 oxygen microsensor. d) Dimensioned drawing of modifications made to the cathode flow plate. e) Detail schematic of sensor, through-hole, flow channel, and DM (to scale)..... 25
- Figure 2.2. a) Sensor signals with the PEFC at open circuit, at different values of RH (at 60°C) and temperature (at 72% RH). b) A typical waveform of the sensor signal during O₂ flux interrupt. The difference between V_{meas} and V_{N2} represents the measured O₂ concentration, and the difference between $V_{interrupt}$ and V_{N2} is the instantaneous calibration point, representing the O₂ concentration of the channel gas. 28
- Figure 2.3 Results of micro-CT scan of 10BC DM sample, including a) a virtual tomography slice of the 3D reconstruction; b) a virtual slice of the segmented 3D reconstruction, showing the fiber phase (white), the MPL or PTFE-binder phase (grey), and the pore phase (black); c) the distribution of phase fractions as a function of the z coordinate through the DM. 31
- Figure 2.4 Polarization curves for all cell builds at all RH values studied, at a cathode flow rate of 2 SLPM, with the through-hole sealed (dashed line) and open (solid line). Inset is the PEFC current density (normalized by the max value in each case) at 0.3 V, at different cathode gas flow rates, with both sealed (dashed line) and open hole (solid line) cases lying nearly on top of each other..... 33
- Figure 2.5 Anecdotal time series of oxygen microsensor signal during oxygen flux interrupt procedure, in (a) a case with no liquid water (83% RH, near the outer surface of the DM) and (b) a case with significant liquid water flooding at all currents (91% RH, just within the DM)..... 34
- Figure 2.6 Plots of dimensionless c_{O_2} at four different values of RH, and at four different PEFC currents, indicated on each figure. A virtual tomography slice from micro-CT of the DM is included, to scale, to illustrate microstructural features affecting the concentration profiles. 36

- Figure 2.7 Formation factor K_{form} for 62% and 72% RH cases at PEFC current densities of 1.5 and 1.8 A/cm². A virtual tomography slice from micro-CT of the DM is included, to scale, to illustrate microstructural features affecting the values of K_{form} 38
- Figure 2.8 Location of water onset at different values of RH, plotted versus PEFC current density. Location values of 0 indicate no flooding at all. A virtual tomography slice from micro-CT of the DM is included, to scale, to illustrate the location of flooding with respect to microstructural features. 42
- Figure 3.1 Thin-film sensor used for O₂ flux interrupt, with detail on the sensing tip. 47
- Figure 3.2: Results of a parametric study of ionomer bridge length using the 0-D sensor model. 48
- Figure 3.3: Sensor I/V curves for 21% and 10% oxygen, both with the PEFC at open circuit, 87% RH, and 60°C. 50
- Figure 3.4: (a) Dimensionless oxygen concentration measurements in 21% and 10% oxygen. Error bars represent +/- one standard deviation based on 11 measurements. The data points in the 21% O₂ case marked with a dotted line are questionable due to the PEFC Ohmic drop, but are included for completeness. (b) PEFC polarization curves from the same experiment as the concentration measurements in (a). In both plots, connecting lines are to guide the eye. PEFC was at 60°C and 87% RH. 52
- Figure 3.5 Oxygen transport resistance of the entire DM calculated from values of c_{O_2} measured in this study, plotted as a function of PEFC current density for full and half air cases. 55
- Figure 4.1 Schematic of O₂-sensing MES, with detail on Nafion coating of inner side-wall. Inset: SEM image of MES before filling with CL ink. 58
- Figure 4.2: (a) CV of the fuel cell at a scan rate of 10 mV/s, with cathode and anode inlet gas respectively at 30°C and 40°C, both flowing at 0.4 slpm at atmospheric pressure, and a cell temperature of 43°C. (b) Reverse scan from CV of a Pt UME located 42.3 μm from the membrane (scan rate 5 mV/s). A transport-limited ORR region can be seen in the vicinity of 0.2 V. 60
- Figure 4.3: Time series of current for the UME located 7.5 μm from the membrane as c_{O_2} - listed on figure as a fraction of $c_{O_2}(\text{air})$ - was varied every 60 s. 62
- Figure 4.4: UME current time series for a fuel cell voltage change from OCV to 0.2 V for the UME located 7.5 μm from the membrane. The change in current indicates the near complete depletion of oxygen. The inset shows the corresponding fuel cell current time series. 63
- Figure 4.5: *In-situ* distribution of c_{O_2} through the thickness of a fuel cell cathode operating at 450 mA/cm². A schematic key to the x-axis is shown below. A fit based on Fick's law with constant reaction rate is shown by a dotted line. The error bars represent the propagation of one standard deviation from the two calibration and one operating point measurements, with each of the three standard deviations being for 23 realizations. The dashed line indicates the c_{O_2} in the channel, defined as 1. 65
- Figure 5.1 Schematic of the nano-CT instrument, which uses x-ray optics to non-destructively achieve high-resolution 3D images of both hard and soft materials. A reflective condenser optic focuses the X-rays from a laboratory X-ray source onto the sample, which

rotates on a high-precision stage. The Fresnel zone plate objective is positioned past the sample. The Zernike phase ring then shifts the phase of the unscattered X-rays to enhance contrast, particularly for low-Z materials. 71

Figure 5.2 Verifying X-ray data with TEM images. a and b, A 2D X-ray slice of E1 before (a) and after (b) binary thresholding. The dark regions represent the solid phase in both images. c, Raw high resolution TEM image of a separate region of E1 with 1.72 nm pixels. d, Image c after binary thresholding to distinguish carbon particles. e, Image c after filtering and resizing for 50 nm resolution with 32.5 nm pixels. f, Image e after binary thresholding. Comparison between images d and f shows the macropore structure is resolved with 50 nm resolution. Images e and f are also qualitatively similar to the X-ray CT slices in images a and b. The dashed box in image b depicts the relative scale of the TEM images. 74

Figure 5.3 3D reconstructions of PEFC electrodes. a, The 3D solid phase of E1, which includes the ionomer and primary pores. b, The 3D secondary pore phase of E1. c and d, Magnified views of E1's solid (c) and pore (d) phase reconstructions. e and f, 3D reconstructions of E2's solid (e) and pore (f) phases. The cube dimensions in Images a, b, e and f are 3.25 x 3.25 x 3.25 μm . The porosity of the reconstructed E1 and E2 cubes are 43% and 41%, respectively. 77

Figure 5.4 Verification of nano-CT for PEFC electrodes with MIP measurement and simulations. MIP measurement for E1 and the corresponding pore size distributions from MIP simulations using the cubic 3D volume of Figure 5.3 (Cube) and a thicker, non-cubic volume (Thick). The relative cumulative volume is the cumulative intrusion volume divided by the total sample volume (sum of pore and solid volumes). The cube simulation's vertical error bars are the 95% confidence intervals for the six MIP simulations beginning on each face. The horizontal error bars are plus and minus half the side length of a voxel. Inset: Intrusion isosurfaces for MIP simulations for intruding spheres with diameters of 179, 146, and 114 nm in the cubic simulation, and the same for the thick simulation with 146 nm diameter spheres. 79

Figure 5.5 Pore and solid phase size distributions for PEFC electrodes. a, Solid phase size distributions for E1 and E2. The solid phase volume includes the Nafion and primary pore volumes. The peaks of the solid phase distributions are ca. 150 nm and 240 nm for E1 and E2, respectively. b, Pore size distributions for E1 and E2. The size distributions are based on inscribed spheres and are percentages of the total volume. c and d, Spatial size distributions for the pore (c) and solid (d) phases in a 2D slice (3.25 μm x 3.25 μm) of E1 on the $z = 1.625 \mu\text{m}$ plane, which is the same plane as Figure 5.2a. 81

Figure 6.1 Nano-CT characterization of a PEFC electrode's microstructure. a, Nano-CT reconstruction (50 nm resolution) of the solid phase of a PEFC electrode, from Chapter 5. b, Histogram showing the agglomerate diameter distribution, found by fitting inscribed spheres into the reconstruction shown in image a. The displayed average diameter of 188 nm was computed using volumetric weighting of each agglomerate bin. 87

Figure 6.2 Schematic of the model domain. The model presented here considers a small area slice of the catalyst layer at constant depth, in which the gas phase oxygen concentration in the secondary pores and electric potentials are constant. The bottom image depicts nomenclature concerning the spherical agglomerates. Note that the agglomerate diameter includes the ionomer film for comparison to physically measured values, whereas r_{agg} does not, to conform with the method of Thiele.¹⁷ 88

Figure 6.3 The agglomerate diameter and contribution to reaction rate. a, The effect of agglomerate diameter on effectiveness factor at cathode overpotentials of 0.7 V (red squares), 0.6 V (green circles), and 0.5 V (blue triangles). b, The volumetric fractional contribution to the overall cathode reaction for each agglomerate diameter, based on the volumetric distribution of effectiveness factors..... 93

Figure 6.4: Relationship between agglomerate diameter choice and model predictions as a function of overpotential. a, The effective agglomerate diameter, d_{eff} , versus overpotential. The volume-average diameter d_{avg} is shown for comparison. b, For each choice of agglomerate diameter (shown on figure for each curve), the error in j_{tot} when assuming a single agglomerate diameter. The baseline for computing the error is the value found by Equation (6.7), which accounts for the experimental agglomerate diameter distribution..... 95

Figure 6.5 Output polarization curves of a full non-PGM PEFC performance model based on the agglomerate framework, calculated using a single, uniform agglomerate diameter (blue) and a real distribution of agglomerate sizes (red). The range of agglomerate diameters was 0.6 to 8 μm with a mean of 2.4 μm , which is a typical agglomerate size distribution for these particular novel non-PGM catalyst layers..... 97

Figure 6.6 Effect of a small local Pt|Nafion level transport resistance on the results of Figure 6.4..... 100

Figure 7.1 The local oxygen transport resistance within PEFC cathodes is simulated by supporting thin Nafion films on a track-etched PCM with widely spaced cylindrical 10 nm pores. The PCM-supported Nafion's oxygen transport resistance is quantified using the limiting current of a modified 1 cm^2 PEFC..... 105

Figure 7.2 SEM images of the 1 wt% Nafion coated (left) and un-coated (right) surfaces of the PCM. The uncoated image shows the sparse distribution of 10 nm through-hole pores. 108

Figure 7.3 a) Log-log plot oxygen transport resistance of the Nafion coated PCM and Nafion membranes⁵⁻⁸ (NR211 from present study) as function of thickness. The corrected curve (solid) are the values when resistance is corrected for uniform 1D flux through a film of the same thickness using the correction factors in Figure 7.4e. The grey dashed line indicates a slope of 1 for expected proportionality between resistance and thickness. b) Linear plot of the same uncorrected and corrected oxygen transport resistance values, including the uncoated PCM and an inset near the zero-thickness intercept. The range of interfacial resistance estimation from prior work is shown at thicknesses they were estimated from in experiments; Suzuki et al.¹ (hatch fill), Ono et al.¹⁰ (black fill), Greszler et al.¹¹ (white fill)..... 110

Figure 7.4 a) X-ray radiography characterization of the 20 wt% Nafion film thickness. Red dashed lines show Nafion interfaces from the Zernike phase contrast image. b) Simulation of O_2 diffusion in the 2 μm film from the 20 wt% Nafion coating. c) TEM measurement of the 3 wt% Nafion film thickness. d) Simulation of O_2 diffusion in the 0.2 μm film from the 20 wt% Nafion coating. e) Correction factors for converting measured resistance to the corresponding value for uniform 1D flux based on a parametric computational study of O_2 diffusion through films of varying thickness..... 112

Figure 8.1 Schematic depiction of the treatment of single-phase oxygen transport resistance in this model..... 119

Figure 8.2 Experimental and model-generated IR-free polarization curves, with model curves for various values of the local O_2 transport resistance k_{local} (noted by each curve), ranging from the lower to upper limits of $R_{O_2,local}$ in the literature, and including the “best match” value of $k_{local} = 1.25 \times 10^{-3}$ m/s. Also depicted are the model results with no k_{local} effect, and with no mass transport effects. 122

Figure 8.3 Voltage losses arising from different mechanisms of oxygen transport resistance, namely (from the bottom): DM pores, CL pores, the Nafion film covering agglomerates, Nafion diffusion within the agglomerate interior, and the local ionomer/Pt resistance. Curves are cumulative with respect to the mechanisms of transport resistance. 123

Figure 9.1 Synchrotron micro-CT of cell. a) Virtual 2D slice of 3D synchrotron reconstruction, with cathode current collector (CCC), CAL, electrolyte (EL), anode active layer (AAL), and anode support layer (ASL) labelled. b) 2D intensity plot depicting the integrated greyscale intensity through a $150 \times 150 \mu\text{m}$ sub-volume containing only the CAL, after correcting for linear gradient and normalizing based on Eq. (9.2). 130

Figure 9.2 Nano-CT images. a) Radiograph of sample pillar, with CAL, electrolyte (EL), and AAL labelled, as well as a considerably large particle (LP) of LSM. From the 3D nano-CT reconstruction of the LSM-YSZ CAL, greyscale (b) and segmented (c) virtual 2D slices, with electrolyte situated at bottom (in segmented version, LSM is white, YSZ is grey, and pore is black). From the same reconstruction, the AAL’s greyscale (d) and segmented (e) virtual 2D slices, with electrolyte situated towards the top (in segmented version, nickel is grey and YSZ is white). 134

Figure 9.3 Determination of triple phase boundaries. a) Example of TPB vertices (black dots), orthogonal path connections (blue lines), and a final smoothed TPB curve (red curve) in 3D space. The orthogonal distance between each vertex is 32.5 nm (half a voxel). b) 3D renderings of CAL and AAL (dimensions shown in μm), each with a $(6.5 \mu\text{m})^3$ cube removed and the equivalent cloud of TPB curves shown for the cut-out volume. In 3D rendering of the CAL, red is LSM, light blue is YSZ, and pores are transparent. In AAL, dark blue is YSZ, green is Ni, and pores are transparent. The TPB densities for the specific cut-out sub-volumes shown here were $3.4 \mu\text{m}^{-2}$ and $5.6 \mu\text{m}^{-2}$ for the CAL and AAL, respectively. 137

Figure 9.4 2D variability of greyscale intensity (x-ray attenuation) in synchrotron image of CAL and AAL, expressed as 90% confidence intervals based on two-tailed Student-T distribution. 139

Figure 9.5 a) 3D variability of phase fraction based on size of placed sub-images. Curves shown are average variability for all three phases’ volume fractions in that layer (shown separately in inset). b) 3D variability of TPB density based on size of placed sub-images. Both (a) and (b) are expressed as 90% confidence intervals based on a two-tailed Student-T distribution. 141

1 Introduction

The emission of greenhouse gases (GHGs) is a problem of increasing urgency in today's world. Carbon dioxide is the anthropogenic GHG with the greatest impact on climate disruption, a phenomenon with the possibility for grave consequences.¹ As the United States depends almost entirely on oil for transportation, that sector accounted for 27% of U.S. GHG emissions in 2010.² More specifically, light-duty vehicles accounted for 17% of U.S. GHG emissions in that year.² These emissions are set only to get worse, as the miles driven in the U.S. are increasing at twice the rate as the population and are also rapidly increasing in developing countries.³

The United States' dependence on petroleum for transportation creates problems besides carbon dioxide emissions. Vehicle emissions contribute significantly to local and regional air pollution. Estimated healthcare spending due to urban air pollution is \$26-61 billion per year.⁴ U.S. petroleum dependence also subjects the country's energy situation to disruptions in foreign supply. In fact, the United States consumes 25% of the world's petroleum, but only produces 9% of it.³ U.S. military spending for protecting foreign oil interests was estimated to be \$15-47 billion per year in 2004.⁵ Although a 2012 report from the International Energy Agency suggests a shift in the next 20 years towards U.S. energy independence, it also predicts increasing fossil fuel usage exacerbating our environmental and public health woes.⁶

One line of technology with great promise to cure transportation energy woes is that of electric vehicles (EVs). Polymer electrolyte fuel cell (PEFC) EVs, accompanied by a hydrogen infrastructure backed by sustainably and domestically manufactured hydrogen, could enable a future US transportation sector that is free of harmful emissions, free of the costs incurred by defending foreign oil interests, and independent of the volatile global oil market. Such a fleet would surpass the EPA 2016 goal of 250 grams of CO₂ per vehicle per mile,⁷ considering that such automobiles have zero tailpipe emissions and reduced total emissions because of the more efficient electrochemical energy conversion.

However, major technological hurdles remain to widespread commercialization of PEFCs. Though the cost of automotive PEFC systems is ever-decreasing through research and development, their projected high-throughput cost in 2015 was still \$55/kW, compared to the

Department of Energy's 2020 target of \$40/kW and ultimate target of \$30/kW.⁸ Nearly half of the system's cost is the platinum catalyst materials and their application. However, Pt catalyst is significantly under-utilized in typical PEFC operation, with utilization as low as 10%, and oxygen transport losses are responsible for most of the loss in utilization.⁹⁻¹¹ The PEFC community has yet to directly measure oxygen gradients and thereby determine where in the electrode the bulk of these losses occur, and under what conditions this can change. In this dissertation, we will present research regarding through-plane transport phenomena in the porous electrodes of PEFCs.

1.1 Background: Polymer Electrolyte Fuel Cells

A schematic of a PEFC is shown in Figure 1.1. Hydrogen gas is fed to the anode, and an excess of oxygen (usually in air) to the cathode, through conductive gas-flow plates.¹² The reactant gases diffuse through a porous diffusion medium (DM) to the catalyst layer (CL). In the anode CL, hydrogen gas is oxidized, and the resulting protons travel through the polymer electrolyte membrane (PEM) to reach the cathode CL. The PEM is made of *ionomer*, a polymer that conducts protons and blocks electrons. (It also blocks wholesale mixing of gases, though it permits a small amount of H₂ diffusion). The most common ionomer in PEFCs is Nafion. Electrons are forced instead to travel outward through the conductive diffusion medium and an external circuit in order to reach the cathode. There, the electrons, the arriving protons from the PEM, and the supplied oxygen react to form water. The product water leaves via the hydrophobic DM, and is swept along with effluent gas.¹²

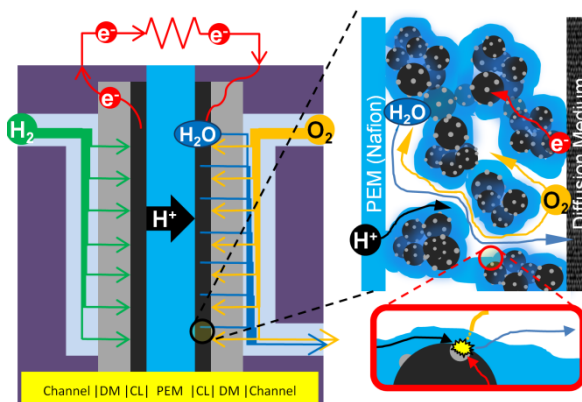


Figure 1.1: Schematic of a PEFC in operation, with detail on cathode catalyst layer (CL) and further detail on a “three-phase” reaction site.

The diffusion medium, sometimes called a gas diffusion layer (GDL), is typically a carbon fiber paper, felt, or cloth coated on one side with a micro-porous layer (MPL), all impregnated with a hydrophobic coating such as polytetrafluoroethylene (PTFE, a.k.a. Teflon).¹³ The DM allows electronic conduction to the CL, and the transport of gaseous reactants in and product water out of the electrode. The MPL faces towards the CL, and it has a similar pore structure as the CL, since it is usually made of carbon black and PTFE (PTFE is similar to Nafion, the polymer that binds the CL; in fact, until the 1990s, CLs were bound with PTFE¹⁴). Imaging studies have found that the MPL material, aside from forming its own distinct layer, also intrudes some distance into the carbon fiber layer.¹⁵⁻¹⁷ The MPL’s hydrophobic surfaces and small pores help prevent liquid water from accumulating in the cathode, forcing it into the carbon fiber layer.¹⁸⁻²⁰ There, the pores are large enough (10-100 μm) for some water to condense, though even there it is undesirable. From the carbon fiber layer, the water leaves through the gas flow channels.

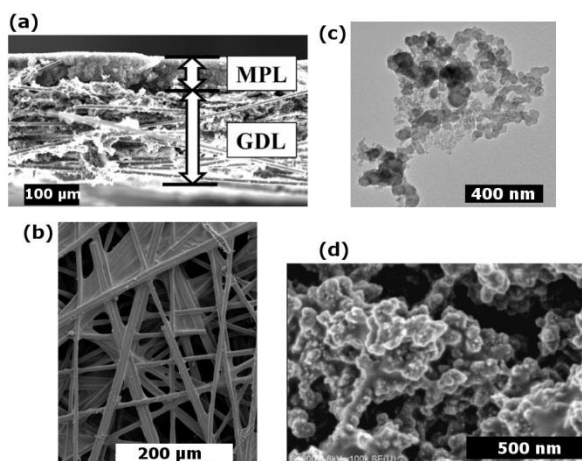


Figure 1.2: SEM images of (a) a composite DM with a carbon paper (labeled by source authors as “GDL”) and MPL,²¹ (b) carbon paper viewed from above,²² (c) TEM close-up of Pt/C catalyst used in CL,²³ and (d) SEM of ionomer-bound CL material.²⁴ All images taken from cited sources.

The cathode catalyst layer is a major focus of PEFC research due to the sluggish kinetics of the oxygen reduction reaction (ORR), as well as transport issues that arise in part from water production. As Figure 1 illustrates, the CL is a porous, multi-component medium with a complicated structure that is often described in terms of its three phases: electronic, ionic (proton), and gas.¹³ Different materials in the CL allow the transport of those three phases throughout the layer.

The catalyst layer is comprised of carbon black powder (~40 nm primary particle size) dotted with platinum nanoparticles (~3 nm), bound together into agglomerates by an ionomer.¹³ These agglomerates exist in a variety of shapes and sizes in a given CL, but according to our X-ray CT measurements, their mean size is on the order of 200 nm.²⁵ The network formed by the ionomer binder constitutes the ionic phase of the CL, while the percolating network formed by the carbon is the electronic phase. Macropores between the agglomerates are also on the order of 100s of nm.²⁵

Apart from recent, promising efforts toward novel non-noble-metal catalysts,²⁶⁻²⁸ platinum is the standard catalyst for PEFCs – despite its high cost – because of its very high catalytic activity for the oxygen reduction reaction and comparatively higher durability.²⁶ However, due primarily to mass transport issues, the effectiveness of catalyst utilization has been estimated to be only about 10% in PEFC operation.⁹⁻¹¹ Mass transport in the cathode includes both the transport of the reactant oxygen and the removal of product water. These two competing transport processes are inextricably linked – if water is not removed effectively, it can flood the diffusion medium and/or the CL, which increases resistance to oxygen transport.

1.1.1 Oxygen Transport in PEFC Cathodes

In PEFC cathodes, oxygen arrives first in flow channels that run across and along the length and width (the x-y plane) of the electrode. Because water droplets can form in these channels, and because more and more oxygen is consumed by reaction as it travels down the channel, there can be maldistributions in oxygen (and hence current generation) in the x-y plane; this is not the focus of this research, but is generally an important effect. This work focuses on oxygen transport in the z-direction through the thickness of the electrode, i.e. from the channel down through the DM and CL to the PEM. Since x-y variations in oxygen transport are not considered, one can think of the channel as a constant boundary condition for oxygen concentration in this through-thickness analysis (we achieve this in experiment with a high air flow rate, also known as a “differential cell” configuration). The different barriers to oxygen transport in this direction are illustrated in Figure 1.3, schematically represented by a network of resistors leading from the channel to multiple sites of reaction. Each “resistor” in this network will be experimentally addressed throughout this dissertation.

Diffusing from the channel, oxygen travels first through the coarse portion (carbon fiber paper, carbon fiber felt, or carbon cloth) of the DM, and then the finer-structured MPL, all at the same time as product water is leaving the CL (through the DM) to the channel. Entering the electrochemically active portion of the electrode, oxygen travels through the CL’s macropore system (the gas phase) to the surface of agglomerates throughout the CL, where it diffuses into the ionomer and towards the platinum catalyst’s surface.²⁹ Product water also travels out through the macropore network, and then out through the DM. Component interface resistances, e.g. at

the channel|DM interface or the MPL|CL interface, are not shown in Figure 1.3, but are instead lumped into the adjacent resistances; such interfacial resistances can however be significant.³⁰ What preceded was an overview of transport processes; the next few paragraphs provide further details on through-plane oxygen and water transport in each component of the cathode.

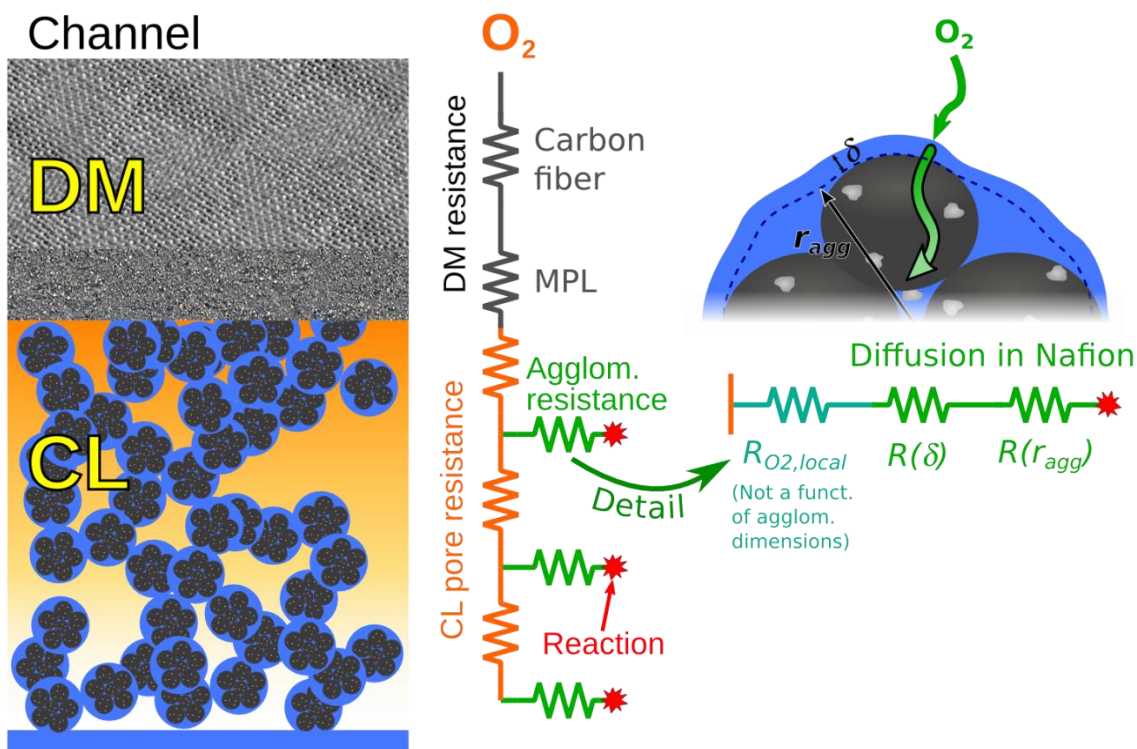


Figure 1.3: Different types of oxygen transport resistances present in a PEFC cathode, illustrated schematically as a network of resistors leading from the channel (O_2 “source”) to multiple sites of reaction. Detail of agglomerate-level resistances on right shows the local or “interfacial” resistance, which is not a function of geometry, and intra-agglomerate diffusion resistances. Electrode not to scale.

A number of modeling³¹⁻³⁴ and experimental^{20, 35-38} works have studied the interplay between water and oxygen transport in the DM. Imaging studies using synchrotron x-ray imaging^{35, 36} and neutron radiography³⁸ have demonstrated that there is significant liquid water throughout the DM in a variety of conditions. Several experiments^{20, 36, 37} and a pore-network DM model³⁴ suggest that, when the DM features an MPL, water forms breakthrough pathways or “capillary fingers.” As more water is generated, it tends to travel through these finger-like pathways – rather than forming a new path, which would incur a surface energy cost. However,

another work by Owejan et al.¹⁹ claimed that (though capillary “fingers” are likely at lower temperatures) most water removal in realistic PEFC operating conditions occurs in the vapor phase, and that the MPL’s role is primarily to prevent liquid water condensation at the CL/DM interface. Without an MPL, this interfacial condensation would block oxygen transport into CL pores, and likely imbibe into the CL pores, causing even further transport issues. Other works have found that natural cracks, holes, and asperities in the MPL on the orders of 1-100 μm allow water to condense in the MPL and at the MPL/CL interface,^{15, 30, 39} potentially causing significant barrier to oxygen transport.

Oxygen and water transport in the catalyst layer are more difficult to study experimentally, due to the layer’s smaller size and finer pores. CL-level oxygen and water are important to study, due to their interconnected nature. Under complete CL flooding (a largely hypothetical scenario), oxygen could only penetrate 0.1 to 1 μm into the 10-20 μm thick catalyst layer.⁴⁰ Furthermore, Eikerling⁴⁰ developed a model that suggests the formation of a “water band” in the cathode CL near the porous DM. There is no experimental verification of this result, but if true, this band would seriously impede oxygen transport to the farther reaches of the catalyst layer. In other PEFC electrode models, different treatments of through-thickness and agglomerate level transport yield significantly different predictions of both through-plane distribution of oxygen and fuel cell performance, even without consideration of liquid water.⁴¹

At the level of ionomer-bound Pt/C agglomerates, it is generally understood that oxygen undergoes Henry-like dissolution into the surrounding ionomer binder and diffusion through that binder,^{29, 42} followed by diffusion/reaction through the inner region,^{29, 40} which contains Pt/C particles and may be filled with a combination of ionomer, mesoporous voids, and liquid water.^{43, 44} Recently (since 2010), increasing research has been pointing to an additional oxygen transport resistance that is local to the catalyst/binder⁴⁵⁻⁵¹ – one that is crucial to understand since it becomes more significant at low platinum loading.⁴⁸⁻⁵¹ This new resistance is often ascribed to interfacial effects in the ionomer, though it is also possible that this resistance occurs instead within the ionomer or as an adsorption step on the platinum surface.^{49, 50}

1.2 Background: Solid Oxide Fuel Cells

Solid oxide fuel cells (SOFCs) are a promising energy conversion technology for both centralized and distributed electricity and heat generation, owing to their scalability, high fuel efficiency, and fuel flexibility.⁵² Because they can be fueled by widely available methane, SOFCs have already seen some implementation for distributed electricity and heat co-generation in residential and commercial settings. They are also a promising technology for centralized power generation: previous researchers have found that SOFCs, combined with coal gasification and carbon capture, provide one of the most efficient methods of generating carbon-emission-free electricity from coal.^{53,54}

Anode-supported SOFCs,⁵⁵ such as those studied in this work, are typically comprised of 5 distinct layers: 1) a thick porous, electron-conducting anode support layer that acts as a carrier for the rest of the cell; 2) a porous, composite anode active layer (AAL); 3) a dense YSZ electrolyte layer; 4) a porous, composite cathode active layer (CAL); and 5) a porous, electron-conducting cathode current collector layer. Oxygen is reduced at the CAL, and hydrogen (which may be internally reformed from methane and other fuels) is oxidized at the AAL. The CAL is typically composed of an ion-conducting phase (ICP) like YSZ, and an electron-conducting phase (ECP) such as lanthanum strontium manganite (LSM) or lanthanum strontium cobalt ferrite (LSCF). Similarly, the AAL uses an ICP such as YSZ, and an ECP, typically nickel.

In the active layers, the reaction can only happen where the gas-carrying pores, the ECP, and the ICP all come together – these locations are known as triple-phase boundaries (TPBs). A high density of TPBs is important for a high reaction rate, as are the transport of ions, electrons, and gas to the TPB locations in the microstructure. Degradation in SOFC cathodes is also tied to overpotential,⁵⁶ which will depend in part on microstructure for a given reaction rate. For these reasons, microstructural characterization has been a recent thrust in SOFC research, as will be detailed later in this dissertation.

1.3 Relevant Work

1.3.1 Electrode-level Oxygen Transport: Experimental Characterization

There are a number of ways to characterize oxygen transport losses using global, cell-level measurements, largely focusing on the effect of different operating conditions and electrode compositions on PEFC performance. For example, cathode transport parameters can be estimated by analyzing the PEFC's transient current/voltage behavior in a closed system with finite oxygen.⁵⁷ With a more typical open-system, flow-through cathode, other methods are possible. In-depth analysis of a PEFC's I-V curve, coupled with testing the effects of different gas mixtures, can yield insight into which mechanisms of voltage loss are dominant,⁵⁸⁻⁶¹ including whether oxygen transport losses in the pore or ionomer binder phases play a major role.^{59, 60} In a related but more specific method, researchers also study the effect of different operating conditions on the PEFC's limiting current in order to extract cathode transport parameters and identify the dominant loss mechanisms.^{45, 48-50, 59, 60, 62-64} The "limiting current" (or limiting reaction rate) refers to the mass-transport-limited current – the highest current that an electrode can support at a given concentration of reactant in its environment (c_{O_2} in the channels, in this case), given that electrode's inherent mass transport resistances. Most recently, limiting current studies in PEFCs with carefully varied platinum loadings and feed gas conditions have yielded insight into the unexplained oxygen transport resistance local to the catalyst.⁴⁸⁻⁵⁰

A range of studies have been carried out on PEFC electrodes and hardware concerning *in-situ* measurements of in-plane distributions of various quantities.⁶⁵⁻⁷⁰ *In-situ* measurements within the PEFC's membrane-electrode assembly have been limited. Prior studies from other groups have used platinum-wire probes embedded in the PEM to measure the presence of hydrogen peroxide,^{71, 72} oxygen and hydrogen concentrations,^{69, 73, 74} and water content.⁷⁵ Some of these studies featured multiple probes embedded through the thickness of the membrane to obtain through-plane measurements.^{71, 73, 75} Perhaps the most relevant of these studies to this work are those that amperometrically sensed oxygen concentrations at the cathode CL/PEM interface,^{69, 72, 74} one of which did so with multiple probes across the plane of the PEM to obtain in-plane distributions.⁶⁹ In my own group, we have devised an MES that measures the ionic potential distribution through the thickness of a PEFC cathode⁷⁶ using fabrication techniques

similar to, and devised in parallel with, the oxygen-sensing MES presented in this dissertation. Outside of our group's electrode scaffold approach,^{76, 77} we know of only a handful of through-plane distribution measurements in electrochemical electrodes – an interrupted-electrode approach for Li-ion batteries that is too intrusive to use in fuel cells,⁷⁸ and through-plane imaging of Li concentration in Li-ion battery electrodes using neutron radiography⁷⁹ or optical imaging.⁸⁰

Outside of actual operating PEFCs, several studies have made *ex-situ* determinations of the oxygen diffusivity of DMs^{21, 81, 82} and of CL material,⁸³ providing valuable input to models (computational, analytical, and theoretical) of oxygen transport. However, the PEFC community is still mostly lacking on direct, *in-situ* measurements of c_{O_2} throughout the cathode – measurements that would validate such models and provide insight into the dominant mechanisms of oxygen transport losses. This is difficult due to the physically small scales involved in the CL, but such measurements are crucial to understanding thermal and liquid water gradients that complicate models that are otherwise well-validated. Later, this dissertation will show further detail into our work on making such measurements.

1.3.2 Local Resistance at the Ionomer Film

A recent (ca. 2010), concerning finding in PEFC development is that as the Pt loading is reduced, a previously unaccounted-for O_2 transport resistance becomes significant.^{47, 49, 84-89} This apparent increase in mass transport voltage loss at low loading reduces the power density, offsetting the cost savings from reduced catalyst material. Several groups, including many from the automotive fuel cell industry, have identified that the additional resistance scales with Pt surface area.^{47, 87, 88} By studying the O_2 transport resistance at different Pt loadings, the *in-situ* measurements of Greszler et al.⁸⁸ and Ono et al.⁸⁷ estimate the additional, local O_2 transport resistance in the range of 10-20 s/cm, equivalent to diffusion through tens of nanometers of ionomer film (when in reality, the ionomer binder films in the CL are only 1-10 nm thick.⁵⁰).

One hypothesis is that the thin Nafion film has a different structure from bulk Nafion in a way that reduces O_2 permeability. Another hypothesis is that there is an interfacial effect that only becomes observable as the films become very thin (e.g., a kinetic limitation to O_2 dissolution). Greszler *et al.*⁸⁸ suggested a third hypothesis of a first order sulfonic acid group

adsorption onto the Pt that interferes with the ORR.^{90, 91} The combined in-situ experiments and simplified single particle model in a separate work by Owejan et al.⁸⁶ suggests that combined interfacial resistances at the Pt|Nafion and the Nafion|air interfaces could be responsible for the additional local resistance. The only ex-situ studies of this effect have been by Suzuki et al.,⁴⁵⁻⁴⁷ who used Pt electrodes coated with thin Nafion films of different thicknesses to measure Nafion's oxygen diffusivity. Extrapolating the data showed a finite oxygen resistance at zero thickness – we would expect zero from bulk diffusion theory, but it was in fact quite large, with the lower end of their measured range agreeing with that of the other in-situ works. Since Suzuki et al.'s ionomer films⁴⁵⁻⁴⁷ were coated directly on Pt electrodes, and since the other studies involved CLs where the ionomer was in contact with Pt,⁴⁸⁻⁵⁰ the exact mechanism has not been clear.

1.3.3 Catalyst Layer Morphology

Researchers use a range of techniques to examine PEFC catalyst layer morphology, each with its own advantages and drawbacks. Mercury intrusion porosimetry (MIP) and gas adsorption techniques⁹² have given valuable insight into CL morphology^{23, 43, 93, 94} by measuring volumetric pore size and surface area distributions. However, MIP and gas adsorption are generally bulk techniques without spatial specificity, and they can be limited by the effect of pore throats.⁹² Transmission electron microscopy (TEM) offers high resolution and elemental contrast; it is a powerful tool for examining electrode microstructures,⁹⁴⁻¹⁰² but due to its limited sample size, it is less suited for macrostructural characterization. A few other minor shortcomings limit TEM's ability to fully characterize the CL's 3D porous structure. The 2D image is integrated through a ca. 100 nm ultra-microtome, reducing apparent porosity – though tilt TEM tomography offers some insight into the 3D structure.^{101, 102} It is also difficult to distinguish the CL's ionomer from the epoxy binding the microtome,^{94, 97, 98, 100-102} though cesium ion staining of the ionomer and/or energy-filtered imaging can allow TEM to distinguish the ionomer coating the agglomerates.^{98, 103}

Two-dimensional scanning electron microscopy (SEM) can resolve carbon black particles and the larger microstructure.^{24, 94, 96, 98, 104-106} With the additional use of destructive focused ion beam (FIB) sectioning, a series of SEM images can be computationally

reconstructed into a 3D image of the electrode,^{102, 104-106} although it is unclear to what extent the FIB damages the ionomer.²⁴ FIB-SEM (with its high field-of-view but limited detail) can be combined tilt-TEM tomography (lower field-of-view, higher detail) – this multi-scale approach has been used to generate a representative reconstruction of the platinum distribution in a CL.¹⁰² Elemental mapping techniques such as back-scattered electron,⁹⁸ energy dispersive X-ray,^{96, 98} and energy-filtered TEM imaging,⁹⁸ as well as soft X-ray spectromicroscopy,¹⁰⁷ can also aid in imaging material distributions in electrodes.

X-ray computed tomography (XCT) offers the capability to non-destructively resolve the 3D structure of porous materials with high spatial resolution^{15, 35, 82, 106, 108-111} using X-ray radiographs from many angles to computationally reconstruct a 3D image of the material.⁹² Empty pores absorb less radiation and hence contrast with solid materials. In the fuel cell field, this technique has been used at micron-scale resolution to image DM materials from PEFCs,^{15, 17, 35, 82, 112} yielding structural properties,^{15, 17, 82, 112} transport properties,^{17, 82, 112} and insight into the distribution of liquid water.³⁵ Higher resolution (resolution of 50 nm) X-ray CT (nano-CT) has been used by other groups in 2D form to study platinum redistribution during cell aging.¹⁰⁹ This dissertation will cover in further detail our work to characterize the 3D structure of PEFC catalyst layers using nano-CT.

1.3.4 Catalyst Layer Morphology and the Agglomerate Model

The agglomerate model,^{9, 29, 41, 84, 113-124} which makes use of generalized microstructural CL knowledge to simulate PEFC performance, is a popular approach to simulating the performance of PEFC electrodes. This modeling approach uses analytical solutions for coupled oxygen diffusion and reduction reaction in an idealized, spherical agglomerate. It thereby offers a more detailed physical and mathematical description of the transport processes in the electrode compared to the macro-homogeneous or interface approaches.⁴¹ However, most prior implementations of the agglomerate model have assumed a single, representative agglomerate diameter^{9, 29, 41, 113-124} (though references^{9, 116, 122} parametrically vary a uniform agglomerate diameter) and do not consider the non-uniform size distributions that actually exist within an electrode. One notable exception is Yoon and Weber,⁸⁴ who consider a deliberate gradient of agglomerate sizes from the membrane to the diffusion medium. In reality, a size distribution

arises in the CL from the primary particle aggregate size distribution and uncontrolled agglomeration, which can be determined using microstructural characterization techniques. This dissertation includes work to examine how that size distribution affects the ORR rates predicted by the agglomerate porous electrode model.

1.4 Scope of This Dissertation

Oxygen transport through the thickness of a PEFC cathode is still not completely characterized. Cell-level measurements can and show how severe oxygen transport losses are, but questions remain. How much of that oxygen loss occurs in the DM versus in the CL? Of the loss in the CL, does more of that loss occur in the pores, or at the agglomerate level? In short, my aim is to determine the relative contributions of the different “resistors” in Figure 1.3. In the work presented in this dissertation, we develop the tools to fully answer these questions by directly measuring oxygen concentrations at different points in the PEFC cathode. In line with the mass transport/electricity analogy, to measure c_{O_2} is equivalent to measuring the “voltage” at nodes between the resistors in Figure 1.3. To that end, this portion of the work focuses on several kinds of oxygen concentration sensors: commercial microprobes, custom-made, amperometric *in-situ* oxygen sensors, and an *ex-situ* oxygen transport resistance measuring experiment. We also investigate the microstructure of the CL using nanoscale X-ray computed tomography, and apply those results to a PEFC model, and develop similar techniques for a different kind of fuel cell (solid oxide fuel cell, or SOFC). To summarize, the projects outlined herein are:

- *In-situ* measurements at multiple points through the channel and DM using a commercial oxygen probe
- An *in-situ* thin-film oxygen sensor at the DM/CL interface
- A micro-structured electrode scaffold, with multiple *in-situ* oxygen sensors along the thickness of a working CL
- An *ex-situ* experiment to measure the oxygen transport resistance of thin ionomer films similar to the CL binder

- 3D microstructural characterization of the PEFC CL, and application of results to PEFC models
- Application of microstructural characterization techniques to SOFCs

1.4.1 Characterizing Oxygen Losses in the Diffusion Medium

An oxygen microsensor with a 25 μm tip is advanced through the thickness of the channel and the DM of an operating PEFC cathode. At each location, at different values of relative humidity (RH) and PEFC current density, we measure the oxygen concentration. We do so using a new self-referencing technique we call *oxygen flux interrupt* that re-calibrates the sensor upon each measurement, to obviate the issue of sensor drift over time and sensor mis-calibration due to changing humidity and temperature. Thereby we characterize the oxygen transport resistance, and by proxy the microstructure, as a function of coordinate through the DM. We use these results together with microscale x-ray computed tomography (micro-CT) to make inferences about the effect of microstructure on transport. We also map out water flooding as a function of space, RH, and current density.

In another work, an in-house fabricated thin-film sensor architecture is placed at the interface between the DM (more specifically, the MPL) and the CL, measuring the oxygen concentration at that location using oxygen flux interrupt. This DM/CL sensor is fabricated using benchtop thin-film techniques, and it can be used in conjunction with both commercial and custom PEFC electrodes and DMs.

1.4.2 Characterizing Oxygen Transport Resistance in the Catalyst Layer

The second sensor type is a thin-film scaffold to hold multiple electrodes along the thickness of the catalyst layer; each thin-film electrode in the scaffold serves as a separate oxygen sensor. This micro-structured electrode scaffold (MES) holds the sensing layers in place around a small hole, where we deposit CL material, essentially constructing the CL to be studied inside of the scaffold of sensors. In this way, we measure the concentration of oxygen in the pore phase of the CL at various points through its thickness.

Along with the *in-situ* sensor studies, we employ an *ex-situ* apparatus to measure the oxygen transport loss through thin (from the order of 10 nm up to the order of 10 μm) films of Nafion in a realistic PEFC environment. These Nafion films are supported by an inactive substrate with negligible oxygen transport resistance compared to the Nafion film. In this way, we measure the Nafion films' oxygen transport properties independent of the electrochemical Nafion|Pt interface, in order to determine whether the additional resistance seen in the literature arises from the Nafion|Pt interface, or by another mechanism.

1.4.3 Catalyst Layer Morphology and Oxygen Transport

The 3D microstructure of the CL – in particular, the geometry and connectivity of pores and agglomerates – plays a large role in governing oxygen transport within the layer. This work will feature the characterization of the CL's 3D morphology using nanoscale X-ray computed tomography (nano-CT). We will use this knowledge of CL morphology in conjunction with the PEFC agglomerate model (a popular approach to modeling PEFC electrode performance) to examine its effect on oxygen transport and reaction distribution.

1.4.4 Solid Oxide Fuel Cell Morphology

We also apply the techniques developed for nano-CT characterization of the CL to another kind of fuel cell entirely. SOFCs use a ceramic/metallic composite for their electrochemically active layers. The different materials present unique challenges in nano-CT characterization, and the microstructure of these layers exists on a different scale than that of PEFC CLs. The composite nature of the material gives rise to several microstructural performance metrics, such as triple phase boundaries, that we calculate in 3D space from the microstructural data.

1.5 References for Chapter 1

1. Fourth Assessment Report of the IPCC, in, Intergovernmental Panel on Climate Change (IPCC) (2007).
2. Transportation Energy Data Book. *Oak Ridge National Laboratory*, **31** (2012).
3. Transportation Energy Data Book: Edition 25, in, Oak Ridge National Laboratory (2006).
4. M. A. Delucchi, J. J. Murphy and D. R. McCubbin, *Journal of Environmental Management*, **64**, 139 (2002).
5. M. A. Delucchi and J. J. Murphy, *Energy Policy*, **36**, 2253 (2008).
6. World Energy Outlook 2012, in, International Energy Agency (2012).
7. DOT Secretary Ray LaHood and EPA Administrator Lisa P. Jackson Propose National Program to Improve Fuel Economy and Reduce Greenhouse Gases/ New Interagency Program to Address Climate Change and Energy Security in *US EPA News Releases*, US EPA (2009).
8. D. Papageorgopoulos, in Dept. of Energy 2015 Annual Merit Review and Peer Evaluation Meeting, Washington, D.C. (2015).
9. Z. T. Xia, Q. P. Wang, M. Eikerling and Z. S. Liu, *Can. J. Chem.*, **86**, 657 (2008).
10. M. Lee, M. Uchida, D. A. Tryk, H. Uchida and M. Watanabe, *Electrochim. Acta*, **56**, 4783 (2011).
11. M. Lee, M. Uchida, H. Yano, D. A. Tryk, H. Uchida and M. Watanabe, *Electrochim. Acta*, **55**, 8504 (2010).
12. F. Barbir, *PEM Fuel Cells: Theory and Practice*, Elsevier Academic Press, London (2005).
13. S. Litster and G. McLean, *J. Power Sources*, **130**, 61 (2004).
14. M. S. Wilson and S. Gottesfeld, *J. Appl. Electrochem.*, **22**, 1 (1992).
15. Z. Fishman and A. Bazylak, *J. Electrochem. Soc.*, **158**, B846 (2011).
16. Z. Fishman, J. Hinebaugh and A. Bazylak, *J. Electrochem. Soc.*, **157**, B1643 (2010).
17. E. a. Wargo, V. P. Schulz, A. Çeçen, S. R. Kalidindi and E. C. Kumbur, *Electrochim. Acta*, **87**, 201 (2013).
18. L. Cindrella, A. M. Kannan, J. F. Lin, K. Saminathan, Y. Ho, C. W. Lin and J. Wertz, *J. Power Sources*, **194**, 146 (2009).

19. J. P. Owejan, J. E. Owejan, W. Gu, T. A. Trabold, T. W. Tighe and M. F. Mathias, *J. Electrochem. Soc.*, **157**, B1456 (2010).
20. J. T. Gostick, M. A. Ioannidis, M. W. Fowler and M. D. Pritzker, *Electrochem. Commun.*, **11**, 576 (2009).
21. C. Chan, N. Zamel, X. Li and J. Shen, *Electrochim. Acta*, **65**, 13 (2012).
22. V. Berejnov, A. Bazylak, D. Sinton and N. Djilali, *J. Electrochem. Soc.*, **157**, B760 (2010).
23. T. Soboleva, X. S. Zhao, K. Mallek, Z. Xie, T. Navessin and S. Holdcroft, *ACS Appl. Mater. Interfaces*, **2**, 375 (2010).
24. C. S. Kuroda and Y. Yamazaki, *ECS Trans.*, **11**, 509 (2007).
25. W. K. Epting, J. Gelb and S. Litster, *Adv. Funct. Mater.*, **22**, 555 (2012).
26. M. Lefevre, E. Proietti, F. Jaouen and J. P. Dodelet, *Science*, **324**, 71 (2009).
27. H. A. Gasteiger and N. M. Markovic, *Science*, **324**, 48 (2009).
28. R. Bashyam and P. Zelenay, *Nature*, **443**, 63 (2006).
29. W. Sun, B. A. Peppley and K. Karan, *Electrochim. Acta*, **50**, 3359 (2005).
30. I. V. Zenyuk, R. Taspinar, a. R. Kalidindi, E. C. Kumbur and S. Litster, *J. Electrochem. Soc.*, **161**, F3091 (2014).
31. T. Berning and N. Djilali, *J. Electrochem. Soc.*, **150**, A1589 (2003).
32. A. Z. Weber, R. M. Darling and J. Newman, *J. Electrochem. Soc.*, **151**, A1715 (2004).
33. J. T. Gostick, M. A. Ioannidis, M. W. Fowler and M. D. Pritzker, *J. Power Sources*, **173**, 277 (2007).
34. P. K. Sinha and C. Y. Wang, *Electrochim. Acta*, **52**, 7936 (2007).
35. J. Eller, T. Rosen, F. Marone, M. Stampanoni, A. Wokaun and F. N. Buchi, *J. Electrochem. Soc.*, **158**, B963 (2011).
36. J. Lee, J. Hinebaugh and A. Bazylak, *J. Power Sources*, **227**, 123 (2013).
37. S. Litster, D. Sinton and N. Djilali, *J. Power Sources*, **154**, 95 (2006).
38. R. S. Fu, U. Pasaogullari, T. Shiomi, Y. Tabuchi, D. S. Hussey and D. L. Jacobson, *J. Electrochem. Soc.*, **159**, F545 (2012).
39. T. Swamy, E. C. Kumbur and M. M. Mench, *J. Electrochem. Soc.*, **157**, B77 (2010).
40. M. Eikerling, *J. Electrochem. Soc.*, **153**, E58 (2006).

41. D. Harvey, J. G. Pharoah and K. Karan, *Journal of Power Sources*, **179**, 209 (2008).
42. A. Parthasarathy, S. Srinivasan, A. J. Appleby and C. R. Martin, *J. Electrochem. Soc.*, **139**, 2856 (1992).
43. M. Uchida, Y. Aoyama, N. Eda and A. Ohta, *J. Electrochem. Soc.*, **142**, 4143 (1995).
44. K. Malek, M. Eikerling, Q. P. Wang, T. C. Navessin and Z. S. Liu, *J. Phys. Chem. C*, **111**, 13627 (2007).
45. K. Kudo, T. Suzuki and Y. Morimoto, *ECS Trans.*, **33**, 1495 (2010).
46. K. Kudo and Y. Morimoto, *ECS Meeting Abstracts*, **MA2012-02**, 1270 (2012).
47. T. Suzuki, K. Kudo and Y. Morimoto, *Journal of Power Sources*, **222**, 379 (2013).
48. Y. Ono, T. Mashio, S. Takaichi, A. Ohma, H. Kanesaka and K. Shinohara, *ECS Trans.*, **28**, 69 (2010).
49. N. Nonoyama, S. Okazaki, A. Z. Weber, Y. Ikogi and T. Yoshida, *J. Electrochem. Soc.*, **158**, B416 (2011).
50. T. A. Greszler, D. A. Caulk and P. K. Sinha, *J. Electrochem. Soc.*, **159**, F831 (2012).
51. J. P. Owejan, J. E. Owejan and W. Gu, *J. Electrochem. Soc.*, **160**, F824 (2013).
52. S. C. Singhal, *Solid State Ion.*, **135**, 305 (2000).
53. N. S. Siefert and S. Litster, *Applied Energy*, **107**, 315 (2013).
54. K. J. Gerdes, D. Gray, J. M. Klara, J. Plunkett, S. Salerno, G. Tomlinson and C. W. White, in (2010).
55. S. de Souza, Reduced-Temperature Solid Oxide Fuel Cell Based on YSZ Thin-Film Electrolyte, in *J. Electrochem. Soc.*, p. L35 (1997).
56. H. Yokokawa, H. Tu, B. Iwanschitz and A. Mai, *J. Power Sources*, **182**, 400 (2008).
57. J. r. Stumper, H. Haas and A. Granados, *J. Electrochem. Soc.*, **152**, A837 (2005).
58. J. Benziger, E. Kimball, R. Mejia-Ariza and I. Kevrekidis, *Aiche Journal*, **57**, 2505 (2011).
59. M. V. Williams, H. R. Kunz and J. M. Fenton, *J. Electrochem. Soc.*, **152**, A635 (2005).
60. S. Sambandam and V. Ramani, *Phys. Chem. Chem. Phys.*, **12**, 6140 (2010).
61. Y. W. Rho, O. A. Velev, S. Srinivasan and Y. T. Kho, *J. Electrochem. Soc.*, **141**, 2084 (1994).

62. J. St-Pierre, B. Wetton, G. S. Kim and K. Promislow, *J. Electrochem. Soc.*, **154**, B186 (2007).
63. U. Beuscher, *J. Electrochem. Soc.*, **153**, A1788 (2006).
64. D. R. Baker, D. A. Caulk, K. C. Neyerlin and M. W. Murphy, *J. Electrochem. Soc.*, **156**, B991 (2009).
65. D. J. L. Brett, S. Atkins, N. P. Brandon, V. Vesovic, N. Vasileiadis and A. Kucernak, *Electrochemical and Solid-State Letters*, **6**, A63 (2003).
66. D. J. L. Brett, S. Atkins, N. P. Brandon, V. Vesovic, N. Vasileiadis and A. R. Kucernak, *Electrochemistry Communications*, **3**, 628 (2001).
67. H. Ju and C. Y. Wang, *J. Electrochem. Soc.*, **151**, A1954 (2004).
68. X. G. Yang, N. Burke, C. Y. Wang, K. Tajiri and K. Shinohara, *J. Electrochem. Soc.*, **152**, A759 (2005).
69. S. Takaichi, H. Uchida and M. Watanabe, *Electrochim. Acta*, **53**, 4699 (2008).
70. R. Montanini, G. Squadrito and G. Giacoppo, *J. Power Sources*, **196**, 8484 (2011).
71. W. Liu and D. Zuckerbrod, *J. Electrochem. Soc.*, **152**, A1165 (2005).
72. S. Sambandam and V. Ramani, *ECS Trans.*, **25**, 433 (2009).
73. S. Takaichi, H. Uchida and M. Watanabe, *Electrochem. Commun.*, **9**, 1975 (2007).
74. T. Mashio, A. Ohma and K. Shinohara, *ECS Trans.*, **16**, 1009 (2008).
75. F. N. Büchi and G. G. Scherer, *J. Electrochem. Soc.*, **148**, A183 (2001).
76. K. C. Hess, W. K. Epting and S. Litster, *Anal. Chem.*, **83**, 9492 (2011).
77. K. C. Hess, J. F. Whitacre and S. Litster, *J. Electrochem. Soc.*, **159**, A1351 (2012).
78. S. H. Ng, F. La Mantia and P. Novak, *Angew. Chem.-Int. Edit.*, **48**, 528 (2009).
79. J. B. Siegel, X. Lin, A. G. Stefanopoulou, D. S. Hussey, D. L. Jacobson and D. Gorsich, *J. Electrochem. Soc.*, **158**, A523.
80. S. J. Harris, A. Timmons, D. R. Baker and C. Monroe, *Chem. Phys. Lett.*, **485**, 265 (2010).
81. R. Flückiger, S. A. Freunberger, D. Kramer, A. Wokaun, G. n. G. Scherer and F. N. Büchi, *Electrochim. Acta*, **54**, 551 (2008).
82. J. r. Becker, R. Flückiger, M. Reum, F. N. Büchi, F. Marone and M. Stampanoni, *J. Electrochem. Soc.*, **156**, B1175 (2009).

83. Z. Yu and R. N. Carter, *J. Power Sources*, **195**, 1079 (2010).
84. W. Yoon and A. Z. Weber, *Journal of The Electrochemical Society*, **158**, B1007 (2011).
85. A. Z. Weber and A. Kusoglu, *Journal of Materials Chemistry A*, **2**, 17207 (2014).
86. J. P. Owejan, J. E. Owejan and W. Gu, *Journal of the Electrochemical Society*, **160**, F824 (2013).
87. Y. Ono, A. Ohma, K. Shinohara and K. Fushinobu, *Journal of the Electrochemical Society*, **160**, F779 (2013).
88. T. A. Greszler, D. Caulk and P. Sinha, *Journal of The Electrochemical Society*, **159**, F831 (2012).
89. M.-J. Choo, K.-H. Oh, J.-K. Park and H.-T. Kim, *Chemelectrochem*, **2**, 382 (2015).
90. T. Masuda, H. Fukumitsu, T. Kondo, H. Naohara, K. Tamura, O. Sakata and K. Uosaki, *The Journal of Physical Chemistry C*, **117**, 12168 (2013).
91. R. Subbaraman, D. Strmcnik, V. Stamenkovic and N. M. Markovic, *J. Phys. Chem. C*, **114**, 8414 (2010).
92. P.-Z. Wong, *Methods in the Physics of Porous Media*, Academic Press, San Diego (1999).
93. M. Uchida, Y. Fukuoka, Y. Sugawara, N. Eda and A. Ohta, *J. Electrochem. Soc.*, **143**, 2245 (1996).
94. J. Xie, K. L. More, T. A. Zawodzinski and W. H. Smith, *J. Electrochem. Soc.*, **151**, A1841 (2004).
95. F. Xu, H. Y. Zhang, J. Ilavsky, L. Stanciu, D. Ho, M. J. Justice, H. I. Petrache and J. A. Xie, *Langmuir*, **26**, 19199 (2011).
96. J. Xie, F. Garzon, T. Zawodzinski and W. Smith, *J. Electrochem. Soc.*, **151**, A1084 (2004).
97. J. Xie, D. L. Wood, K. L. More, P. Atanassov and R. L. Borup, *J. Electrochem. Soc.*, **152**, A1011 (2005).
98. F. Scheiba, N. Benker, U. Kunz, C. Roth and H. Fuess, *J. Power Sources*, **177**, 273 (2008).
99. Y. Shao-Horn, W. C. Sheng, S. Chen, P. J. Ferreira, E. F. Holby and D. Morgan, *Top. Catal.*, **46**, 285 (2007).

100. C.-N. Sun, K. L. More and T. A. Zawodzinski, *ECS Trans.*, **33**, 1207 (2010).
101. H. Uchida, J. M. Song, S. Suzuki, E. Nakazawa, N. Baba and M. Watanabe, *J. Phys. Chem. B*, **110**, 13319 (2006).
102. S. Thiele, T. Färstehaupt, D. Banham, T. Hutzenlaub, V. Birss, C. Ziegler and R. Zengerle, *J. Power Sources* (In Press).
103. M. Lopez-Haro, L. Guétaz, T. Printemps, A. Morin, S. Escribano, P.-H. Jouneau, P. Bayle-Guillemaud, F. Chandezon and G. Gebel, *Nature Communications*, **5**, 5229 (2014).
104. C. Ziegler, S. Thiele and R. Zengerle, *J. Power Sources*, **196**, 2094 (2011).
105. S. Zils, M. Timpel, T. Arlt, A. Wolz, I. Manke and C. Roth, *Fuel Cells*, **10**, 966 (2010).
106. H. Schulenburg, B. Schwanz, J. Krbanjevic, N. Linse, R. Mokso, M. Stampanoni, A. Wokaun and G. G. Scherer, *ECS Trans.*, **33**, 1471 (2010).
107. D. Bessarabov and A. Hitchcock, *Membrane Technology*, **2009**, 6 (2009).
108. A. Tkachuk, F. Duewer, H. T. Cui, M. Feser, S. Wang and W. B. Yun, *Z. Kristallogr.*, **222**, 650 (2007).
109. S. H. Lau and et al., *J. Phys. Conf. Ser.*, **152**, 012059 (2009).
110. P. R. Shearing, J. Gelb, J. Yi, W. K. Lee, M. Drakopolous and N. P. Brandon, *Electrochem. Commun.*, **12**, 1021 (2010).
111. A. S. Grader and A. B. S. AClark, Computations of Porosity and Permeability of Sparic Carbonate using Muti-Scale CT Images, in *International Symposium of the Society of Core Analysts*, Noordwijk aan Zee, The Netherlands (2009).
112. S. Litster, W. K. Epting, E. A. Wargo, S. R. Kalidindi and E. C. Kumbur, *Fuel Cells*, **13**, 935 (2013).
113. M. Secanell, K. Karan, A. Suleman and N. Djilali, *Electrochim. Acta*, **52**, 6318 (2007).
114. S.-M. Chang and H.-S. Chu, *J. Power Sources*, **161**, 1161 (2006).
115. N. Khajeh-Hosseini-Dalasm, S. Ahadian, K. Fushinobu, K. Okazaki and Y. Kawazoe, *J. Power Sources*, **196**, 3750 (2010).
116. S. Obut and E. Alper, *J. Power Sources*, **196**, 1920 (2011).
117. A. A. Shah, G. S. Kim, W. Gervais, A. Young, K. Promislow, J. Li and S. Ye, *J. Power Sources*, **160**, 1251 (2006).
118. T. Sousa, M. Mamlouk and K. Scott, *Chem. Eng. Sci.*, **65**, 2513 (2010).

119. N. P. Siegel, M. W. Ellis, D. J. Nelson and M. R. von Spakovsky, *J. Power Sources*, **115**, 81 (2003).
120. K. Broka and P. Ekdunge, *J. Appl. Electrochem.*, **27**, 281 (1997).
121. F. Jaouen, G. Lindbergh and G. Sundholm, *J. Electrochem. Soc.*, **149**, A437 (2002).
122. F. Gloaguen and R. Durand, *J. Appl. Electrochem.*, **27**, 1029 (1997).
123. P. K. Das, X. Li and Z.-S. Liu, *J. Power Sources*, **179**, 186 (2008).
124. M. L. Perry, J. Newman and E. J. Cairns, *J. Electrochem. Soc.*, **145**, 5 (1998).

2 In-Situ Measurement of Oxygen Transport Resistance Through the Thickness of a PEFC Diffusion Medium

2.1 Introduction

In this chapter, we present the in-situ characterization of oxygen transport through the diffusion medium (DM) of a working polymer electrolyte fuel cell (PEFC) using a commercial oxygen concentration microsensor. Using a minimally invasive sensor with a 25 μm tip, made from a pulled glass capillary, we measured the O_2 concentration at multiple points through the thickness of the cathode DM in an operating PEFC. We performed these measurements at different current densities and different values of relative humidity (RH), on multiple fuel cell builds. We then analyzed those concentration measurements to yield position-dependent transport properties through the DM thickness, and to find where liquid water condenses in the DM under different conditions. Finally, since the transport properties of a porous medium arise from its microstructure, we employed microscale X-ray computed tomography (micro-CT) to characterize the morphology of the DM and give further insight to the results of the oxygen concentration analysis. To our knowledge, only one other work has directly probed the oxygen concentration through the thickness of the DM using a microprobe, using a fiber-optic method requiring a larger sensor and a previously drilled hole.¹

2.2 Experimental Methods

2.2.1 Physical Setup for Microsensor Insertion

The oxygen microsensor used in this study (OX-25, Unisense A/S, Århus, Denmark) was made from a pulled glass capillary with a 25 μm tip. Internal to the sensor was a small electrochemical cell for measurements based on limiting current oxygen reduction reaction (ORR) measurement, including a “guard cathode” set back from the main working electrode designed to consume extraneous oxygen entering from behind. Figure 2.1a shows a photograph of the sensor, which was advanced forward in measured increments through the thickness of the cathode DM (the z axis) along a straight, through-thickness line using an experimental setup illustrated in Figure 2.1a-b. The measured steps forward in space were accomplished using a micromanipulator (MM-33RT, Warner Instruments, Hamden, CT) with a 10 μm resolution

Vernier micrometer handle for movement in the through-thickness (z , axial to the oxygen sensor) direction.

The PEFC hardware used in this study was a slightly modified 5 cm² fuel cell test fixture from Scribner Associates Inc (Southern Pines, NC), featuring a single serpentine channel 800 μ m in width and depth, in both the cathode and anode flow plates; the flow plates themselves are 12.7 mm thick. The membrane electrode assembly (MEA) was a catalyst-coated Nafion NR-211 membrane, with a cathode Pt loading of 0.3 mg/cm² (Ion Power, New Castle, DE). For this study, the active area was reduced to 5 cm² using adhesive, 25 μ m thick Kapton masks (DuPont, Wilmington, DE). On both the anode and cathode sides, we used Sigracet 10BC DMs (SGL, Wiesbaden, Germany), which are made from carbon felt with a nominal 80% porosity, coated with 5 wt% polytetrafluoroethylene (PTFE), and coated with a microporous layer on the side that faces the catalyst layer. The nominal thickness of the 10BC DM is 420 μ m. However, the thickness can vary significantly from that value. As we will describe later, we used micro-CT to determine these DMs to be about 300 μ m thick. Around the DMs, we employed 230 μ m thick PTFE/fiberglass gaskets on both sides during compression, leading to a roughly 30% compression. Note that despite the compression under the non-channel areas, it is typical for a DM to remain at its full, uncompressed thickness in the center of a channel of this width.²

Controlled by the micromanipulator, the O₂ microsensors entered the cathode via a 420 μ m through-hole to allow sensor entry. The through-hole was placed in the center of the 800 μ m inlet channel - the first pass before the serpentine channel turned. It was 15 mm from the channel inlet hole, or roughly 2/3 of the way along the channel before the first serpentine turn. The sensor through-hole was surrounded by a multi-step counter-sink, as illustrated in Figure 2.1d, to allow space for the larger rear body of the sensor and to allow visual contact for alignment of the sensor with the hole. The hole and counter-sinks shown in Figure 2.1d, along with matching large holes in the hardware's endplate and current collector plate, were the only modifications to the hardware. We verified that the modification did not affect cell performance significantly, as we will discuss below. A special mount ensured that the micromanipulator's z axis was parallel to the axis of the through-hole, and that the micromanipulator could not vibrate or move

independently of the PEFC hardware, as any false movements or vibrations could break the fragile microsensor.

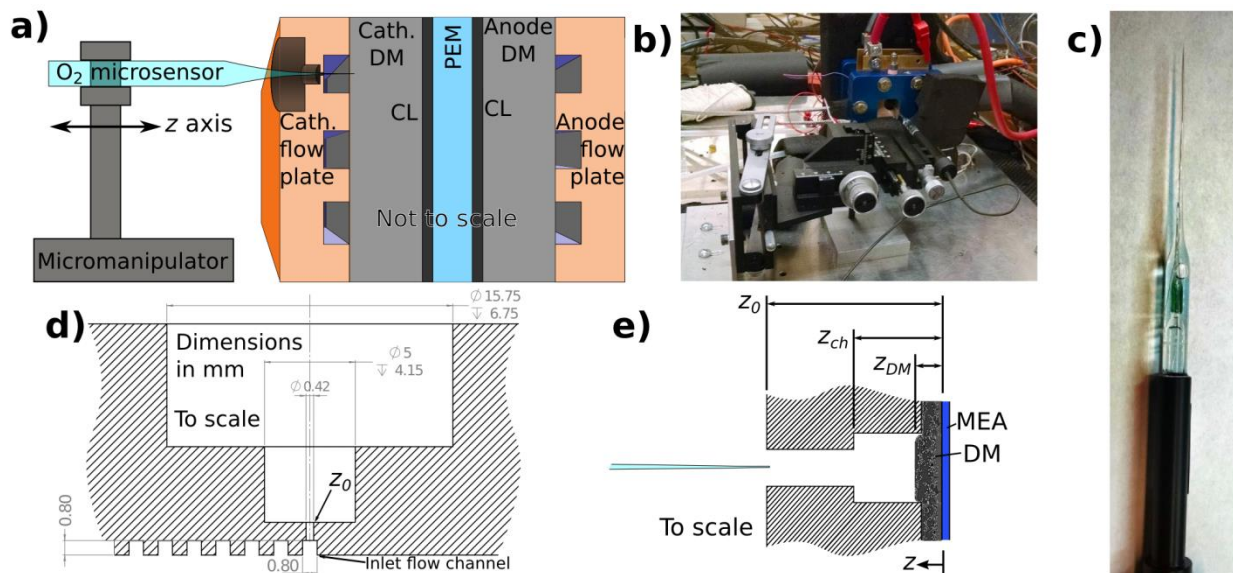


Figure 2.1 a) Schematic of oxygen microsensor penetrating into PEFC cathode. b) Photograph of physical setup for sensor and PEFC experiments. c) Photograph of the OX-25 oxygen microsensor. d) Dimensioned drawing of modifications made to the cathode flow plate. e) Detail schematic of sensor, through-hole, flow channel, and DM (to scale).

In-plane alignment of the sensor with the through-hole was accomplished with the X and Y (non-axial) controls of the micromanipulator using visual feedback, aided by a digital microscope (Dino-Lite AM-311S, AnMo Electronics, Taipei, Taiwan). When the tip was close to the through-hole, the X-Y alignment could also be verified by observing the sensor signal as it moved in X and Y – if nitrogen was flowing through the cathode channels, the through-hole would be emitting a jet of nitrogen, and the signal would be lowest when the sensor was in the proper X-Y position. Once the sensor was aligned, the through-thickness (z) position was established by noting the micrometer gauge's reading when the tip of the sensor was microscopically observed to be flush with the outer surface of the counter-sink, indicated by z_0 in Figure 2.1e. Following this, the sensor's position was known relative to the channel and the DM as it was stepped forward in the z direction. Based on the known geometry and using the z coordinate (beginning from the PEM/cathode catalyst layer interface) marked in Figure 2.1e, z_0 has a value of 2.03 mm, channel entry occurs at $z_{ch} = 1.03$ mm, the outer surface of the DM is

encountered at $z_{DM} = 0.32$ mm, and the DM terminates (and the catalyst layer is reached) at $z_{CL} = 0.02$ mm. As the schematic suggests, and as we will discuss below, the sensor's tip is significantly smaller than the characteristic pore size in the carbon fiber felt of the DM and should not significantly affect the DM's microstructure or transport. The sensor tip is approximately the size of 2 carbon fibers from the DM's carbon fiber phase, so its presence should not significantly affect oxygen transport in its vicinity compared to existing materials. The sensor can create a hole in the MPL, which will affect transport locally after the experiment is fully complete as we will discuss below, but holes and cracks on the order of 10-100 μm already exist naturally in MPLs.^{3,4}

2.2.2 Electrochemical Characterization of PEFC

Gases were humidified and delivered to the PEFC using a Scribner Associates e850 fuel cell test stand, which also controlled the temperature, voltage, and current of the cell. The PEFC was maintained at 60°C through the entirety of this work, except where otherwise noted. In order to achieve differential cell behavior despite the presence of the through-hole, we performed all experiments at a cathode air flow rate of 2 standard liters per minute (SLPM); the anode's hydrogen gas was supplied at 0.5 SLPM and always provided at the same RH as the cathode gas. Each MEA was conditioned on its first day of operation by 8 hours of voltage cycling at 0.8, 0.6, and 0.3 V, under 95% RH. Oxygen concentration experiments were performed under four different values of relative humidity: 62%, 72%, 83%, and 91%. For each of these RH cases, a new MEA was built, installed, conditioned, and characterized before the oxygen concentration measurements.

For each separate cell build, we verified that the through-hole modification to the cathode flow plate did not significantly affect cell behavior. We did this by measuring two separate polarization curves at 2 SLPM, one with the through-hole sealed by adhesive Kapton, and the other with the hole open to the environment. Similarly, we ensured differential cell behavior by measuring the PEFC current at 0.3 V as the cathode flow rate was stepped from 1.5 to 1.75 to 2 SLPM; this was also done once with the hole sealed, and again with the hole open.

2.2.3 Oxygen Concentration Measurement using Oxygen Flux Interrupt

After being positioned as described above, the oxygen microsensor was moved forward in the z direction (along its axis, deeper into the channel/DM) until it entered the channel (z_i in Figure 2.1b). After this point, oxygen measurements were taken every 150 μm through the channel. The z step between measurements was refined to 20 μm , beginning at the location ca. 60 μm away from the outer surface of the DM ($z \approx 400 \mu\text{m}$), and continuing through the rest of the experiment. At each position, without moving the sensor, oxygen concentration measurements were taken for 4 different PEFC current densities (i_{FC}) – 0.5, 1, 1.5, and 1.8 A/cm^2 , galvanostatically controlled to ensure constant flux. These currents were selected to represent widely varying levels of flux and of liquid water flooding (often prevalent at higher currents), while still being accessible in all PEFC builds and at all values of RH. After measuring c_{O_2} at all four PEFC currents, the sensor was advanced further into the DM.

The sensor itself has a signal that is based on the limiting current of the ORR within the sensor. However, the sensor's commercial software expresses its signal in units of mV, which is presumably the voltage across a sensing resistor inside the pico-ammeter that accompanies the sensor. Because of this, we will refer to the sensor signal as V_{sensor} , despite the fact that the c_{O_2} measurement inherently comes from a mass transport limited ORR current within the sensor. Note that the oxygen sensor's signal was being recorded constantly, at a sampling rate of 10 Hz, during the entirety of the experiment. The measurements of interest were extracted by careful logging of the time at which each PEFC current and z position occurred.

In this work, we employ an oxygen sensor operating at its limiting current. Normally, one would calibrate such a sensor beforehand according to known oxygen concentration (c_{O_2}) values, and this calibration curve would be used later to determine unknown c_{O_2} values. However, one issue prevents us from simply detecting the limiting current and correlating it to calibration measurements taken at the PEFC's open circuit. The sensor (being on the cathode side) is subject to the fluctuations in relative humidity and temperature as the PEFC operates and produces water and heat. The sensor's signal changes due to temperature and RH, as well as day to day, as indicated both in the sensor's manual and from our own data. Figure 2.2a shows the sensor's variation from RH and temperature without PEFC current. The curve with varying RH was taken

at a constant 60°C, and the varying temperature curve was taken at a constant 72% RH. The fact that the two curves do not overlap at 60°C and 70% RH illustrates the possible day-to-day variation in the sensor as well.

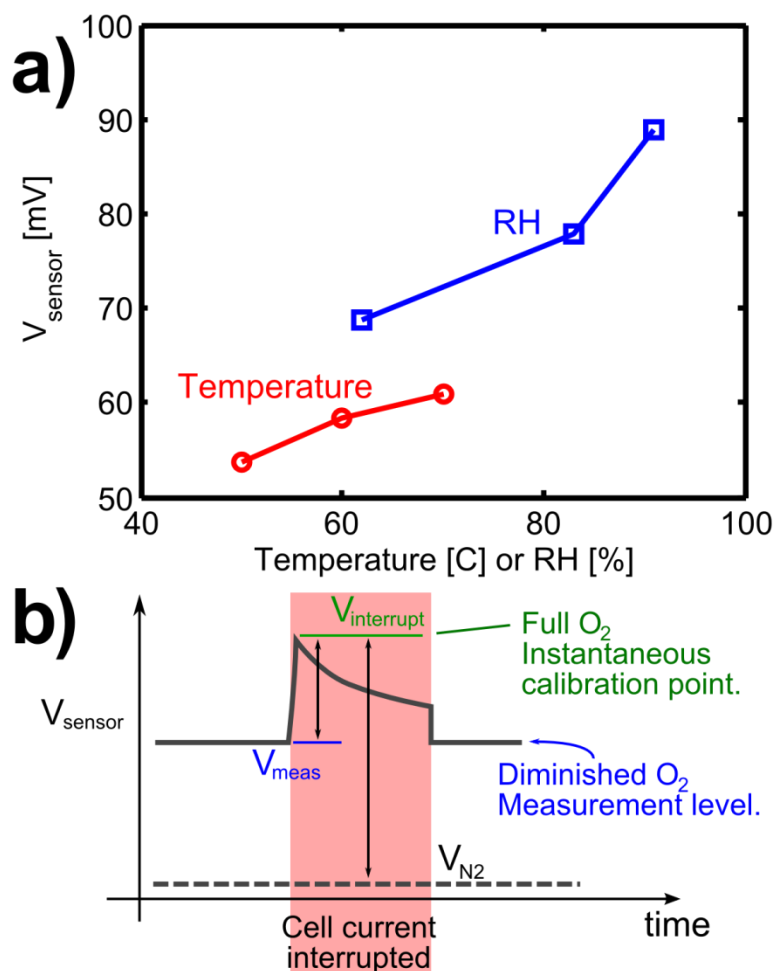


Figure 2.2. a) Sensor signals with the PEFC at open circuit, at different values of RH (at 60°C) and temperature (at 72% RH). b) A typical waveform of the sensor signal during O₂ flux interrupt. The difference between V_{meas} and V_{N_2} represents the measured O₂ concentration, and the difference between $V_{\text{interrupt}}$ and V_{N_2} is the instantaneous calibration point, representing the O₂ concentration of the channel gas.

Therefore, when the PEFC generates current, two competing effects confound pre-calibrated measurements: the increased RH and temperature increases ORR current at the sensor tip, while the diminished concentration of oxygen (which we wish to measure) reduces ORR

current. In another manner of thinking, as the RH and temperature change, the sensor's calibration curve changes as well. In order to separate these effects, we interrupt the PEFC's current in an approach resembling the current interrupt method for measuring Ohmic voltage drops in a PEFC. One can think of this method as re-calibrating the sensor at every measurement. When the PEFC current is interrupted, the concentration of oxygen is rapidly restored to channel levels in a matter of milliseconds, while changes in the sensor's behavior due to RH and temperature occur over many seconds. The result: an interruption of PEFC current provides us with an instantaneous calibration point $V_{interrupt}$ that represents the sensor's signal at $c_{O_2}(\text{channel})$, but under the hydration and temperature conditions it is actually experiencing. Herein, the $c_{O_2}(\text{channel})$ is constant due to a very high stoichiometric ratio and a short air residence time in the channels. In these experiments, each PEFC current hold lasted 3 or 4 minutes, which we found to be more than enough time for the cell and the sensor to reach a steady state in high and low humidity cases, respectively. Each current interruption (where the PEFC was switched to open circuit) lasted 5 seconds.

Key to these measurements is a zero-oxygen reference point for the sensor signal. Here we use the sensor's signal when there is only humidified nitrogen in the cathode, and the PEFC is at open circuit. This value, V_{N_2} , is taken in a separate, prior experiment from the oxygen interrupt measurements. Its value is typically on the order of 1/100th of the sensor's signal in oxygen, and we have found it to be very consistent over a wide range of RH and temperature. Thus, we take V_{N_2} to be a constant value throughout each experiment.

As illustrated in Figure 2.2b, the difference between V_{meas} (the pre-interrupt sensor signal) and V_{N_2} corresponds to the value of c_{O_2} we desire to measure, while the difference between $V_{interrupt}$ and V_{N_2} is a measure of c_{O_2} in the channel and is used as an instantaneous calibration point. Given high flow rate and the short residence time of the air in the channels, this is also the inlet oxygen concentration (i.e. that of humidified air). The expression used to calculate the dimensionless concentration as non-dimensionalized by the channel concentration, $\overline{c_{O_2}} = c_{O_2} / c_{O_2,channel}$, is:

$$\overline{C_{O_2}} = \frac{V_{meas} - V_{N_2}}{V_{interrupt} - V_{N_2}} \quad (2.1)$$

2.2.4 Micro-CT of Diffusion Medium

Since a porous medium's transport properties arise from its microstructure, interpreting the results of the oxygen concentration measurements can be aided by knowledge of microstructural properties. For this reason, we characterized the 3D microstructure of the SGL 10BC DM used in this study using micro-CT. We prepared a 1 mm diameter cylindrical sample of the whole thickness of the DM using a 1 mm inner diameter Miltex Biopsy Punch (Integra Miltex, Plainsboro, NJ). The sample was imaged using a Zeiss Xradia 520 Versa laboratory micro-CT system (Zeiss Xradia, Pleasanton, CA). This system generated a broadband "pink" X-ray beam with an accelerating voltage of 50 kV, and imaged the sample using a 10x objective. The sample was imaged across 360° of rotation with 1601 steps, at 1 second exposure time per angle step. The 1601 images were reconstructed using Zeiss Xradia proprietary software, and segmented and analyzed using Avizo (FEI, Hillsboro, OR) and MATLAB (Mathworks, Natick, MA).

2.3 Results and Discussion

2.3.1 Micro-CT of Diffusion Medium

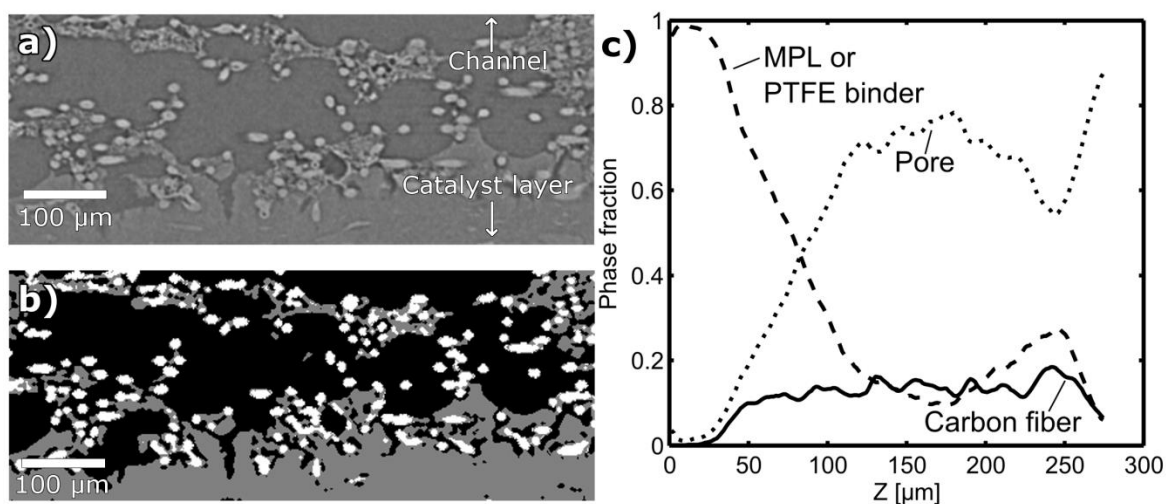


Figure 2.3 Results of micro-CT scan of 10BC DM sample, including a) a virtual tomography slice of the 3D reconstruction; b) a virtual slice of the segmented 3D reconstruction, showing the fiber phase (white), the MPL or PTFE-binder phase (grey), and the pore phase (black); c) the distribution of phase fractions as a function of the z coordinate through the DM.

The micro-CT reconstruction of the 10BC DM studied here is shown in Figure 2.3. The 3D reconstruction of the cylindrical sample was cropped to a rectangular prism of $640 \times 700 \times 275 \mu\text{m}$ before phase segmentation. The actual DM extends slightly larger than this in the z direction, to about $300 \mu\text{m}$ thick, but the bottom-most $25 \mu\text{m}$ portion was cropped out as it included some artefacts of sample preparation and mounting. We then segmented the raw grayscale reconstruction into 3 phases – fibers, MPL/PTFE-binder, and pore. A virtual slice of the data before and after segmentation can be seen in Figure 2.3 (a) and (b), respectively. Note that the MPL phase has a microporosity of roughly 40%,⁵ which was not captured by the $1.5 \mu\text{m}$ voxel scan here; instead, it is presented as one seemingly solid phase. The PTFE binder on the carbon fiber felt, on the other hand, has a sub-porosity that is somewhat captured by the micro-CT. The microporosity of the PTFE binder not captured here is minor enough, and the total phase fraction of the PTFE binder is low enough, that it does not significantly impact the overall porosity. The MPL and the PTFE binder both had a similar intensity in the reconstruction, so they are both segmented as the same phase, though they are not the same material. The MPL

material can be distinguished from the PTFE binder material qualitatively, e.g. in Figure 2.3a; the MPL generally does not extend beyond about $z = 120 \mu\text{m}$.

After segmenting the image, we plotted versus the z axis the phase fractions of the MPL/PTFE-binder phase, the fiber phase, and the pore phase. The results are in Figure 2.3c. As expected, the MPL takes up almost 100% of the volume on the MPL-side of the DM – because of the MPL's sub-porosity, the actual porosity in this region would be roughly 40%, comprised of small pores in which Knudsen diffusion is significant. We found that rather than a distinct interface, the MPL tapers off over a fairly wide (50-100 μm) range. Works by Fishman and Bazylak⁴ and Wargo et al.⁵ on the 10BC DM show a similar distribution. Following the tapering off of MPL content, there is a particularly empty region in the middle of the carbon fiber region, followed by a particularly dense fiber/PTFE region at the outer edge of the DM, similar to that observed by Wargo et al.⁵

2.3.2 Electrochemical Characterization of PEFC

Initial electrochemical characterization of each PEFC build successfully verified that the presence of the through-hole did not significantly affect cell behavior. Figure 2.4 presents polarization curves for each of the 4 values of RH studied here, on the 4 different MEAs used. Some variation can be seen due to the particular MEA build – for example, the MEA used in the 72% RH case exhibits slightly lower activity than the others. However, all of the MEAs at all of the RH conditions perform adequately for these experiments, considering that the cell's current density is controlled galvanostatically to ensure consistent oxygen flux. Moreover, all of the polarization curves show negligible difference between the sealed and open-hole case, indicating little to no effect from the modification to the hardware at this flow rate. The inset in Figure 2.4 shows the PEFC currents (normalized for each case by that case's maximum value) at 0.3 V as the cathode gas flow rate is increased. All 4 RH cases with open and sealed holes are shown. All of the curves lie nearly on top of each other, with the highest flow rate of 2 SLPM giving only 5% more current density than the second-highest of 1.75 SLPM. This indicates that the PEFC is operating as a differential cell at flow rates of 2 SLPM, whether the through-hole is open or sealed.

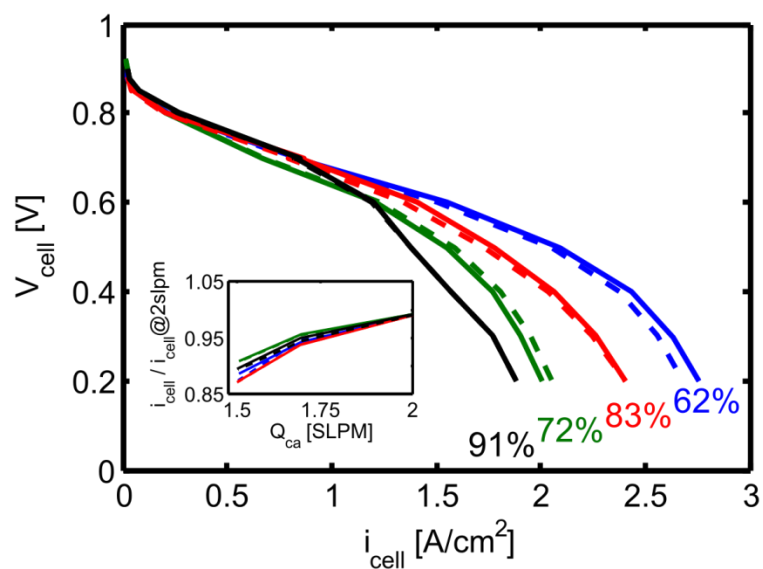


Figure 2.4 Polarization curves for all cell builds at all RH values studied, at a cathode flow rate of 2 SLPM, with the through-hole sealed (dashed line) and open (solid line). Inset is the PEFC current density (normalized by the max value in each case) at 0.3 V, at different cathode gas flow rates, with both sealed (dashed line) and open hole (solid line) cases lying nearly on top of each other.

2.3.3 Oxygen Concentration Measurements

As the oxygen microsensor advanced through the channel and the DM, the sensor's signal was logged constantly as oxygen flux interrupt procedures were performed through the channel and the DM. At times we found erratic, anomalous sensor behavior that was indicative of the presence of liquid water. Figure 2.5a shows an example of a normal sensor signal during all 4 current holds of an oxygen flux interrupt procedure at one z position. The sensor signal is steady as the PEFC holds current, and quickly jumps up to the calibration value corresponding to $c_{O_2}(\text{channel})$ when the PEFC is switched to open circuit. Figure 2.5b shows an example of erratic, anomalous sensor behavior indicative of liquid water. This sensor behavior occurs only within the DM, and it occurs more often at higher values of RH and at higher PEFC currents – all consistent with liquid water flooding. The erratic behavior ceases within a few seconds when the PEFC current is stopped, which is consistent with the liquid water clearing away once it is no longer being produced. The anomalous sensor signal in liquid water makes the extraction of a c_{O_2} value impossible – not only from a signal processing standpoint, but also because the liquid water significantly increases the timescale for c_{O_2} to return to the channel calibration value when

PEFC current is interrupted. Therefore, in the proceeding analysis, we consider the z -positions, currents, and RH values where the sensor exhibits erratic behavior to be flooded zones in the DM, and do not express a particular c_{O_2} value for the flooded points.

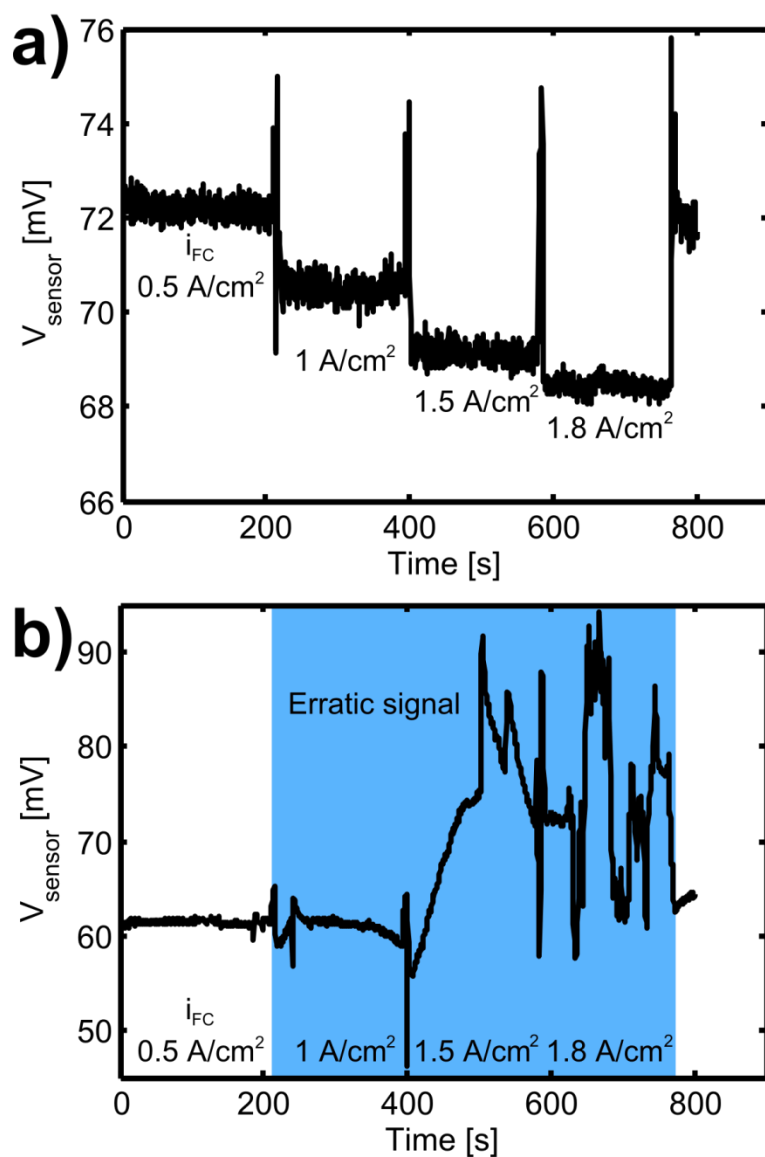


Figure 2.5 Anecdotal time series of oxygen microsensor signal during oxygen flux interrupt procedure, in (a) a case with no liquid water (83% RH, near the outer surface of the DM) and (b) a case with significant liquid water flooding at all currents (91% RH, just within the DM).

Anecdotally, in the 72% RH experiment performed in this work, the sensor was advanced all the way through the DM's microporous layer (MPL). After the break-through and after all

c_{O_2} readings were complete, the sensor's readings during withdrawal from the cell indicated liquid water at all but the lowest current density, which was different from the previous behavior when the sensor was first advancing through the DM. We believe that the sensor had created a new 25 μm hole in the hydrophobic MPL that allowed facile condensation and outflow of water. Note that MPLs naturally contain cracks and holes larger than this, which may act as arteries of water outflow.^{3,6,7} To test this hole-creation hypothesis, during the same day but after the 72% RH experiment, we lowered the PEFC's RH to 62%. The erratic signal ceased. We measured c_{O_2} at several z locations through the DM, including within the MPL, and all of the resulting c_{O_2} measurements matched the non-flooded measurements from the 72% RH experiment. This demonstrated not only that the through-hole had created increased flooding in that region, but also that in the absence of liquid water, the hole in the DM created by the sensor did not affect c_{O_2} through the DM. As further evidence for this, in other dry cases, the sensor could obtain repeatable readings when retreating back to an earlier z location, so long as the MPL had not been broken through. Considering that the existence of a hole in the DM exacerbates flooding, this method is particularly well-suited to determine the location of liquid water in the DM compared to the oxygen probing method of Kobayashi et al.,¹ which required a 100 μm hole drilled through the DM prior to the experiment.

The oxygen flux interrupt procedure yielded measurements in four cases of RH (each with a separate MEA), and at four different PEFC currents, all plotted together in Figure 2.6. Each concentration curve indicates where liquid water was encountered, if at all, in that particular case. If flooding was observed, it persisted at every further measurement point deeper into the DM, but as noted previously, the flooding ceased when PEFC current was ceased. Also included in Figure 2.6 is a virtual 2D slice of the 3D micro-CT reconstruction of the 10BC DM used in this study, shown to scale with the x-axis, to aid in interpreting the c_{O_2} profiles. We also note here that the 72% RH case was the first experiment performed. In this case, the sensor was able to penetrate all the way through the MPL, as described above. That particular commercial oxygen sensor later broke in a separate experiment, and was replaced with another sensor of the same type. The sensors are made to order by the vendor. The second sensor was more delicate and could not penetrate through the MPL without straining, which caused an internal short

circuit that temporarily made measurement impossible. For this reason, the 62% RH curves cease at roughly $z = 100 \mu\text{m}$, where the sensor is first encountering the MPL. The 83% and 91% experiments encountered the same short circuit phenomenon, but it is not evident in Figure 2.6 because liquid water flooding set in before the sensor reached the depth of the MPL.

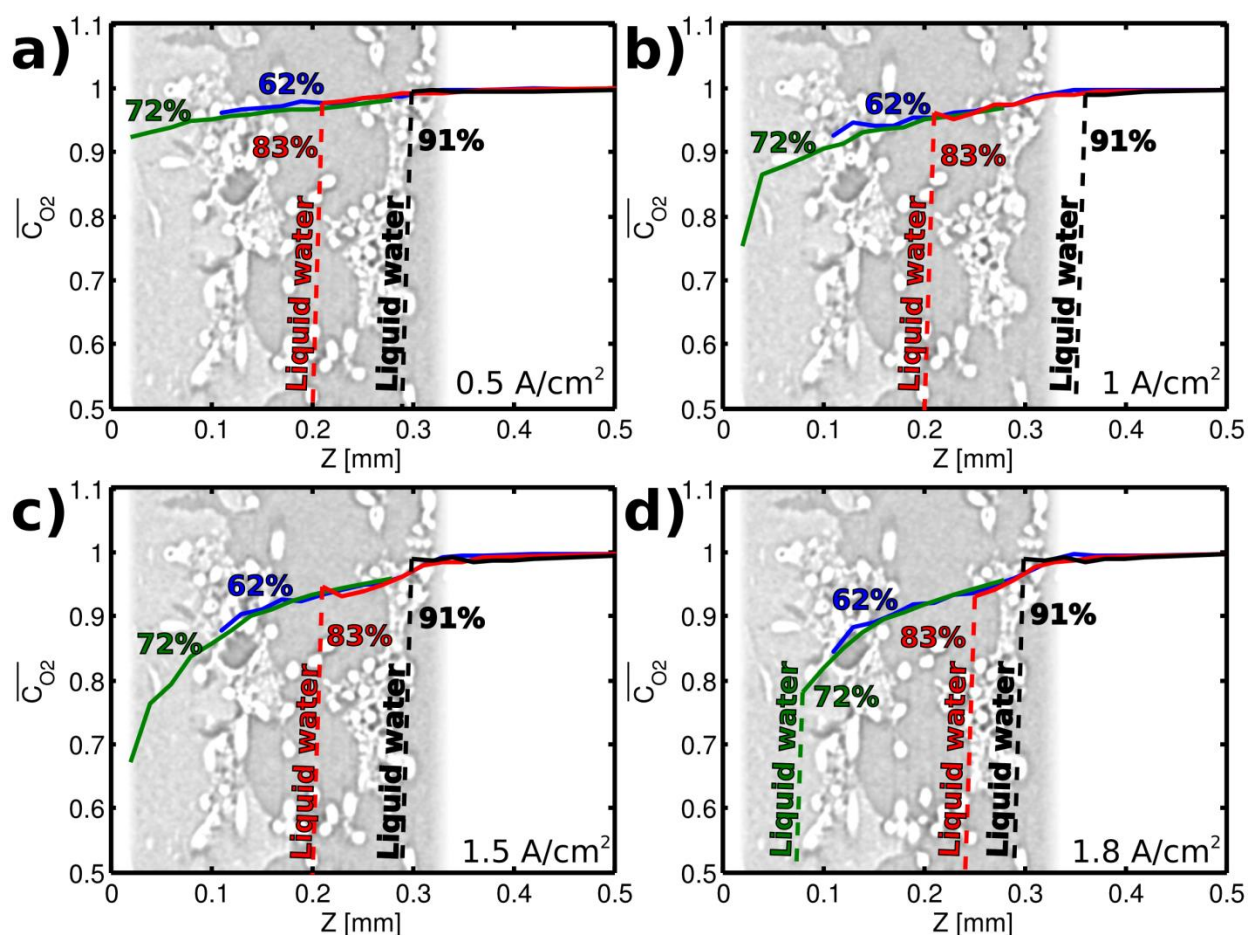


Figure 2.6 Plots of dimensionless c_{O_2} at four different values of RH, and at four different PEFC currents, indicated on each figure. A virtual tomography slice from micro-CT of the DM is included, to scale, to illustrate microstructural features affecting the concentration profiles.

Other than the onset of liquid water, the different RH values' c_{O_2} curves lie on top of each other in each of Figure 2.6's sub-plots. Despite the sensor's behavior changing from day to day, and despite the DM and MEA being changed between each RH case, the c_{O_2} measurements were repeatable across space (z) and PEFC current. Consistent transport properties between builds and RH values are expected – the DM's microstructure does not change significantly based on RH,

other than liquid water flooding. This indicates a success of the method in measuring what we intended. The valuable output of the results shown in Figure 2.6 are the *in-situ* measurement of the consistent, non-flooded transport properties; and the *in-situ* measurement of where and under what conditions liquid water flooding occurs in the DM.

A detailed inspection of the c_{O_2} profile at the interface between the channel gas and the DM surface can yield a mass transfer coefficient h_m for the mass transfer boundary layer there. We performed this calculation based on the definition $\dot{n}_{O_2} = h_m(c_\infty - c_{surf})$, using the data from the 62% RH and 83% RH cases. The oxygen flux \dot{n}_{O_2} is known from the cell current density i_{FC} using Faraday's law of electrolysis. The concentrations c_∞ and c_{surf} are the values of c_{O_2} in the channel (known) and at the surface of the DM (measured), respectively. The 62% RH and 83% RH cases agreed well across all current densities, and yielded an average mass transfer coefficient h_m of 0.14 m/s, with a standard deviation of 0.02 m/s.

Moving deeper into the DM, the local slope dc/dz at any point (where there is not flooding) allows us to calculate the formation factor K_{form} by which the microstructure reduces the diffusivity, according to the following variation of Fick's law of diffusion:

$$\dot{n}_{O_2} = K_{form} D_{O_2/N_2} \frac{dc}{dz} \quad (2.2)$$

where, again, the oxygen flux \dot{n}_{O_2} is known from the cell current density i_{FC} according to Faraday's law of electrolysis; and the binary diffusivity D_{O_2/N_2} is 0.252 cm²/s, a value corrected for temperature from the CRC Handbook.⁸ In other words, K_{form} in a porous medium is the ratio of the effective diffusivity to the binary diffusivity, or $K_{form} = D_{eff} / D_{O_2/N_2}$. In porous medium theory, K_{form} is often approximated using the ratio of the porosity ϵ to the tortuosity factor τ , or sometimes more simply using the Bruggeman factor $\epsilon^{1.5}$. These approximations of K_{form} do not incorporate the effect of Knudsen diffusion or the 3D effects of diffusion bottlenecks. For this reason, we keep with the simplest version, K_{form} , as derived from these experimental measurements. Figure 2.7 presents the values of K_{form} as a function of location in the DM for the four cases with sufficiently high O₂ flux and with no liquid water flooding. All four curves agree well with each other, despite the changing RH and current density. Values of K_{form} that were

calculated from un-flooded i_{FC} cases of 0.5 and 1 A/cm² agreed in value, but contained significant non-systematic variation due to the lower signal and hence are not shown.

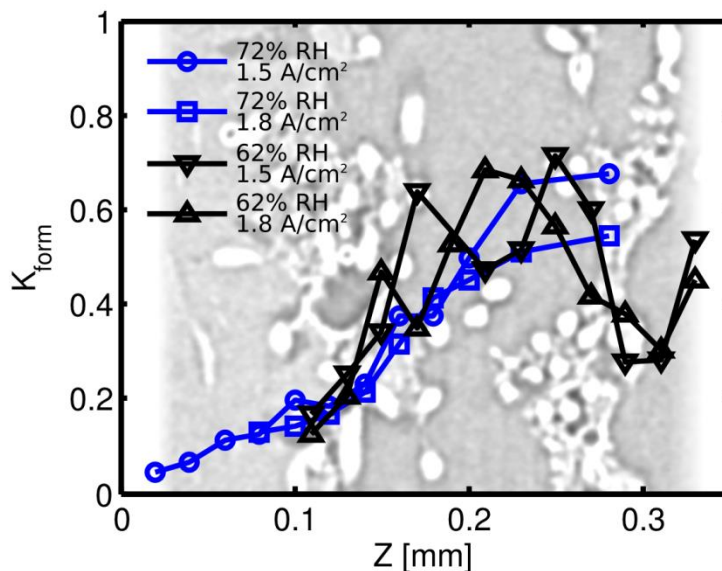


Figure 2.7 Formation factor K_{form} for 62% and 72% RH cases at PEFC current densities of 1.5 and 1.8 A/cm². A virtual tomography slice from micro-CT of the DM is included, to scale, to illustrate microstructural features affecting the values of K_{form} .

The K_{form} curves shown in Figure 2.7 have several notable features. Note that the 72% RH curves do not extend as far to the right in the figure (higher z values) because we advanced by too large of a z -step when first entering the DM during that experiment. The 62% RH curves do not extend through the MPL (to the left) due to the previously described difficulty in penetrating the MPL in that case. Moving from right to left in Figure 2.7, the 62% RH case shows a significantly lower K_{form} upon initial entry into the DM, before moving to higher values. Lower values of K_{form} mean a higher transport resistance, due to lower porosity, more tortuous transport pathways, or other changes in diffusion behavior (e.g. Knudsen diffusion). The lower K_{form} at the DM entrance indicates some initial transport blockage close to the outer surface of the DM that clears up deeper into the DM. In our micro-CT reconstruction of a 10BC sample, we did in fact observe a matching feature – a significantly lower porosity closest to the outer surface at a corresponding location (Wargo et al.⁵ observed a similar feature in a 10BC sample). This can be seen both in the background of Figure 2.7 and in the micro-CT analysis presented in Figure 2.3. There is a higher fraction of PTFE binder (added by the manufacturer to reduce flooding)

near the outer surface of the DM that significantly reduces porosity. The PTFE binder does not appear to have penetrated through the entire carbon fiber felt portion of the DM, leading to a high-porosity region in the middle of the DM between the low-porosity outer surface and the MPL region.

The K_{form} results from the 72% RH case have similar values to the 62% case, ranging mostly from 0.5 to 0.7 in the core of the carbon fiber region. The measurements in this case extend farther into the DM, into the MPL region. There is a gradual decline in K_{form} consistent with the MPL transition region seen in Figure 2.3. In the core of the MPL, the formation factor drops to the 0.1 – 0.2 range. When we compare the formation factor with the porosity distribution in Figure 2.3, it is clear that the formation factors follow a similar trend, but are consistently lower than the porosity. This is expected, as formation factor depends on a number of factors – porosity, tortuosity, and other transport effects like pore size dependent Knudsen diffusion and 3D bottlenecks in diffusion.⁹ For example, the K_{form} values in the carbon fiber phase, not including the extra dense region near the outer surface, average to about 0.55, compared to a porosity of roughly 0.75 in that region. A common expression for the formation factor is the porosity divided by the tortuosity factor, where the tortuosity factor is the square of the average actual transport pathway divided by the straight-line pathway through a porous medium.⁹ If we employ the tortuosity factor of $(1.07)^2$ found by Wargo et al.⁵ for the carbon fiber phase, we see that the two values do indeed match up quite well, with the predicted K_{form} being 0.61. If we include the extra dense region near the outer DM surface, our average K_{form} is closer to 0.5, which agrees well with the structural diffusivity factor K_{SD} (defined similarly to K_{form}) of 0.45 (which included a similar dense outer surface region) found by Wargo et al.⁵

The relationship between K_{form} and porosity is somewhat different in the MPL, due to the smaller pore sizes. MPLs have pores on the order of 100 nm.⁵ At this range of pore size, gas diffusion occurs in the Knudsen transition regime, and the effective binary diffusivity is reduced roughly in half according to the Bousanquet formulation for transition-regime diffusion.⁹ Furthermore, the MPL's micropores are significantly more tortuous than the carbon fiber phase.⁵ If we examine only the values of K_{form} in the core of the MPL, which average to approximately 0.12, we can assume that this corresponds with the nearly 100% MPL region in Figure 2.3. Using

the MPL's sub-porosity of 0.42 and tortuosity factor of $(1.33)^2$ found by Wargo et al., we find that the formation factor without considering Knudsen diffusion should be roughly 0.24. However, when directly measuring the concentration and the flux and calculating K_{form} , as we have in this study, we inherently lump the Knudsen penalty to the binary diffusivity into the apparent formation factor. In other words, the K_{form} we have indirectly measured already includes a roughly 50% penalty due to being in the Knudsen transition regime. If we consider the MPL porosity of 0.42, the tortuosity factor of $(1.33)^2$, and the Knudsen penalty of roughly one half, the expected K_{form} becomes about 0.12, which agrees well with our measured value here.

To summarize, we have tabulated our average value of K_{form} in the MPL region and the carbon fiber region, but not K_{form} in the entire DM – since oxygen transport resistance is dominated by the MPL, it does not make sense to simply average K_{form} through the entire DM, only in each sub-layer that has a consistent microstructure. Instead, we have also calculated the oxygen transport resistance R_{O_2} for the entire DM, and for those same sub-regions, based on an electrical resistor analogy used with Fick's law of diffusion:

$$R_{O_2} = \frac{\Delta c_{O_2}}{\dot{n}_{O_2}} \quad (2.3)$$

The analogy used to derive R_{O_2} is similar to Darcy's law – both use a medium-dependent coefficient to describe the loss in concentration (or pressure in Darcy's law) incurred by flux through a porous medium. Functionally, R_{O_2} is also the inverse of the mass transfer coefficient used in mass transport on a surface.

Table 2.1 presents the results, with K_{form} averaged from the cases presented in Figure 2.7, and R_{O_2} calculated from the concentrations in the 62% and 72% RH experiments in Figure 2.6. Note that the values for R_{O_2} in the sub-regions do not exactly add up to the total value because R_{O_2} is not reported in the MPL/carbon fiber transition zone. The results tabulated here compare reasonably with several other works that have measured the overall oxygen transport resistance through the DM as a whole. For comparison, Chan et al.¹⁰ measured K_{form} through an MPL-free SGL 10BA DM to be 0.36, which is reasonably close to the value of 0.5 for the carbon fiber region in Table 2.1 (the 10BA is identical to the 10BC without an MPL). Caulk and Baker¹¹ used limiting current methods to measure a value of roughly 50 s/m for R_{O_2} , at atmospheric pressure,

in an operating PEFC; however, this was for a slightly thinner, carbon-fiber-only Toray 060 DM. Beuscher¹² used *in-situ* limiting current methods to measure an R_{O_2} of 24 s/m for a CARBEL DM, which is also MPL-free and roughly 230 μm thick – this would also be comparable to the carbon fiber region in the this work and agrees well with the corresponding value of 20 s/m in Table 2.1.

Table 2.1: Summary of K_{form} and R_{O_2} Values

Region (z range)	Average dry K_{form}	Average dry R_{O_2} [s/m]
Entire DM (20 – 320 μm)	-	65
MPL (20 – 100 μm)	0.12	41
Carbon fiber (150 – 320 μm)	0.5	20

The oxygen concentration profiles in Figure 2.6 also illustrate where liquid water flooding begins and under what conditions. We have collected the z locations where the sensor first encountered flooding in each given case; Figure 2.8 presents those locations for all values of PEFC current, and for all values of RH except for 62% RH, which had no flooding at all. Once flooding was encountered, the flooding behavior returned at each deeper point in z at that value of i_{FC} for the remainder of that experiment. However, within the same experiment, a lower or even a higher current might still not show flooding until a deeper z location, or perhaps never at all (as in the case of the lower currents in the 72% RH experiment). In other words, experimentally, the flooding was a space, RH, and PEFC current dependent phenomenon with no apparent memory for the previous value of i_{FC} .

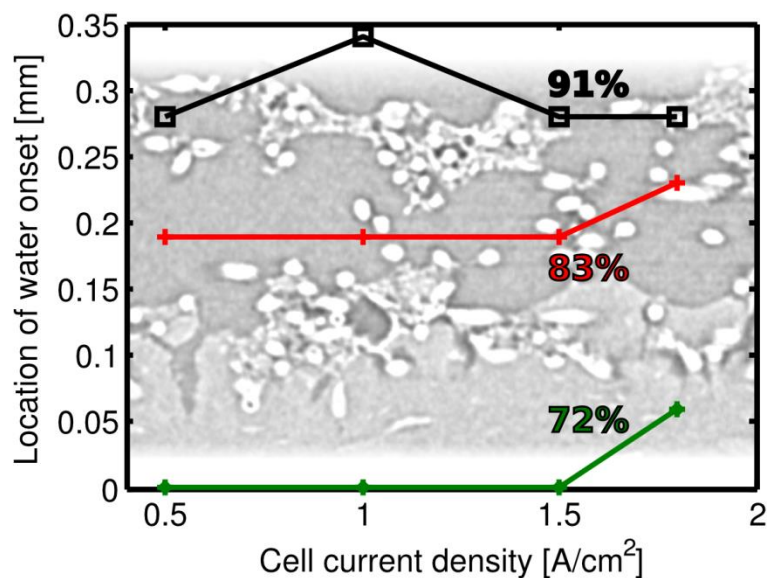


Figure 2.8 Location of water onset at different values of RH, plotted versus PEFC current density. Location values of 0 indicate no flooding at all. A virtual tomography slice from micro-CT of the DM is included, to scale, to illustrate the location of flooding with respect to microstructural features.

Figure 2.8 shows that at 91% RH, liquid water flooding was present at the outer DM surface and continued throughout the DM thickness. The 83% RH case shows liquid water flooding at all PEFC currents, with all of it beginning within the highly porous zone in the middle of the carbon fiber layer. Finally, only the highest current of 1.8 A/cm² exhibited any flooding in the 72% RH experiment – the flooding set on within the MPL region. This is an unexpected finding, and could indicate that the sensor was passing through or near a pore or a crack, where liquid water is likely to be found.³ Our measurement of the point of water onset at 91% RH and a lack thereof at 62% RH agrees with LaManna et al.'s¹³ neutron radiography work measuring water distributions in PEFCs, which show liquid water throughout all of the DM other than the MPL in 95% RH, and nearly no liquid water at 50% RH. On the other hand, Eller et al.¹⁴ observed significant liquid water throughout the DM even at 40% RH using synchrotron micro-CT; however, that group also found the synchrotron beam to have significant effects on the PEFC behavior and water content.¹⁵ Another neutron radiography study by Fu et al.¹⁶ found less liquid water within the DM's carbon fiber core at 95% RH, but a significant uptick in liquid water content at the outermost surface of the DM, consistent with our observation of outer DM surface flooding at 91% RH. Yet another neutron radiography study by Kotaka et al.¹⁷ found at

100% RH significant liquid water in the highly porous core of the carbon fiber layer that reduced towards the outer surface, possibly due to physical occlusion of the water due to the lower porosity we see in Figure 2.3 of the present work. All of these studies employ conditions and DM materials that are inconsistent with this study, and none of them study an intermediate humidity like 83%, where we observed no flooding until the highly porous core of the carbon fiber layer. However, it is worth noting that other in-situ studies of through-plane water distributions in PEFC DMs at high RH have found significant liquid water throughout at least the carbon fiber portion of the DM, a phenomenon we have mapped out in space, RH, and PEFC current in Figure 2.8. We also note again the excessively high air stoichiometry in this work, which has the effect of reducing liquid water accumulation. This means that at lower cathode stoichiometry ratios, flooding would most likely be as or more prevalent than what we measured here.

2.4 Summary

In this chapter, we used a commercially available oxygen microsensor with a 25 μm tip to measure the oxygen concentration profile at 20 μm resolution through the thickness of a 10BC DM in an operating PEFC cathode. We analyzed the resulting concentration profiles alongside a microstructural characterization using micro-CT. From those measurements, we calculated a surface mass transfer coefficient, and a distribution of the formation factor for diffusion through the DM that agrees with microstructural properties in this work and others. We found that, at least with the high stoichiometry used in this work, liquid water flooding occurs throughout the DM when the cathode gas is 91% RH; it begins within the core of the carbon fiber layer at 83% RH; it only occurs at high currents at 72% RH; and no flooding occurs at all at 62% RH.

2.5 References for Chapter 2

1. T. Kobayashi et al., in *226th Meeting of the Electrochemical Society*, p. 1158 (2014).
2. I. Nitta, T. Hottinen, O. Himanen, and M. Mikkola, *J. Power Sources*, **171**, 26 (2007).
3. I. V. Zenyuk, R. Taspinar, a. R. Kalidindi, E. C. Kumbur, and S. Litster, *J. Electrochem. Soc.*, **161**, F3091 (2014).
4. Z. Fishman and A. Bazylak, *J. Electrochem. Soc.*, **158**, B846 (2011).
5. E. a. Wargo, V. P. Schulz, A. Çeçen, S. R. Kalidindi, and E. C. Kumbur, *Electrochim. Acta*, **87**, 201 (2013).
6. S. Litster, D. Sinton, and N. Djilali, *J. Power Sources*, **154**, 95 (2006).
7. J. Lee, J. Hinebaugh, and a. Bazylak, *J. Power Sources*, **227**, 123 (2013).
8. D. R. Lide, *CRC Handbook of Chemistry and Physics*, 94th Edition, 2013-2014, p. 2616, (2013).
9. S. Litster, W. K. Epting, E. A. Wargo, S. R. Kalidindi, and E. C. Kumbur, *Fuel Cells*, **13**, 935 (2013).
10. C. Chan, N. Zamel, X. Li, and J. Shen, *Electrochim. Acta*, **65**, 13 (2012).
11. D. a. Caulk and D. R. Baker, *J. Electrochem. Soc.*, **157**, B1237 (2010).
12. U. Beuscher, *J. Electrochem. Soc.*, **153**, A1788 (2006).
13. J. M. Lamanna, S. Chakraborty, J. J. Gagliardo, and M. M. Mench, *Int. J. Hydrogen Energy*, **39**, 3387 (2014).
14. J. Eller et al., *J. Electrochem. Soc.*, **158**, B963 (2011).
15. J. Eller et al., *J. Power Sources*, **245**, 796 (2014).
16. R. S. Fu et al., *J. Electrochem. Soc.*, **159**, F545 (2012).
17. T. Kotaka, Y. Tabuchi, U. Pasaogullari, and C.-Y. Wang, *Electrochim. Acta*, **146**, 618 (2014).

3 In-situ Thin-Film Microsensor for Characterizing Oxygen Transport in the Diffusion Medium

3.1 Introduction

Knowledge of the oxygen concentration at the interface between the diffusion medium (DM) and the catalyst layer (CL) is an important piece of understanding the role of DM-level losses versus electrode-level losses. However, the oxygen concentration at this interface during operation is difficult to verify from ex-situ characterizations and modeling because of the complex distributions of temperature, compression, current density, and liquid water saturation. To our knowledge, there has been no prior direct oxygen concentration measurement at this interface. This chapter concerns a sensor and method designed to make such measurements *in-situ*. We present a thin-film sensor that employs the oxygen flux interrupt technique detailed in Chapter 2. This method and sensor combination can be applied to any PEFC electrode with a sufficiently low Ohmic drop, and with further development of the sensor, potentially any PEFC electrode at all.

3.2 Sensor Concept

The sensor we fabricated (Figure 3.1) consists of thin films ($\sim 1.5 \mu\text{m}$) of an insulating material sandwiching a thin layer ($\sim 1 \mu\text{m}$) of cast Nafion ionomer. Within the sandwich is a conducting (metal, in this case Pt) layer leading to a small (order of $100 \mu\text{m}$ diameter) spot of Pt/C ink near the tip where the oxygen concentration is measured. The Nafion bridge between the ink and the sensor's tip fulfills several functions. It acts as the oxygen diffusion barrier and prevents an electrical short between the sensor and PEFC cathode. It also acts as the electrolyte bridge to the PEFC cathode, allowing the sensor to use the PEFC anode as a counter electrode (to ensure this contact, we also apply an additional thin coat of Nafion to the sensor tip). The sensor is placed between the PEFC cathode's DM and CL. The sensor in this study is $575 \mu\text{m}$ wide, protrudes ca. 1 mm into the electrode's active area, and has an ionomer bridge length of $30 \mu\text{m}$. The tip of the sensor is placed such that the measurement is localized under the channel area. The estimated thickness of the compressed sensor tip is 4-5 μm . This thickness is small compared to

the ca. 10 μm roughness of a commercial DM's microporous layer,¹ yielding a minimally intrusive sensor.

In this work, we characterize the sensor's current-voltage characteristics, and we select a voltage (e.g. 0.2 V) at which the sensor is at its limiting current. However, one issue prevents us from simply detecting the limiting current and correlating it to calibration measurements taken at the PEFC's open circuit. The sensor (being on the cathode side) is subject to the fluctuations in relative humidity as the PEFC operates and produces water. Changes in relative humidity affect the diffusivity of oxygen through Nafion.² Therefore, when the PEFC generates current, two competing effects confound pre-calibrated measurements: the increased RH increases oxygen reduction reaction (ORR) current at the sensor tip due to this effect, while the diminished concentration of oxygen (which we wish to measure) reduces ORR current.

In order to separate these effects, we employ the oxygen flux interrupt method explained in Chapter 2. We interrupt the PEFC's current, and the concentration of oxygen is rapidly restored to channel levels in a matter of milliseconds, while changes in the ionomer bridge's water content occur over tens of seconds. The result: an interruption of current provides us with an instantaneous calibration point $i_{interrupt}$ that represents the sensor's current at $c_{O_2}(\text{channel})$, but under the hydration conditions it is actually experiencing. Herein, the $c_{O_2}(\text{channel})$ is constant due to a very high stoichiometric ratio and a short air residence time in the channels.

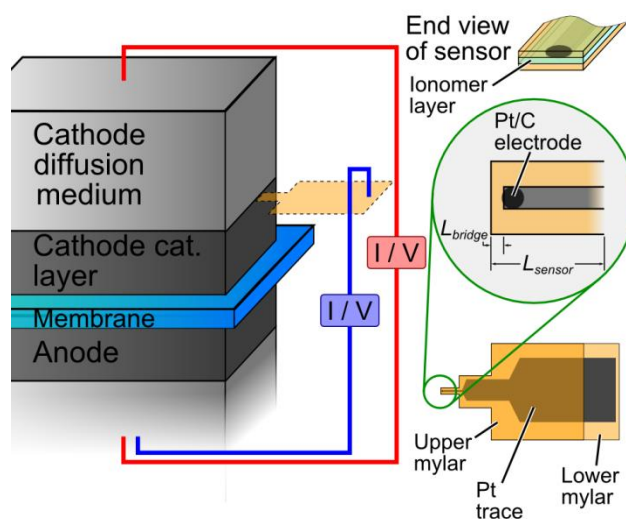


Figure 3.1 Thin-film sensor used for O₂ flux interrupt, with detail on the sensing tip.

In this case, the approach of oxygen flux interrupt is subject to one more complication: the sensor, using the PEFC anode as both a counter- and reference-electrode, is also subject to the Ohmic drops through the PEFC membrane-electrode assembly that arise from the PEFC's current. In other words, as the PEFC operates at current, yielding an Ohmic voltage loss ΔV_{Ω} , the sensor's potential is shifted by the same ΔV_{Ω} . This issue can be solved either by ensuring that the PEFC's ΔV_{Ω} is smaller than the voltage range of the sensor's limiting current plateau, or by incorporating a separate reference electrode for the sensor. In this work, we take the former approach of using the sensor within prescribed limits for ΔV_{Ω} .

3.3 Zero-Dimensional Sensor Model

Due to the Ohmic drop issue explained above, the sensor's limiting current plateau (before the hydrogen evolution reaction sets in at very low potentials) should be wider than the cell's ΔV_{Ω} . This can be achieved by decreasing the limiting current, decreasing the Ohmic resistance, or both. Increasing the length of the ionomer bridge will increase the sensor's Ohmic resistance, but also decrease i_{lim} . It is not immediately obvious whether a longer or a shorter bridge is desirable without knowing which effect is more significant. We have developed a 0-D

model of the sensor to study the effects of the ionomer bridge's geometry, as well as the effect of the activity of its active material.

The model calculates the sensor's limiting current based on the sensor geometry, the diffusivity of oxygen through the ionomer, and the concentration outside of the sensor to find a theoretical limiting current. Additionally using the exchange current density, thermodynamics, ionomer conductivity, and the Tafel equation, the model computes an entire polarization curve for the sensor. In this way, both the limiting current and the voltage range of the limiting current plateau are estimated. Using these figures of merit and fabrication constraints, this model can help to optimize the sensor. Figure 3.2 shows the results of a parametric study of the ionomer bridge length and its effect on both aforementioned figures of merit. Note that the actual values of the results will change based on other sensor parameters. Nonetheless, the trends in Figure 3.2 indicate that a longer bridge is advantageous in that the O₂ transport effect outweighs that of the Ohmic resistance. However, an excessively long bridge would yield long diffusion time scales and deteriorate the rapid O₂ accumulation that facilitates the oxygen interrupt method.

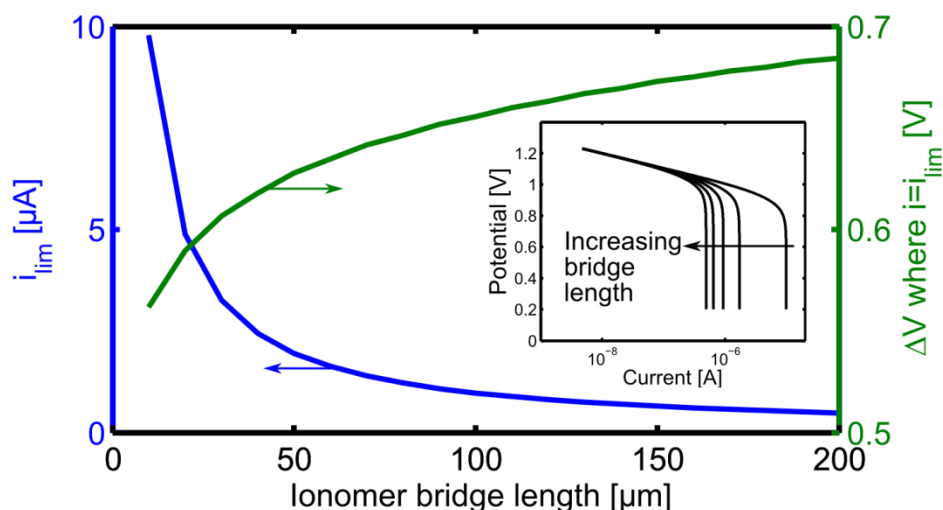


Figure 3.2: Results of a parametric study of ionomer bridge length using the 0-D sensor model.

Another aspect of the sensor prevents us from using a very long ionomer bridge. The conductive metal leading to the Pt/C tip is platinum, which has ORR activity. To ensure that the

sensor's ORR current comes primarily from its tip and not its sides, we want the incidental ionomer bridges to the sensor's sides to be significantly longer than that to the tip. If we use a tip that is too long, but still keep the side bridges comparatively longer, the sensor will have to be very wide and will begin to block too much of the cell's active area. Therefore, in this iteration, we use a shorter ionomer bridge of 30 μm . In future iterations, a less ORR-active conductive trace (e.g. gold) will be used to connect to the Pt/C catalyst at the tip, allowing different sensor geometries, since the ORR current will be forcibly localized to the more active tip.

3.4 Experimental

We fabricated the sensor using 1.5 μm PET film (Goodfellow, Huntingdon, England), Nafion DE-521 suspension (Ion Power, New Castle, DE), and Pt/C catalyst (20% Pt/C on Vulcan XC-72R, HiSPEC 3000, Alfa-Aesar, Ward Hill, MA). We placed the sensor between the cathode of a 1 cm^2 commercial membrane-electrode assembly (Ion Power) and a 10BB Sigracet® DM (Ion Power) such that the sensor penetrated 1 mm into the cell's active area and its tip was under the channel area. The PEFC and sensor were operated with a Bio-Logic VSP potentiostat (Bio-Logic, Claix, FR), and the gas flow and temperatures were controlled by a Scribner 850e test stand (Scribner Associates, Southern Pines, NC). In all cases, the relative humidity was 87%, the cell temperature was 60°C, and the cathode and anode gas flow rates were 400 sccm.

3.5 Results and Discussion

3.5.1 Sensor Characterization

In order to employ the oxygen flux interrupt method as described, we first characterized the sensor's current-voltage characteristics to identify the voltage range for limiting sensor current. We performed this test with the PEFC at open circuit, so that no oxygen was being consumed by the cell, and so the oxygen concentration throughout the cathode was at that of the channel gas (the current drawn by the sensor is low enough that it does not consume substantial oxygen). We generated a sensor I/V curve by holding the sensor at constant voltages ranging from its open circuit down to 0.05 V for 5 minutes each, averaging the last 50% of each hold. The results of this are shown in Figure 3.3 for two cases – one with air (21% oxygen), and the other with 10% oxygen (achieved by diluting the air with nitrogen).

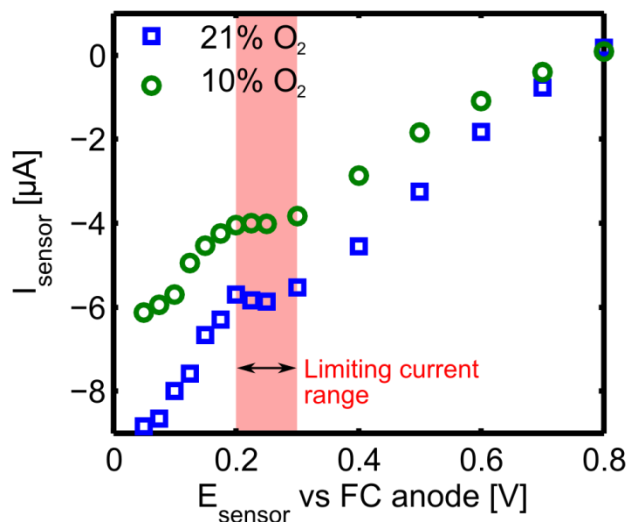


Figure 3.3: Sensor I/V curves for 21% and 10% oxygen, both with the PEFC at open circuit, 87% RH, and 60°C.

As Figure 3.3 shows, the limiting current range roughly extends from 0.2 to 0.3 V for this particular sensor. Therefore, a sensor voltage of 0.2 V versus the PEFC anode is ideal, since the Ohmic drop in the cell running at non-zero current will shift the sensor's apparent voltage upward, towards 0.3 V, along the plateau. Using electrochemical impedance spectroscopy, we measured the high-frequency resistance of the membrane-electrode assembly to be $60 \text{ m}\Omega \text{ cm}^2$. This means that when the cell operates at current densities above 1.6 A/cm^2 , the cell's Ohmic drop will be close to or above 100 mV, causing a shift in the sensor's effective voltage operating point that possibly moves it out of the limiting current range. Therefore, we have reduced confidence in the c_{O_2} measurements taken when the PEFC was operating above 1.6 A/cm^2 .

Prior to taking O_2 flux interrupt measurements, we determined the sensor's current at the set voltage in nitrogen (i_{N_2}), and additionally verified that this value is stable and does not change with varying RH. We also observed that the sensor's current at the set voltage in air is in fact a strong function of RH even when the PEFC is at open circuit.

3.5.2 Oxygen Flux Interrupt Measurements during PEFC Operation

We collected a polarization curve potentiostatically, with holds every 20 mV from open circuit to $E_{\text{cell}} = 0.8 \text{ V}$, and every 100 mV thereafter for 11 minutes, down to 0.1 V. For E_{cell}

holds of 0.7 V and below, we performed the oxygen flux interruption with a 2 second current interruption by stepping the cell voltage to $E_{cell} = 0.9$ V (where the oxygen consumption was negligible) every minute. Eleven measurements were made at each cell voltage. Over the whole duration, the sensor was held at 0.2 V and its current was recorded.

The polarization curves and oxygen concentrations were measured with humidified (87% RH) gases, once with 21% and again with 10% oxygen. The time-series of sensor current was analyzed to obtain the dimensionless oxygen concentrations, $\overline{c_{O_2}}$, relative to that of oxygen in air. For the polarization curve plots, each PEFC current data point is the average of the time average currents measured during the last 50% of each 1-minute segment between the current interruptions. Figure 3.4 presents the results for $\overline{c_{O_2}}$ alongside the associated polarization curves for the PEFC. Here, both dimensionless oxygen concentration plots are normalized to the 21% O₂ level so the two sets of results can be compared in terms of concentration. That is, the 10% oxygen results for $\overline{c_{O_2}}$ were multiplied by the fraction 10/21 so that the values are normalized by 21% oxygen instead of 10%. This means that in the 10% O₂ case, the maximum possible value of $\overline{c_{O_2}}$ is 0.5.

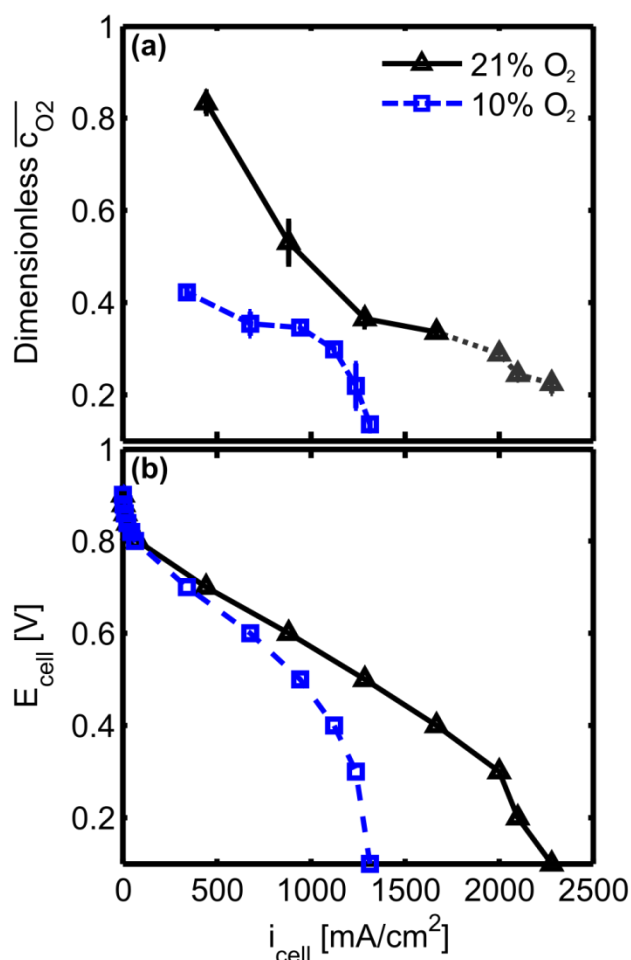


Figure 3.4: (a) Dimensionless oxygen concentration measurements in 21% and 10% oxygen. Error bars represent \pm one standard deviation based on 11 measurements. The data points in the 21% O_2 case marked with a dotted line are questionable due to the PEFC Ohmic drop, but are included for completeness. (b) PEFC polarization curves from the same experiment as the concentration measurements in (a). In both plots, connecting lines are to guide the eye. PEFC was at 60°C and 87% RH.

A particularly interesting scenario to study with this method is when the PEFC is at its limiting current. Since the PEFC's limiting current density was greater than $1.6 \text{ A}/\text{cm}^2$ under 21% O_2 , we are less confident in those last values of $\overline{c}_{\text{O}_2}$ (dotted line) in that case. We turn to the 10% O_2 case, where the PEFC's limiting current was below $1.5 \text{ A}/\text{cm}^2$. Our first remark is that the value of $\overline{c}_{\text{O}_2}$ is nearly zero, suggesting that most of the oxygen transport loss is in the DM in this case.

Second, we note that the trend of $\overline{c_{O_2}}$ vs PEFC current is mostly linear in the 21% and 10% O₂ cases at low current. However, in the last two points of the 10% O₂ case – as we approach the cell’s limiting current – we see a sharp down-turn of $\overline{c_{O_2}}$, away from the linear trend. To explain a change in the $\overline{c_{O_2}}$ curve’s slope, we suggest two possible, distinct events: 1) a change in the DM’s effective diffusivity, or 2) a change in the location of the reaction – concentrated under the land or channel (recall, the sensor is under the channel). At roughly constant cell temperature, the effective diffusivity should only change with changing liquid water accumulation in the DM – more water results in a steeper slope. We expect the spatial current density cell changes only a small amount because of the high air stoichiometric ratio used. Thus, the 10% O₂ results suggest flooding of the DM occurred in this experiment at current densities greater than 1000 mA/cm².

In the 21% O₂ case, we see an opposite trend, where the slope became less steep at high current. Those last points are slightly dubious given the high current density. Nevertheless, if the effective sensor voltage were to rise above the limiting current range due to the membrane’s Ohmic drop, it would cause lower sensor and hence spuriously low concentration estimations (not higher concentration). In other words, the Ohmic drop issue would cause c_{O_2} readings to be lower than reality, but in Figure 3.4 the noteworthy trend is one that deviates to higher values. Therefore, while the values themselves are questionable, we do have confidence in the positive curvature trend of the 21% O₂ case. This decreasing slope indicates a higher effective diffusivity at high currents. It is common in PEFC studies to observe flooding at intermediate current (due to water production) followed by dry-out at higher current densities (due to greater heat production raising the temperature and evaporating water). This is consistent with the changing slope that indicates less flooding at higher currents.

To give further insight into the results, we calculated values for the oxygen transport resistance R_{O_2} through the DM, using the concentration results and PEFC current densities in Figure 3.4. As we have discussed previously, R_{O_2} arises from an electrical resistor analogy of Fick’s law of diffusion. This analogy is similar to Darcy’s law, only for diffusive gas flux instead of viscous flow. Given the previously described assumption that the concentration of oxygen in

the channel c_{ch} is that of the inlet gas (either 0.21 or 0.1 atm for full and half air cases, respectively), and knowing the oxygen flux \dot{n}_{O_2} from the PEFC current density and Faraday's law of electrolysis, R_{O_2} is given by:

$$R_{O_2} = \frac{c_{ch} - c_{meas}}{\dot{n}_{O_2}} \quad (3.1)$$

The results of this calculation are shown in Figure 3.5. The fact that the half-air values are less than the full-air values suggests that there is significantly less liquid water in the DM in the half air case for the same given current density. This is likely due to a higher temperature – the lower O_2 concentration causes a higher overpotential (evident in the lower cell voltage), which implies a greater rate of heat production in the cell in the half air case. The resulting higher temperatures allow more liquid water to exist in the vapor phase rather than as oxygen-blocking liquid. To further support this idea, we note that the values of R_{O_2} for the half-air case agree well with the measurement in Chapter 2, where we found that R_{O_2} was 65 s/m for a dry 10BC DM (a newer but very similar version of the 10BB in the present work). Similarly, the notion that the full-air case was significantly flooded at all currents (inferred from its higher R_{O_2} values) would agree with Chapter 2's findings of liquid water in the DM at 83% and 91% RH, compared to this study's 87% RH. Finally, we discussed earlier in this section that the 10% O_2 case shows increasing liquid water flooding at its very highest currents, and the 21% O_2 case appears to flood at intermediate currents but dry out somewhat at the highest currents. Those notions are supported by the results in Figure 3.5, if R_{O_2} is taken as a proxy for the extent of liquid water flooding in the DM.

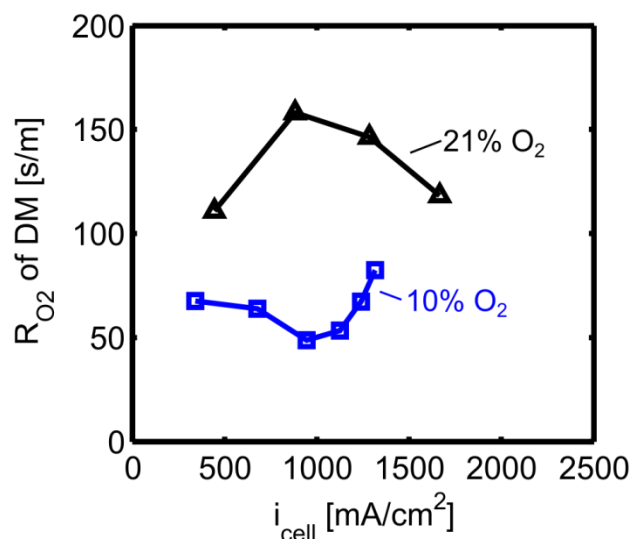


Figure 3.5 Oxygen transport resistance of the entire DM calculated from values of c_{O_2} measured in this study, plotted as a function of PEFC current density for full and half air cases.

3.6 Summary

In this chapter, we presented a thin-film sensor capable of measuring the oxygen concentration at the interface between the cathode and the DM of a PEFC. To take accurate measurements with this sensor, we employed the oxygen flux interrupt method that provides instantaneous calibration points for each measurement. Our measurements showed c_{O_2} at the DM/electrode interface to have a non-linear dependence on current density, which we suggest is due to changing amounts of liquid water in the DM. Similarly, our calculation of the overall oxygen transport resistance through the DM agrees with those of Chapter 2, if the half-air case in this chapter is taken to be single-phase and the full-air case in this work is assumed to be flooded. This work complements that of Chapter 2 in that this work can measure R_{O_2} of the entire DM, whether the DM is flooded or not. In contrast, the method of Chapter 2 is limited to the single-phase case for actual R_{O_2} measurements, but can map out both R_{O_2} and liquid water flooding as a function of space in the DM.

3.7 References for Chapter 3

1. F. E. Hizir, S. O. Ural, E. C. Kumbur and M. M. Mench, *J. Power Sources*, **195**, 3463 (2010).

2. Y. Takamura, E. Nakashima, H. Yamada, A. Tasaka and M. Inaba, *ECS Trans.*, **16**, 881 (2008).

4 In-Situ Oxygen Concentration Measurement Through the Thickness of a Cathode Catalyst Layer

4.1 Introduction

In this chapter, we present a micro-electrode scaffold (MES) for *in-situ* sensing of species concentration distributions through the thickness of polymer electrolyte fuel cell (PEFC) catalyst layers (CLs). To the best of our knowledge, this is the first method for making such measurements. As Figure 4.1 shows, the MES allows platinum ultra-microelectrodes (UMEs) to intercept the side of a roughly one-dimensional catalyst layer column at several points across its thickness. A thin electrolyte layer is coated around the circumference of the catalyst layer to electrically isolate it from the UMEs. Electroanalytical techniques such as cyclic voltammetry (CV), linear sweep voltammetry (LSV), chronoamperometry, and pulsed amperometric detection (PAD) can then be used to yield species concentration data. Here we present measurements of the oxygen concentration c_{O_2} at multiple points through the thickness of a cathode catalyst layer using potentiostatic chronoamperometry and PAD.

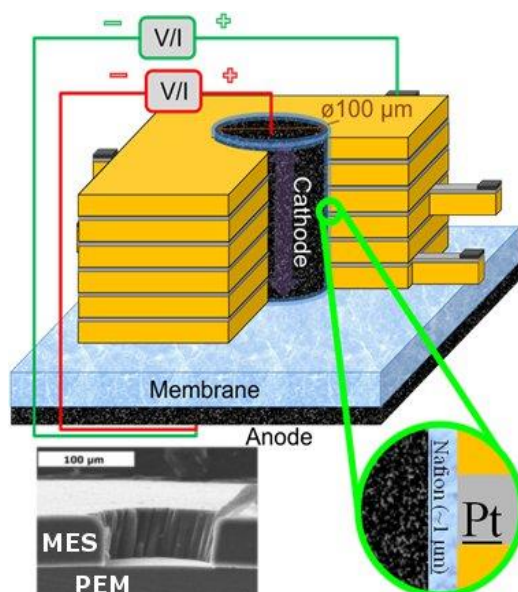


Figure 4.1 Schematic of O₂-sensing MES, with detail on Nafion coating of inner side-wall. Inset: SEM image of MES before filling with CL ink.

4.2 Experimental

4.2.1 MES Fabrication

The MES illustrated in Figure 4.1 is composed of alternating insulating and sensing layers that surround a working fuel cell cathode. The insulating layers for this MES were 7.5 μm thick Kapton film (American Durafilm, Holliston, MA, USA) with 1 μm of Teflon FEP solution (TE9568, Fuel Cell Earth LLC, Stoneham, MA, USA) spin-coated on to aid hot-bonding the layers together. RF-magnetron sputtering was used to deposit a 200 nm Pt film (the sensing layer) on the other side of the Kapton. The Pt-Kapton-FEP substrate was subsequently cut into a shape that allows an exposed surface of Pt coated Kapton to protrude from the side of the MES and connect to an electrical contact. Five such layers were stacked and hot-bonded for 10 minutes at 300°C and 3.6 MPa, and allowed to cool under pressure overnight (cooling under pressure was critical to good layer bonding). A 100 μm diameter hole was cut into the center of the stack with a laser micro-mill (New Wave, Fremont, CA, USA), and the inside wall of the hole was coated with approximately 2 μm of Nafion, using 5 wt% DE-521 Nafion solution (Ion Power, New Castle, DE, USA), to provide electrolytic contact and prevent electrical shorting between the UMEs and the catalyst layer. The hole was then filled with catalyst layer ink, which

was made using Pt/C catalyst (20% Pt/C on Vulcan XC-72R, Fuel Cell Store, San Diego, CA, USA) and Nafion DE-521 (Ion Power) for 30% wt. Nafion content. The ink was mixed overnight using a magnetic stirrer and then hand painted into the 100 μm diameter hole to create a 50 μm thick circular cathode inside the MES. The MES was hot-bonded to a Nafion 115 membrane (Ion Power) for 4 minutes at 125°C and 0.7 MPa. At each fabrication step, the resistance between the Pt layers was measured to ensure sufficient electrical isolation. A sourcemeter (2410 1100V Sourcemeter, Keithley Instruments, Cleveland, OH, USA) was used in two-wire resistance measurement mode to verify that the resistance between layers was on the order of tens of megaohms.

4.2.2 Experimental Setup

The MES-membrane assembly was stacked between a gas diffusion electrode (GDE) (Electrochem EC-20-10-7 Electrode, Woburn, MA, USA) used for the anode and a diffusion medium (DM) (SGL-24BC, Ion Power) for the cathode, and placed inside custom fuel cell hardware designed to provide isolated electrical connections to the protruding UME Pt film. Cathode air and anode hydrogen flow were controlled and humidified by a fuel cell test stand (850e test stand, Scribner and Associates, Southern Pines, NC, USA). Where noted, additional dry nitrogen gas was used to dilute the oxygen in the humidified air for UME verification and calibration. The flow rate of the nitrogen was controlled with a manual flow control valve and rotameter (Key Instruments, Trevese, PA, USA). A potentiostat (SP-150, Bio-logic, Knoxville, TN, USA) was used to control the fuel cell potential and current, and the aforementioned Keithley sourcemeter was connected to the UME leads for c_{O_2} sensing. The Keithley sourcemeter was controlled by custom LabVIEW code for chronoamperometry and PAD. The fuel cell anode was used as the reference- and counter-electrode for the UME measurements, where the UMEs were used as the working electrodes. The experiments were performed with the fuel cell placed inside a Faraday cage (Technical Manufacturing Corporation, Peabody, MA, USA) to minimize noise.

Except where otherwise noted, the cathode air flow rate was 0.4 slpm and its dew point was 30°C; the anode's hydrogen had the same flow rate and a dew point of 40°C. The cell temperature was set to 44°C. Both gases were at atmospheric pressure. The high flow rates and

dry conditions were chosen for this initial study to ameliorate flooding and extract data regarding single-phase gas transport limitations.

4.3 Results and Discussion

4.3.1 Fuel Cell and UME Characterization.

Figure 4.2a shows the fuel cell polarization curves obtained by CV at 10 mV/s. The polarization curves exhibit the hysteresis and Ohmic behavior expected for the low humidity conditions used. In addition, the catalyst layer used in this study presented significant activation losses as indicated by the large voltage drop at low currents. It is also important to note that the fuel cell polarization curve does not exhibit mass transport limitations despite the high thickness of the electrode. This result is in part due to the low humidity operation.

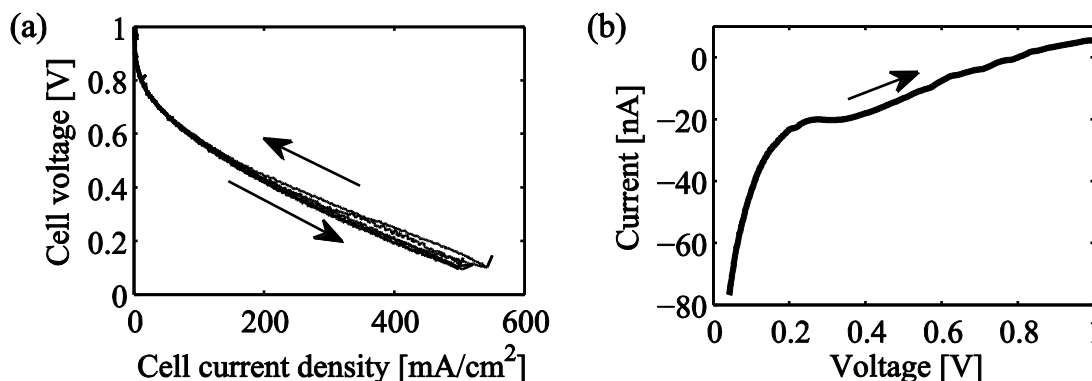


Figure 4.2: (a) CV of the fuel cell at a scan rate of 10 mV/s, with cathode and anode inlet gas respectively at 30°C and 40°C, both flowing at 0.4 slpm at atmospheric pressure, and a cell temperature of 43°C. (b) Reverse scan from CV of a Pt UME located 42.3 μm from the membrane (scan rate 5 mV/s). A transport-limited ORR region can be seen in the vicinity of 0.2 V.

In order to determine the voltage at which oxygen reduction at the UME was diffusion-limited, and to verify the expected UME behavior, CV was performed on the UMEs at 5 mV/s. Figure 4.2b shows the reverse scan from a CV study on the UME located 42 μm from the membrane. The CV shows a flat region indicating limiting ORR current around 0.2 V. At lower potentials, the current increases again. This is most likely from the hydrogen evolution reaction, which exists in every PEFC electrode at sufficiently low voltage as well, but it is usually dominated by oxygen reduction current. In this case, the low oxygen reduction current on the

UME allowed the low hydrogen evolution current to be more evident. Similar hydrogen evolution current behavior has been seen in other PEFC electrodes past their limiting current in cases where the overall signal is low.¹ To remain within the limiting current plateau of Figure 4.2, in this study, a UME potential of 0.175 V was chosen as sufficient for performing oxygen reduction in an oxygen transport limited regime.

4.3.2 Concentration Measurement with Potentiostatic Chronoamperometry

Potentiostatic measurements were performed by holding a UME's voltage at the previously noted potential of 0.175 V and recording the current. This proved a useful method for collecting anecdotal data to show the response of the UMEs to changes in c_{O_2} . While holding this potential on the UME located 7.5 μm from the membrane, the flow rate of nitrogen was varied using the control valve rotameter. The nitrogen was mixed with air at 0.1 slpm to produce gas mixtures with different oxygen mole fractions, and hence different values of c_{O_2} . The UME current showed to be sufficiently sensitive to changes in c_{O_2} with a quick (< 1 s) response, as seen in the time series in Figure 4.3. The case of near zero c_{O_2} (where the air flow rate was set to zero) gives a positive UME current. This likely corresponds to a hydrogen oxidation reaction that underlies all UME data, as seen in similar works.²

Also using potentiostatic UME c_{O_2} sensing, the fuel cell voltage was changed from open circuit to 0.2 V in a single step. As Figure 4.4 shows, the increased cell current caused a rapid drop in ORR current at the UME. The drop in c_{O_2} was large enough that the UME current became positive, indicating hydrogen oxidation due to crossover. As this was the UME located closest to the membrane, it is expected that hydrogen was present and the oxygen was almost completely depleted at high cell currents, especially considering the thickness of the catalyst layer. It is also important to note from Figure 4.4 that the UME current is almost three orders of magnitude smaller than that of the fuel cell, which demonstrates that the oxygen consumption by the UME should have negligible influence on the amount of oxygen available in the cathode CL.

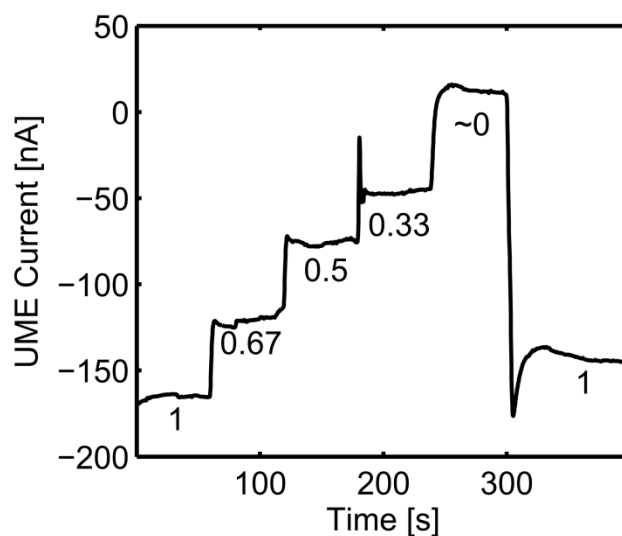


Figure 4.3: Time series of current for the UME located $7.5 \mu\text{m}$ from the membrane as c_{O_2} - listed on figure as a fraction of $c_{O_2(\text{air})}$ - was varied every 60 s.

During the course of the previously described potentiostatic chronoamperometry measurements of c_{O_2} , we observed significant and long transients (many minutes) characteristic of electrode fouling. These transients not only made measurement times prohibitively long, but also rendered the measurements less repeatable, as can be seen by comparing the two different steps in Figure 4.3 where the dimensionless $c_{O_2} = 1$ (i.e. that of oxygen in air). Furthermore, the electrode fouling reduced the current measured by the UMEs and thus reduced measurement resolution. Therefore, for greater repeatability and resolution, PAD was used in the proceeding measurements of c_{O_2} distributions in the catalyst layer. In the future, the oxygen flux interrupt method described in Chapter 2 could be a promising method for making these measurements as well.

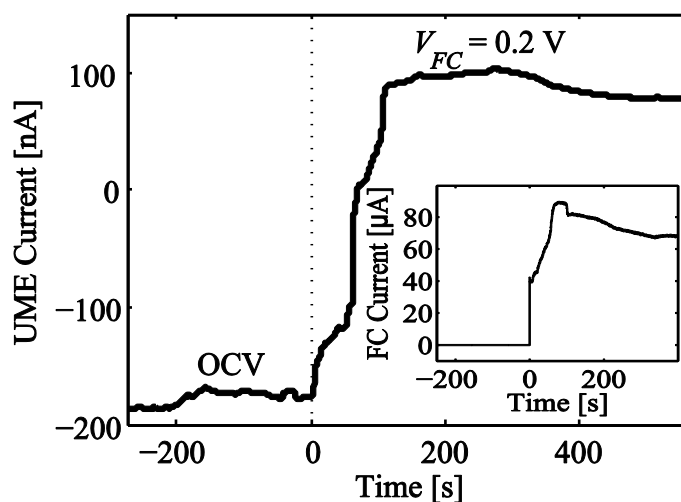


Figure 4.4: UME current time series for a fuel cell voltage change from OCV to 0.2 V for the UME located 7.5 μm from the membrane. The change in current indicates the near complete depletion of oxygen. The inset shows the corresponding fuel cell current time series.

4.3.3 Concentration Distribution Measurement with PAD

The O_2 concentration distribution across the catalyst layer was measured using PAD with a waveform featuring three potential pulses: the first pulse anodically cleaned the electrode; the second pulse cathodically renewed it by stripping oxides; and the third pulse, after a short spike from capacitive discharge, measured the ORR current.^{3, 4} In this experiment, the anodic and cathodic pulses were 1 s each at 1.5 V and -0.2 V, respectively. The measurement pulse was 8 s at 0.175 V, where the current recorded was the average of the last 2 s.

To ensure the different UMEs were providing independent local measurements during c_{O_2} distribution analysis, the PAD technique was applied separately and then simultaneously to adjacent pairs of UMEs while the fuel cell was held at open circuit. We verified that the sum of the currents measured for each UME was approximately equal to the current measured when PAD was applied to adjacent pairs simultaneously.

During the c_{O_2} distribution measurement, the fuel cell was held at a galvanostatic operating point of 450 mA/cm^2 . The galvanostatic hold was preferred over a potentiostatic hold for measuring the c_{O_2} at each layer individually in series, as the fuel cell's constant oxygen consumption rate with galvanostatic operation allowed more repeatable measurements over the

25 minutes it took to complete PAD measurements on all five layers in series. In the future, one would ideally measure the c_{O_2} distribution either simultaneously at all UMEs, or with faster switching times between UMEs. In the experimental results shown here, we performed 30 PAD sequences for each data point, with the mean and standard deviation of the last 23 measurements being used for data processing. For each measurement of c_{O_2} , the PAD measurement for each UME first had to be calibrated for the relationship between c_{O_2} and the measured PAD current. A two-point, linear calibration was made by first running the cell at open circuit (c_{O_2} of the channel air, defined as 1 in this dimensionless scheme) and measuring the PAD current, and then measuring the PAD current with the cathode flooded with nitrogen (zero c_{O_2}). Only two calibration points were taken because the ORR current generally has a linear relationship with c_{O_2} as evidenced by Figure 4.3 and the work by Takaichi et al.² After measuring the two calibration points, the cathode gas was switched back to air and the cell held at the desired current, and another 30-trial PAD sequence was performed to obtain the operating point measurement. The two calibration points and the operating point measurement were used to determine the dimensionless value c_{O_2} with the following formula:

$$c_{O_2} = \frac{I - I_0}{I_{OCV} - I_0} \quad (4.1)$$

where I is the PAD measurement current while the cell is at the operating point, and I_0 and I_{OCV} are the PAD measurement currents from the calibration measurements in N_2 and air, respectively. As all three current measurements were based on many realizations and had associated variance, error propagation theory was used with Equation (4.1) to combine all three measurements' standard deviation values (σ) into one value:

$$\sigma_{c_{O_2}} = \sigma_I \left| \frac{\partial c_{O_2}}{\partial I} \right| + \sigma_{I_0} \left| \frac{\partial c_{O_2}}{\partial I_0} \right| + \sigma_{I_{OCV}} \left| \frac{\partial c_{O_2}}{\partial I_{OCV}} \right| \quad (4.2)$$

One at a time, each layer was used to measure c_{O_2} as the fuel cell held 450 mA/cm^2 . Figure 4.5 shows the resulting through-plane distribution of oxygen concentration, and an analytical fit from Fick's law that assumes a spatially uniform volumetric reaction rate $\dot{n}_{O_2,vol}$:

$$D_{eff,CL} \left(\frac{d^2 c_{O_2}}{dz^2} \right) = \dot{n}_{O_2,vol} = \frac{i_{cell}}{4FL_{CL}} \quad (4.3)$$

where L_{CL} is the CL thickness of $50 \text{ }\mu\text{m}$, F is Faraday's constant, and z is the coordinate through the thickness of the CL ($z = 0$ is the CL|membrane interface). The fitting parameters of this curve are a useful output. They are the concentration at the CL|DM interface $c_{O_2}(CL|DM) = 0.75$, and the pore-phase CL diffusivity $D_{eff,CL} = 1.3 \cdot 10^{-7} \text{ m}^2 / \text{s}$. The fit itself had an R^2 value of 0.323. Due to the low value of the goodness of fit merit R^2 , the values of the fitting parameters should be taken lightly.

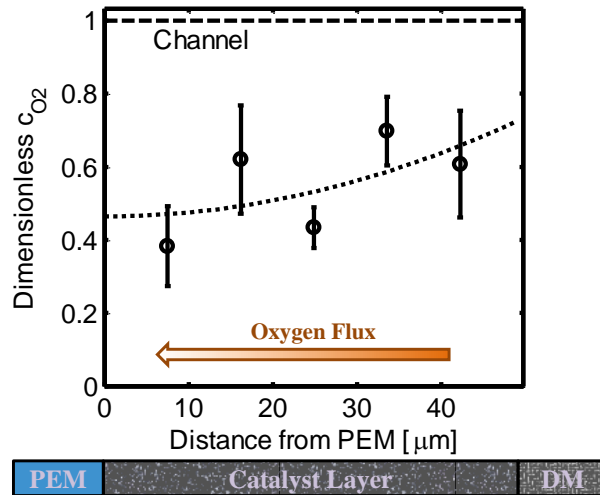


Figure 4.5: *In-situ* distribution of c_{O_2} through the thickness of a fuel cell cathode operating at 450 mA/cm^2 . A schematic key to the x-axis is shown below. A fit based on Fick's law with constant reaction rate is shown by a dotted line. The error bars represent the propagation of one standard deviation from the two calibration and one operating point measurements, with each of the three standard deviations being for 23 realizations. The dashed line indicates the c_{O_2} in the channel, defined as 1.

The c_{O_2} profile shows a general decline in oxygen concentration deeper in the CL, as we would expect, but the data do not form a solid trend. This is likely because the fuel cell under study was not completely stable, and measurements were taken at each layer separately, in

sequence. The measurements at each layer lasted 5 minutes, allowing sufficient time for the system itself to change. In the future, either simultaneous or quickly-switched data collection will be able to overcome this issue.

From the analytical fit, the dimensionless concentration of 0.75 at the CL|DM interface is in the same range as the results from Chapters 2 and 3, but is slightly higher, as expected – the 24BC DM in this study is thinner by nearly a factor of 2 compared to the 10BB and 10BC DMs used in Chapters 2 and 3. The value of $D_{eff,CL} = 1.3 \cdot 10^{-7} m^2 / s$, when compared with the binary diffusivity of O₂ in N₂ at this temperature $D_{O_2/N_2} = 2.3 \cdot 10^{-5} m^2 / s$, gives a formation factor $K_{form} = 0.006$ (the formation factor is defined and discussed in Chapter 2). This is significantly less than the single-phase K_{form} estimate of 0.15 from the microstructural analysis of a CL in Litster et al.,⁵ and on the lower end of CL diffusivities measured experimentally by Yu and Carter.⁶ The latter work studied $D_{eff,CL}$ in CLs made with varying ionomer/carbon (I/C) weight ratios of 0.5, 1, and 1.5, for which they found K_{form} values of 0.09, 0.03, and 0.004, respectively. Only that work's unusually high I/C ratio of 1.5 yielded a K_{form} measurement similar to this MES work. However, the CL composition in this MES has an I/C weight ratio of 0.5, for which Yu and Carter⁶ measured a much higher diffusivity, with a K_{form} of 0.09, more in agreement with Litster et al.'s⁵ K_{form} value of 0.15 from a similar CL composition. One explanation for this discrepancy could be that the CL pores in this work were flooded with liquid water. We can estimate the pores' saturation with liquid water S using the ratio of K_{form} to its expected value:

$$S = 1 - \frac{K_{form,meas}}{K_{form,expected}} \quad (4.4)$$

Using the literature $K_{form,expected}$ values for comparable electrode compositions (0.15 and 0.09)^{5, 6} yields estimated saturations S of 96% and 93%, respectively. These high saturation values are surprising given the 46% RH of the cathode gas in this MES study, and the lack of any significant mass transport voltage losses in the polarization curves (Figure 4.2). If the saturation is high, one possible explanation is that the geometry of the MES creates a high-humidity environment – the anode was more humid, meaning the Nafion membrane had a higher water activity than the cathode gas, and the cathode CL of the MES draws from a disproportionately

large area of Nafion membrane,⁷ which could lend the cathode CL a higher activity of water. It is also possible that the boundary on the sides of the CL created by the MES impedes water outflow. Finally, a third possibility is that the fitting parameters are simply not entirely representative, given the low R^2 value of 0.323 for the fitted curve.

4.4 Summary

A novel apparatus for making *in-situ* measurements of c_{O_2} distribution through the thickness of a PEFC cathode was presented in this paper. To our knowledge, it is the first such measurement. The sensitivity of the UMEs was first investigated using potentiostatic chronoamperometry, verifying that c_{O_2} was successfully being measured. To improve repeatability, PAD was adopted as the primary measurement technique. After two calibration measurements for each layer, the fuel cell was galvanostatically held at 450 mA/cm^2 while operating point c_{O_2} measurements were taken at the UMEs. The results were compiled into a c_{O_2} distribution, which showed a decrease of c_{O_2} through the thickness of the catalyst layer. Using an analytical fit from Fick's law (assuming a constant reaction rate), we extract an estimated CL/DM concentration $\overline{c_{O_2}}(CL|DM) = 0.75$, which compares reasonably with the results of Chapters 2, and we extract an estimated pore-phase CL diffusivity $D_{eff,CL} = 1.3 \cdot 10^{-7} \text{ m}^2 / \text{s}$. This may indicate a high liquid water saturation in the CL pores, when compared with the expected single-phase $D_{eff,CL}$ found in other studies.

4.5 References for Chapter 4

1. T. a. Greszler, D. Caulk and P. Sinha, *J. Electrochem. Soc.*, **159**, F831 (2012).
2. S. Takaichi, H. Uchida and M. Watanabe, *Electrochim. Acta*, **53**, 4699 (2008).
3. W. R. LaCourse and S. J. Modi, *Electroanalysis*, **17**, 1141 (2005).
4. A. J. Bard and L. R. Faulkner, *Electrochemical Methods: Fundamentals and Applications*, John Wiley & Sons, Hoboken (2001).
5. S. Litster, W. K. Epting, E. A. Wargo, S. R. Kalidindi and E. C. Kumbur, *Fuel Cells*, **13**, 935 (2013).
6. Z. Yu and R. N. Carter, *J. Power Sources*, **195**, 1079 (2010).

7. K. C. Hess, W. K. Epting and S. Litster, *Anal. Chem.*, **83**, 9492 (2011).

5 Resolving the 3D Catalyst Layer Microstructure Using Nanoscale X-ray Computed Tomography

5.1 Introduction

In this chapter, we employ x-ray computed tomography (XCT) to characterize the microstructure of a polymer electrolyte fuel cell (PEFC) cathode catalyst layer (CL). XCT offers the capability to non-destructively resolve the 3D structure of porous materials with high spatial resolution¹⁻⁶ using X-ray radiographs from many angles to computationally reconstruct a 3D image of the material.⁷ Empty pores absorb less radiation and hence contrast with solid materials. Owing to recent developments using specialized X-ray lenses, 50 nm resolution is now available in commercial XCT equipment using Zernike phase contrast and a Fresnel zone plate objective (nano-CT).² Phase contrast is important for obtaining reasonable signal-to-noise ratios (SNR) when imaging nano-scale features.

In medicine and biology, nano-CT techniques have recently been used for imaging variations in bone density at approximately 100 nm resolution⁸ and visualizing metal nanoparticles in cells at 40 nm resolution.⁹ In the field of electrochemistry, nano-CT has been used to investigate the morphology of solid oxide fuel cell electrodes,²⁻⁴ where the constituent materials have high atomic numbers (Z) and high X-ray contrast. Their morphology is also very different from PEFC electrodes. In a PEFC electrode, most of the solid volume is comprised of low Z materials (carbon and a fluorocarbon ionomer), although it also contains small (3-5 nm), dispersed Pt nanoparticles that occupy roughly 1% of the electrode volume. Post-mortem nano-CT has been used to two-dimensionally image macroscopic Pt redistribution in a PEFC electrode to study electrode degradation.³ However, to our knowledge, nano-CT has not previously been used to characterize the overall 3D structure of a PEFC electrode or of any carbon material with similar feature sizes.

In imaging PEFC electrodes, the nano-CT's 50 nm resolution cannot separately distinguish the individual 30-40 nm diameter carbon support particles, the 3-5 nm diameter platinum nanoparticles, and the 5-10 nm thick ionomer films within the agglomerates, since

these basic constituents are smaller than the resolution. Rather, nano-CT is able to provide a useful 3D characterization of the size and shape of those agglomerates, as well as the pores between them. Additionally, because it is non-invasive and does not require a vacuum, nano-CT holds promise for *in-situ* imaging of PEFC electrodes. Eller et al.^{5, 10, 11} have demonstrated *in-operando* micrometre scale imaging of liquid water in PEFC diffusion media using XCT, though more recent works suggest that the high-intensity synchrotron beam in that work has a serious impact on the PEFC's performance.¹¹

In this chapter, we report our use of nano-CT to image *ex-situ* the morphology of PEFC electrodes. The nano-CT data is used to extract volumetric distributions of the effective secondary pore and agglomerate diameters. The nano-CT measurements are validated by TEM imaging and by comparisons between MIP data and computational simulations of MIP using geometry from the nano-CT data.

5.2 Experimental

Two PEFC electrodes were imaged using the nano-CT system (UltraXRM-L200, Xradia Inc., Pleasanton, CA) illustrated in Figure 5.1. The electrodes were composed of carbon supported Pt catalyst (Vulcan XC-72R, 20% wt. Pt/C) and Nafion[®] ionomer binder (35% wt. loading). The ultrasonically-dispersed (10 min) catalyst ink suspension of the first electrode (Electrode 1, E1) was painted onto Kapton[®] films rather than the typical Nafion[®] membrane to eliminate time varying hydration and swelling of Nafion[®]. From TEM imagery, the thickness of E1 was approximately 70 μm for a Pt loading of 0.9 mg Pt/cm². A second electrode sample (Electrode 2, E2) with larger agglomerates was prepared following Wilson et al.'s¹² protocol that adds tetrabutylammonium hydroxide and glycerol, and underwent only 30 s of ultrasonication.

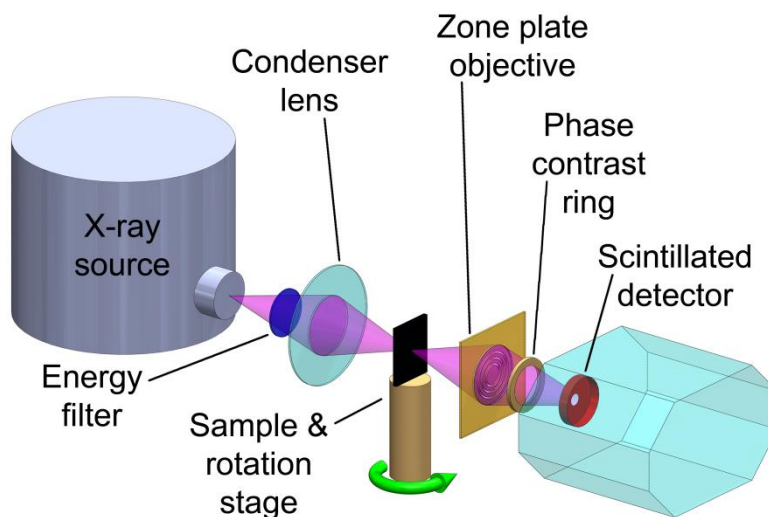


Figure 5.1 Schematic of the nano-CT instrument, which uses x-ray optics to non-destructively achieve high-resolution 3D images of both hard and soft materials. A reflective condenser optic focuses the X-rays from a laboratory X-ray source onto the sample, which rotates on a high-precision stage. The Fresnel zone plate objective is positioned past the sample. The Zernike phase ring then shifts the phase of the unscattered X-rays to enhance contrast, particularly for low-Z materials.

5.2.1 Sample preparation

To prepare E1, a catalyst suspension was prepared with 20 wt% Pt/Vulcan XC-72R (Electrochem, Woburn, MA), 5 wt% Nafion[®] DE-521 suspension (Ion Power, New Castle, DE), and de-ionized water. The Nafion was loading was 35% wt. The mixture was agitated by a dip ultrasound mixer (Cole-Parmer, Vernon Hills, IL) for 10 minutes and stirred by magnetic stir bar overnight. It was then painted onto a 3 x 4 cm piece of 50 μm thick Kapton HN film (DuPont, Wilmington, DE) to obviate the time-varying swelling that occurs with Nafion[®] substrates and hinders ex-situ imaging. Xie et al.¹³ demonstrated that painting electrodes onto Kapton has no discernable impact on the electrode structure because of Kapton's good wettability to catalyst suspensions. Repeated painting continued, with 30 minutes in a 110°C oven between coats, until the gravimetrically determined platinum loading reached 0.9 mg cm^{-2} . From TEM images, the thickness of E1 is approximately 70 μm for this Pt loading. This high loading is 2-3 times more than typical loadings and was chosen to increase the electrode volume for more accurate MIP.

The second electrode, E2, was prepared having the same volumetric composition of Pt, carbon, and Nafion as E1, but in such a way as to feature a larger pore and agglomerate diameter.

This catalyst ink suspension was ion-exchanged with tetrabutylammonium hydroxide following Wilson et al.'s¹² method and featured glycerol as an additional solvent, and a shorter duration of ultrasonication (ca. 30 s).

5.2.2 Porosimetry and electron microscopy

A 3 x 3 cm section of the finished E1 electrode with Kapton backing was characterized by MIP to obtain pore size distributions. The MIP was performed by Porous Materials, Inc. (Ithaca, NY). TEM samples from E1 were embedded in epoxy (EPON-Araldite[®], Huntsman Advanced Materials, Everburg, Belgium) for 4 days at 35°C to prevent sample bending, and then for an additional night at 55°C. An ultramicrotome slice was cut with a thickness of 100 nm and mounted in a Hitachi 7100 TEM. An accelerating voltage of 75 keV was used for imaging.

5.3 Nano-CT Data Collection

A smaller piece (ca. 5 mm equilateral triangle) of E1 with the Kapton backing was cloven from the larger sample and placed in an UltraXRM-L200 (Xradia, Pleasanton, CA) for nano-CT (50 nm resolution, 32.5 nm cubic voxels), which uses a 8 keV laboratory X-ray source, a Fresnel zone plate objective, and Zernike phase contrast, schematically illustrated in Figure 5.1. To stabilize the thin sample in a standing position during nano-CT imaging, a triangular piece was bent with the electrode outward and the two free ends clipped together to create a loop. The radius of curvature was ca. 1 mm, which is two orders of magnitude greater than electrode thickness and thus insignificant.

5.3.1 Image processing

The raw X-ray data was processed by proprietary software (Xradia, Inc.) to generate the unprocessed 3D reconstructions.² Subsequent analysis was performed using MATLAB (Mathworks, Natick, MA). First, MATLAB's image equalization function redistributed the raw grayscale histogram intensities over the entire intensity range to aid in visualizing the data. Then, a thresholding operation split the data into binary values representing solid (agglomerate phase) and void (pore phase). In processing TEM data, we used a similar thresholding technique to split the image into binary solid- and pore-phase data. Using the thresholded data, we characterized the solid agglomerate and pore phase size distributions based on the fitting of inscribed spheres

of different diameter within the volume of each phase. An MIP simulation (described in detail below) was also implemented in MATLAB.

5.4 Results and discussion

Figure 5.2a shows a single 2D, 32.5 nm thick “virtual slice” from the 3D reconstruction of E1 after histogram equalization using MATLAB (Mathworks, Natick, MA). Figure 5.2b shows the 2D slice after binary thresholding into solid and pore phases, with darker shades indicating the solid phase. Initially, we manually chose a threshold value by inspecting images before and after thresholding. The same value was obtained from the isodata thresholding algorithm.¹⁴

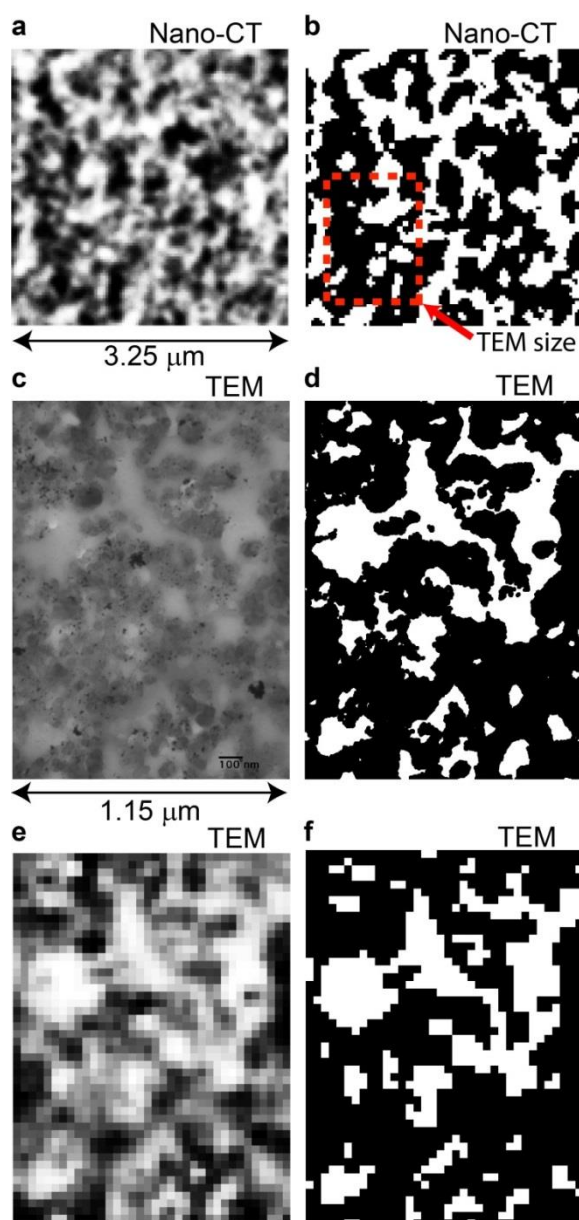


Figure 5.2 Verifying X-ray data with TEM images. a and b, A 2D X-ray slice of E1 before (a) and after (b) binary thresholding. The dark regions represent the solid phase in both images. c, Raw high resolution TEM image of a separate region of E1 with 1.72 nm pixels. d, Image c after binary thresholding to distinguish carbon particles. e, Image c after filtering and resizing for 50 nm resolution with 32.5 nm pixels. f, Image e after binary thresholding. Comparison between images d and f shows the macropore structure is resolved with 50 nm resolution. Images e and f are also qualitatively similar to the X-ray CT slices in images a and b. The dashed box in image b depicts the relative scale of the TEM images.

It is important to identify what microstructure details are lost with 50 nm nano-CT resolution since the constituent materials are smaller (e.g., ca. 40 nm diameter carbon black spheres). Figure 5.2c shows a higher resolution (1.72 nm pixels) TEM image of E1, cut from a different region of the nano-CT sample. Binary thresholding on this image yielded Figure 5.2d, showing a high level of detail that completely resolves carbon spheres. Figure 2c was then de-resolved with a Wiener filter and resized to obtain the pixel size and 50 nm resolution of the nano-CT images. Figure 5.2e shows the de-resolved image. Binary thresholding of Figure 5.2e produced Figure 5.2f, which qualitatively preserved the structure in Figure 5.2d while only losing small, isolated pores and solids. The largest inscribed pore diameter in Figure 5.2f was 260 nm, consistent with the larger pores in the nano-CT images of E1.

The porosity computed from this small TEM sample area was 38% in Figure 5.2d (before de-resolving) and 37% in Figure 5.2f (after de-resolving) using the same thresholding value. Based on the known thickness and composition, the porosity should be 50%. This porosity difference can occur because the ca. 100 nm thick TEM ultramicrotome is several carbon spheres deep, which reduces apparent porosity due to simultaneous imaging of out-of-plane carbon spheres. Another possibility is that the small TEM image is not statistically representative. We also note that agglomerate primary pores are generally difficult to resolve in TEM images.¹⁵

The above comparison of TEM images at different resolutions and with the nano-CT images supports that the 50 nm nano-CT resolution does not thwart characterizing the electrode's agglomerate and secondary pore structure. However, nano-CT cannot resolve the smaller primary pores within the agglomerates.¹⁶ Also, at this time, nano-CT cannot distinguish the thin ionomer films, O(10 nm), within and around the agglomerates. From the preceding 2D and subsequent 3D analyses, it is apparent that the solid phase in nano-CT reconstructions includes the primary pore and ionomer volumes.

Figure 5.3 shows reconstructed 3D images from a cube of nano-CT data (3.25 μm side lengths) for the solid agglomerate and pore phases of E1 and E2, including close up views for E1. This data set is valuable for future computational analysis of transport and electrochemical

phenomena in PEFC electrodes. The computed porosity in the E1 and E2 cubes were 43% and 41%, respectively. The E1 value is close to, but slightly higher than, the de-resolved TEM result of 37% for E1. As described above, this may be because of the lower apparent porosity in TEM imaging and/or the small TEM image area. Indeed, a similar drop in apparent porosity was previously seen between a FIB-SEM reconstruction and a microtome image.¹⁷ Both the nano-CT and TEM porosity values are lower than the 50% calculated from the composition and thickness. As before, this discrepancy is unsurprising – the expected porosity includes the contribution of primary pores that are not considered in the TEM and nano-CT porosity values.

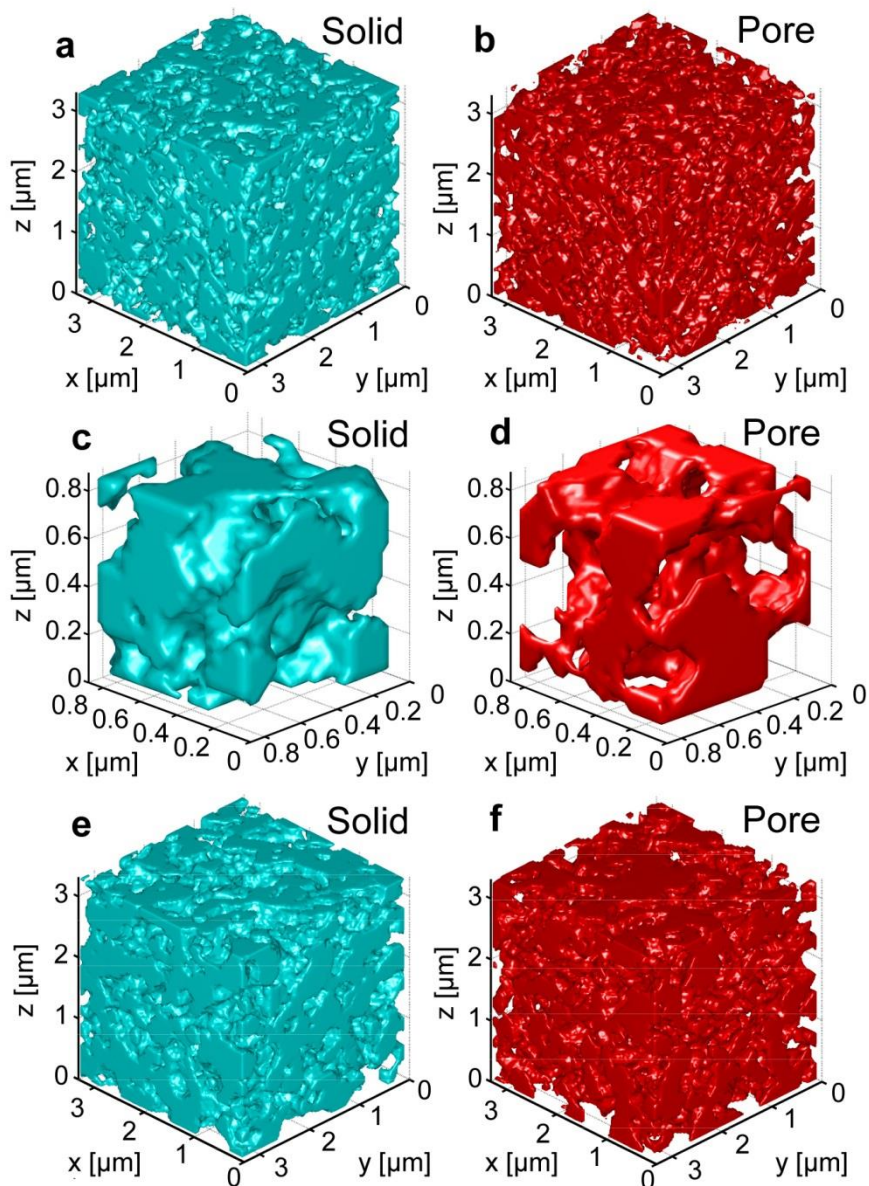


Figure 5.3 3D reconstructions of PEFC electrodes. **a**, The 3D solid phase of E1, which includes the ionomer and primary pores. **b**, The 3D secondary pore phase of E1. **c** and **d**, Magnified views of E1's solid (**c**) and pore (**d**) phase reconstructions. **e** and **f**, 3D reconstructions of E2's solid (**e**) and pore (**f**) phases. The cube dimensions in Images **a**, **b**, **e** and **f** are $3.25 \times 3.25 \times 3.25 \mu\text{m}$. The porosity of the reconstructed E1 and E2 cubes are 43% and 41%, respectively.

MIP was used previously to validate nano-CT results on a solid oxide fuel cell electrode.³ However, that work's omission of the throat effect in analyzing the MIP data led to poor

agreement for larger pores. In our characterization of E1, the nano-CT reconstruction was verified by comparing MIP measurements with morphological MIP simulations on the nano-CT image that account for pore throat effects using an established approach.⁷ The morphological MIP simulation evaluates the intrusion of spheres of decreasing diameter from a face of a 3D reconstruction to mimic the physical MIP process.

For each iteration of decreasing sphere size during the MIP simulation, the sphere diameter corresponds to an effective pore size and a certain pressure during MIP. The difference in diameter between each iteration was limited to the nano-CT's 32.5 nm voxel side length. Starting from one face of the cubic 3D reconstruction space, inscribed sphere fitting determined "seed" sites where a sphere of diameter D could intrude into the sample volume. From these seeds, inscribed spheres of the same diameter were placed in every possible inward direction. Where there was no solid phase overlap, the simulation continued to intrude spheres into adjacent unoccupied volumes. When spheres could proceed in more than one direction, a new sphere seed site and path were initialized. A sphere intrusion branch became "dead" when either a dead-end or a smaller pore throat prevented spheres from being placed in any new direction without solid overlap. After all sphere paths became dead for a given diameter, the volume corresponding to that diameter was computed and inserted to the pore size distribution. With this simulation, the nano-CT data were made to yield pore volumes representative of those measured by MIP.

The insets of Figure 5.4 show pore diameter isosurfaces at several stages of the MIP simulation as the diameter of the intruding spheres was reduced, representing the extent of mercury intrusion from a given starting face. Figure 5.4 presents a comparison of the simulated MIP data versus the MIP measurements. Plots are shown for two sets of simulations: (1) the mean from intrusions starting on all six faces of the largest cube within the nano-CT data and (2) a single simulation for a thicker (6.9 μm), but non-cubic volume. The cube analysis reveals statistical variance. Since mercury does not necessarily percolate through the entire physical sample thickness at lower pressures (larger pores), the thicker nano-CT data set is more useful for comparison with MIP measurements. To compare MIP simulations with the measurements, we normalize the cumulative intruded volume by the total sample volume.

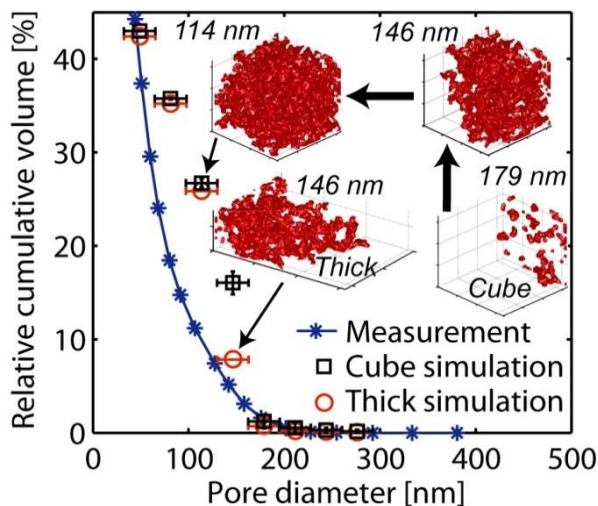


Figure 5.4 Verification of nano-CT for PEFC electrodes with MIP measurement and simulations. MIP measurement for E1 and the corresponding pore size distributions from MIP simulations using the cubic 3D volume of Figure 5.3 (Cube) and a thicker, non-cubic volume (Thick). The relative cumulative volume is the cumulative intrusion volume divided by the total sample volume (sum of pore and solid volumes). The cube simulation's vertical error bars are the 95% confidence internals for the six MIP simulations beginning on each face. The horizontal error bars are plus and minus half the side length of a voxel. Inset: Intrusion isosurfaces for MIP simulations for intruding spheres with diameters of 179, 146, and 114 nm in the cubic simulation, and the same for the thick simulation with 146 nm diameter spheres.

The agreement for large pores in Figure 5.4 is improved over that of earlier solid oxide fuel cell work.³ For the thick simulation, all simulation data are within one voxel side length of the MIP measurement. Altogether, this analysis shows that the thresholded nano-CT data are capturing the pore-size distribution well for pore sizes greater than 50 nm. A useful insight from this analysis is the low anisotropy for MIP in this electrode based on the small vertical error bars for the six simulations on the cube.

Two important outputs of this nano-CT study are the agglomerate- and pore-size distributions, which are useful for evaluating electrode designs and obtaining model inputs. Figure 5.5 displays histograms of the pore- and agglomerate-size distributions based on inscribed spheres, along with related 2D slices of spatial pore- and agglomerate-size distributions. The latter show a sparse distribution of large pores within the volume. The pore-size distribution in Figure 5.5a captures well the larger “secondary” pores, but does not contain information

regarding smaller “primary” pores that may account for roughly 5-10% of this electrode’s total volume. Such a pore size distribution can later be used for evaluating the capillary transport properties for liquid water.¹⁸ The distribution can also be used to calculate an effective diffusion coefficient when considering Knudsen diffusion effects.¹⁹ For example, Knudsen effects result in 65% reduction in diffusivity in a 100 nm pore.¹⁹ Finally, as we will show in the next chapter, the agglomerate size distribution can be used to model PEFC performance more accurately than if one assumes a uniform agglomerate size.

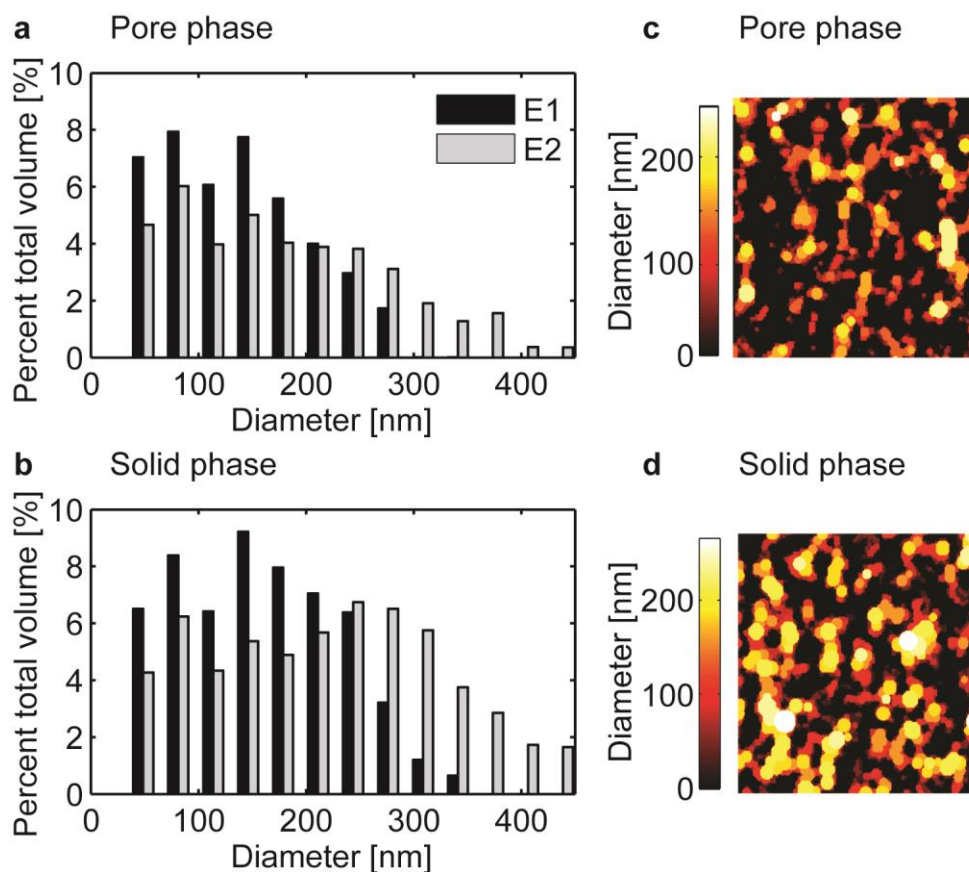


Figure 5.5 Pore and solid phase size distributions for PEFC electrodes. **a**, Solid phase size distributions for E1 and E2. The solid phase volume includes the Nafion and primary pore volumes. The peaks of the solid phase distributions are ca. 150 nm and 240 nm for E1 and E2, respectively. **b**, Pore size distributions for E1 and E2. The size distributions are based on inscribed spheres and are percentages of the total volume. **c** and **d**, Spatial size distributions for the pore (**c**) and solid (**d**) phases in a 2D slice ($3.25\ \mu\text{m} \times 3.25\ \mu\text{m}$) of E1 on the $z = 1.625\ \mu\text{m}$ plane, which is the same plane as Figure 5.2a.

Agglomerate-size peaks can be seen in Figure 5.5b at ca. 150 nm and 240 nm for E1 and E2, respectively; these agree reasonably with characteristic agglomerate sizes found by SAXS,²⁰ TEM,¹⁵ and FIB-SEM.^{1, 17, 21, 22} Unlike the pore phase, the agglomerate-size distribution is not as sensitive to the 50 nm resolution, since the smallest agglomerate length scale is a carbon particle covered by ionomer film ($> 50\ \text{nm}$ diameter). Several PEFC models use an effective agglomerate radius as a critical parameter in modeling the volume-average electrochemical reaction rate. However, an effective diameter from direct 3D measurements has been elusive. Using the solid agglomerate-size distribution in Figure 5.5b, we have calculated the volume-average

agglomerate diameter, D_{avg} , using the agglomerate phase volume fraction, PV , for the i^{th} diameter, D_i , and the volume for that sphere diameter to calculate a volume-average agglomerate volume, $V_{avg} = \sum_i PV_i \pi D_i^3 / 6$. The average diameter is then determined from the equation:

$$D_{avg} = \left[\frac{6}{\pi} V_{avg} \right]^{1/3} = \left[\sum_i PV_i D_i^3 \right]^{1/3} \quad (5.1)$$

We thusly found the average agglomerate diameter to be 188 nm for E1 and 222 nm for E2. These diameters are much smaller than often assumed in models.^{23, 24} Over-estimation of agglomerate size exaggerates the contribution of oxygen diffusion inside the agglomerates in predicting PEFC performance losses, as we will investigate in the next chapter.

5.5 Summary

This chapter presents an X-ray computed tomography reconstruction of two different PEFC electrode samples (E1 and E2) with a resolution of 50 nm and a cubic voxel size of 32.5 nm. De-resolved TEM images verified that the resolution of nano-CT can resolve the 3D structure of the solid and secondary pore phases in the electrode. A 3D image of an electrode reconstructed from the nano-CT data was compared with MIP and showed good agreement for pore radii significantly larger than the nano-CT resolution of 50 nm. A size peak for the solid phase was seen corresponding to characteristic diameters of ca. 150 nm and 240 nm for E1 and E2, respectively. The solid-phase size distribution gave volume-average diameters of 188 nm (E1) and 222 nm (E2) for the imaged volumes. Our analysis has demonstrated nano-CT as a technique valuable for the characterization of a PEFC electrode's 3D structure. The pore size distributions can support the evaluation of liquid water transport and Knudsen diffusion effects during PEFC operation. The agglomerate size distributions and average diameters are valuable for evaluating the dispersion of catalyst ink suspensions and agglomerate-level mass transport effects. Furthermore, the 3D reconstructions can be used for pore-scale numerical simulations. Owing to recent improvements in resolution, nano-CT now has great utility for advancing our understanding of low atomic number porous electrodes, such as those in a PEFC. In the future, nano-CT may permit *in-situ* and even *in-operando* electrode characterization due to its non-destructive nature and flexible sample environment.

5.6 References for Chapter 5

1. H. Schulenburg, B. Schwanitz, J. Krbanjevic, N. Linse, R. Mokso, M. Stampanoni, A. Wokaun and G. G. Scherer, *ECS Trans.*, **33**, 1471 (2010).
2. A. Tkachuk, F. Duewer, H. T. Cui, M. Feser, S. Wang and W. B. Yun, *Z. Kristallogr.*, **222**, 650 (2007).
3. S. H. Lau and et al., *J. Phys. Conf. Ser.*, **152**, 012059 (2009).
4. P. R. Shearing, J. Gelb, J. Yi, W. K. Lee, M. Drakopolous and N. P. Brandon, *Electrochem. Commun.*, **12**, 1021 (2010).
5. J. Eller, T. Rosen, F. Marone, M. Stampanoni, A. Wokaun and F. N. Büchi, *J. Electrochem. Soc.*, **158**, B963 (2011).
6. A. S. Grader and A. B. S. AClark, Computations of Porosity and Permeability of Sparic Carbonate using Muti-Scale CT Images, in *International Symposium of the Society of Core Analysts*, Noordwijk aan Zee, The Netherlands (2009).
7. P.-Z. Wong, *Methods in the Physics of Porous Media*, Academic Press, San Diego (1999).
8. M. Dierolf, A. Menzel, P. Thibault, P. Schneider, C. M. Kewish, R. Wepf, O. Bunk and F. Pfeiffer, *Nature*, **467**, 436 (2010).
9. Y. S. Chu, J. M. Yi, F. De Carlo, Q. Shen, W. K. Lee, H. J. Wu, C. L. Wang, J. Y. Wang, C. J. Liu, C. H. Wang, S. R. Wu, C. C. Chien, Y. Hwu, A. Tkachuk, W. Yun, M. Feser, K. S. Liang, C. S. Yang, J. H. Je and G. Margaritondo, *Appl. Phys. Lett.*, **92**, 3 (2008).
10. F. Büchi, J. Eller, F. Marone and M. Stampanoni, *ECS Trans.*, **33**, 1397 (2010).
11. J. Eller, J. Roth, F. Marone, M. Stampanoni, A. Wokaun and F. N. Büchi, *J. Power Sources*, **245**, 796 (2014).
12. M. S. Wilson, J. A. Valerio and S. Gottesfeld, *Electrochim. Acta*, **40**, 355 (1995).
13. J. Xie, F. Garzon, T. Zawodzinski and W. Smith, *J. Electrochem. Soc.*, **151**, A1084 (2004).
14. T. W. Ridler and S. Calvard, *Ieee Transactions on Systems Man and Cybernetics*, **8**, 630 (1978).

15. J. Xie, D. L. Wood, K. L. More, P. Atanassov and R. L. Borup, *J. Electrochem. Soc.*, **152**, A1011 (2005).
16. M. Uchida, Y. Aoyama, N. Eda and A. Ohta, *J. Electrochem. Soc.*, **142**, 4143 (1995).
17. S. Zils, M. Timpel, T. Arlt, A. Wolz, I. Manke and C. Roth, *Fuel Cells*, **10**, 966 (2010).
18. A. Z. Weber, R. M. Darling and J. Newman, *J. Electrochem. Soc.*, **151**, A1715 (2004).
19. D. Mu, Z. S. Liu, C. Huang and N. Djilali, *Microfluidics and Nanofluidics*, **4**, 257 (2008).
20. F. Xu, H. Y. Zhang, J. Ilavsky, L. Stanciu, D. Ho, M. J. Justice, H. I. Petrache and J. A. Xie, *Langmuir*, **26**, 19199 (2011).
21. C. Ziegler, S. Thiele and R. Zengerle, *J. Power Sources*, **196**, 2094 (2011).
22. C. S. Kuroda and Y. Yamazaki, *ECS Trans.*, **11**, 509 (2007).
23. N. P. Siegel, M. W. Ellis, D. J. Nelson and M. R. von Spakovsky, *J. Power Sources*, **115**, 81 (2003).
24. W. Sun, B. A. Peppley and K. Karan, *Electrochim. Acta*, **50**, 3359 (2005).

6 Effects of an Experimental Agglomerate Size Distribution on the PEFC Agglomerate Model

6.1 Introduction

The agglomerate model for PEFC electrodes¹⁻¹⁶ uses analytical solutions to coupled oxygen diffusion and the reduction reaction in an idealized, spherical agglomerate. It thereby offers a more detailed physical and mathematical description of the transport processes in the electrode compared to the macro-homogeneous or interface approaches.² However, most prior implementations of the agglomerate model have assumed a single, representative agglomerate diameter¹⁻¹⁵ (though a few works^{3, 7, 13} parametrically vary the agglomerate diameter) and do not consider the non-uniform size distributions that actually exist within an electrode. One notable exception is Yoon and Weber,¹⁶ who consider a deliberate gradient of agglomerate sizes from the membrane to the diffusion medium. In that approach, the agglomerate size is still a single value across a plane of constant depth. They modeled a hypothetical engineered agglomerate size gradient to examine the possible benefit. Here the causality is flipped: we consider a naturally arising size distribution derived from experimental characterization, and examine how it affects the oxygen reduction reaction (ORR) rates predicted by the agglomerate porous electrode model.

In Chapter 5, we used nano-scale x-ray computed tomography (nano-CT) with 50 nm resolution to reconstruct the 3D microstructure of PEFC electrodes (Figure 6.1a). The reconstructions were verified using other established characterization techniques. In the solid-phase geometry, we fit inscribed spheres to obtain an agglomerate diameter distribution (Figure 6.1b). In this chapter, this particular geometry will be incorporated into a simplified agglomerate model to demonstrate the impact of a natural agglomerate diameter distribution on ORR rate predictions. In this chapter, we do not model the performance of an entire fuel cell, nor do we use the model to predict the overall voltage-current behavior. Instead, we consider an idealized volume slice within the electrode (Figure 6.2) in which the oxygen concentration in the secondary pores surrounding the agglomerates and the electric potentials are uniform. We thereby focus on the significant difference in predictions incurred by incorporating the agglomerate diameter distribution, when compared to the usual assumption of a single,

representative agglomerate size. An advantage of this approach is that it is general. The results we present are relative, not absolute, and they provide a framework for considering agglomerate diameter distributions in a full fuel cell model.

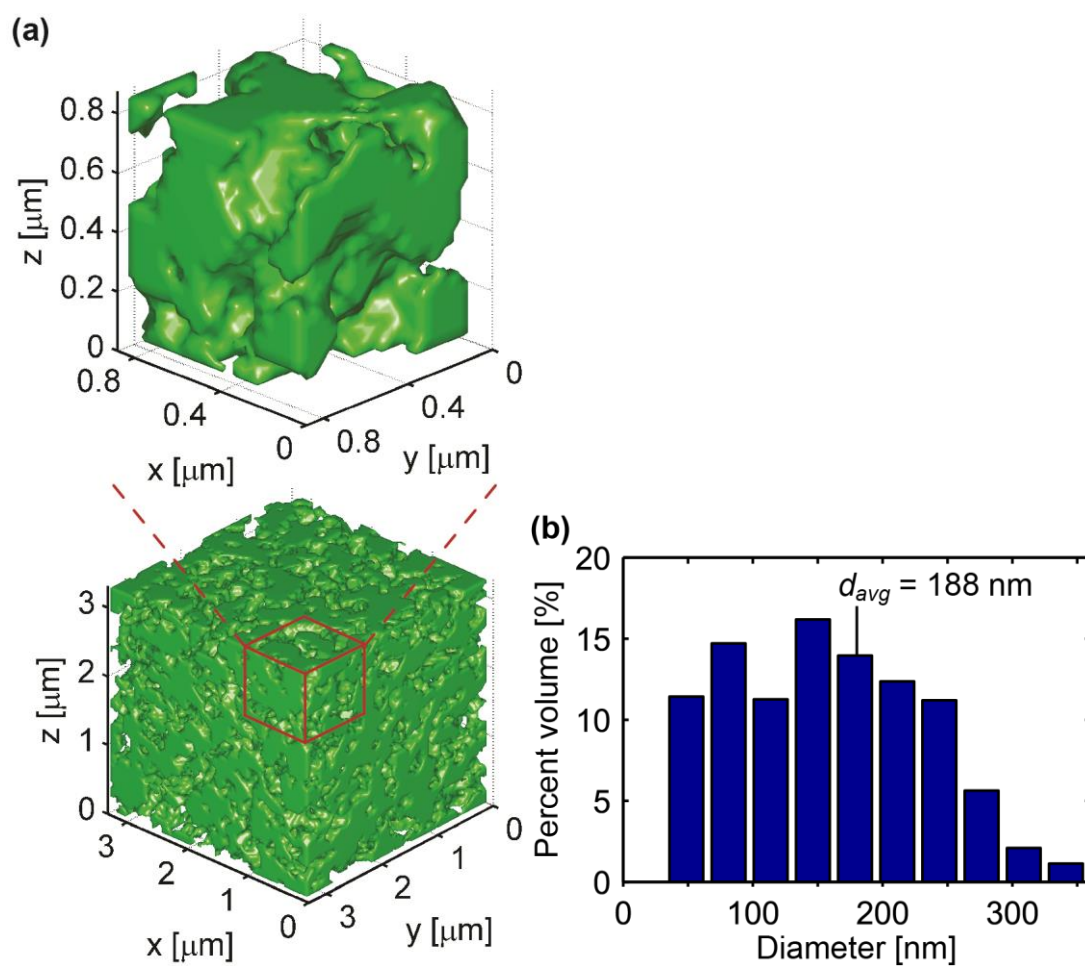


Figure 6.1 Nano-CT characterization of a PEFC electrode's microstructure. a, Nano-CT reconstruction (50 nm resolution) of the solid phase of a PEFC electrode, from Chapter 5. b, Histogram showing the agglomerate diameter distribution, found by fitting inscribed spheres into the reconstruction shown in image a. The displayed average diameter of 188 nm was computed using volumetric weighting of each agglomerate bin.

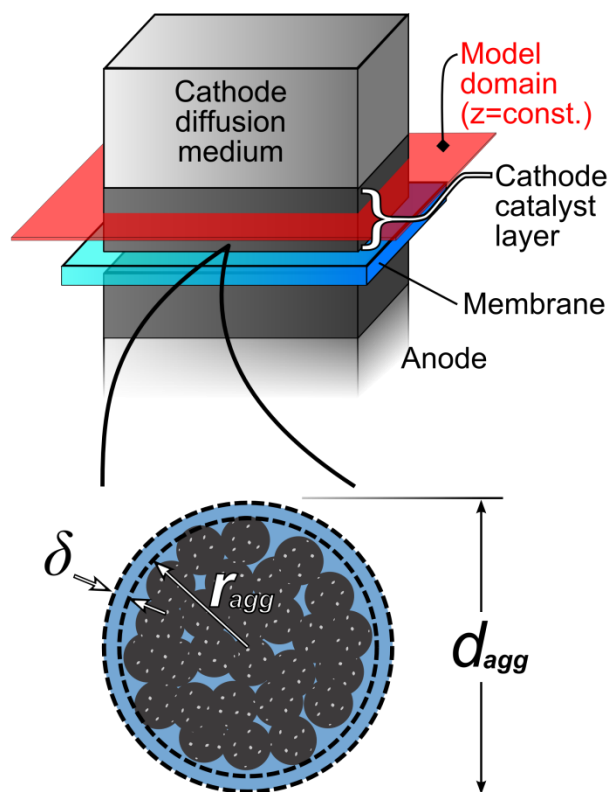


Figure 6.2 Schematic of the model domain. The model presented here considers a small area slice of the catalyst layer at constant depth, in which the gas phase oxygen concentration in the secondary pores and electric potentials are constant. The bottom image depicts nomenclature concerning the spherical agglomerates. Note that the agglomerate diameter includes the ionomer film for comparison to physically measured values, whereas r_{agg} does not, to conform with the method of Thiele.¹⁷

6.2 Theory

To evaluate the effect of the agglomerate diameter distribution on the predicted reaction rate, we first use the solid-phase diameter distribution in Figure 6.1b to estimate a distribution of agglomerate effectiveness factors, drawing on expressions from Sun et al.¹ based on the original work by Thiele.¹⁷ The effectiveness factor represents the reaction rate within an agglomerate divided by the hypothetical reaction rate if transport were infinitely facile. A value close to unity is optimal: this means intra-agglomerate O_2 transport is not hindering the reaction rate. The effectiveness factor is given by

$$E_r = \frac{1}{\Phi_L} \left(\frac{1}{\tanh(3\Phi_L)} - \frac{1}{3\Phi_L} \right) \quad (6.1)$$

where Thiele's modulus, Φ_L , is given below by Eq. (6.2), in which r_{agg} represents the radius of the agglomerate up to, but not including, an assumed surrounding ionomer film; k_c is the ORR rate constant (given by Eq. (6.3)); D is the diffusivity of O_2 in Nafion[®]; and ε_{agg} is the agglomerate ionomer fraction, which represents the volume fraction of ionomer within the agglomerate (not including the surrounding ionomer film).

$$\Phi_L = \frac{r_{agg}}{3} \sqrt{\frac{k_c}{D\varepsilon_{agg}^{1.5}}} \quad (6.2)$$

The ORR rate constant is found from the Butler-Volmer equation as:

$$k_c = \frac{a_{Pt}}{4Ff_{agg}} \frac{i_0}{c_{O_2}} \left[\exp\left(\frac{\alpha_c n F \eta_c}{RT}\right) - \exp\left(\frac{-(1-\alpha_c) n F \eta_c}{RT}\right) \right] \quad (6.3)$$

where a_{Pt} is the electrochemically active volumetric surface area of platinum, F is Faraday's constant, f_{agg} is the electrode's volume fraction of agglomerates not including ionomer film (calculated based on the diameter distribution, the ink composition, a known electrode thickness from TEM, and the assumed thickness δ of the ionomer film), i_0 is the exchange current density, c_{O_2} is the reference oxygen concentration associated with i_0 , α_c is the cathodic transfer coefficient, n is the number of electrons transferred in the rate limiting step of the reaction, and η_c is the representative local overpotential. We note that recent work has suggested the ORR to have an order less than unity.¹⁸ Yoon and Weber¹⁶ have implemented this finding into an agglomerate model. However, to keep with examining the established agglomerate model in this work, we assume a reaction order of 1 for the ORR, as evident in Eq. (3). Also note that k_c is not a size-dependent value. Agglomerate-level transport losses enter the model via the effectiveness factor (above) and the agglomerate model's reaction rate equation (below), both of which call upon k_c , but the latter does not change with agglomerate size.

From the distribution of agglomerate effectiveness factors, we calculate a volumetric distribution of reaction rate vs. agglomerate radius. The volumetric reaction rate in an agglomerate is given by:

$$j_{ORR} = 4F \frac{p_{O_2}}{H} \left[\frac{1}{E_r k_c f_{agg}} + \frac{r_{agg} \delta}{a_{agg} D (r_{agg} + \delta)} \right]^{-1} \quad (6.4)$$

where p_{O_2} is the local partial pressure of oxygen, H is Henry's constant, and a_{agg} is the agglomerate surface area per unit catalyst volume, taken to be $3f_{agg} / r_{agg}$, which is found from the surface area of a sphere of active material (radius r_{agg}) divided by its volume, scaled by the electrode's volume fraction of the active material in the agglomerate (excludes outer film), f_{agg} . Note that the form of j_{ORR} presented in Eq. (6.4) differs from Eq. 8 in Sun et al.¹ We present a derivation in Appendix A that explains in more detail. In short, the difference is the inversion of $r_{agg} / (r_{agg} + \delta)$ in the second term. Although Sun et al. use a different form, the inversion of the fraction does not substantially impact the model results for the larger agglomerate sizes they model. The effect is more significant for smaller (order of 100 nm) agglomerates, where the original form results in an unphysical, non-monotonic dependence on diameter. Some of the agglomerates considered in the present work are in that size range.

To understand the effects of the agglomerate size distribution, the quantity we wish to evaluate is the fraction of the total reaction rate carried by each agglomerate diameter, PJ_i . This is done by finding the reaction rate for each agglomerate diameter, weighting it by the volume V_i occupied by agglomerates of that diameter, and dividing it by the total reaction rate for the electrode:

$$PJ_i = \frac{(j_{ORR})_i V_i}{\sum_i [(j_{ORR})_i V_i]} \quad (6.5)$$

It is important to note that, since j_{ORR} has a linear dependence on p_{O_2} and H , those terms cancel out in this ratio – so long as they are constant. Since we wish to demonstrate the effect of a non-uniform agglomerate diameter distribution on the model predictions, we consider a simplified system where p_{O_2} is uniform in the gas phase – this could be considered as a small plane of electrode at constant depth within a catalyst layer.

It is important to note that, since j_{ORR} has a linear dependence on p_{O_2} and H in this model, those terms cancel out in this local ratio as shown here:

$$PJ_i = \frac{\frac{4F}{H} p_{O_2} \left[\frac{1}{E_r k_c f_{agg}} + \frac{r_{agg} \delta}{a_{agg} D(r_{agg} + \delta)} \right]^{-1} V_i}{\sum_i \left[\left(\frac{4F}{H} p_{O_2} \left[\frac{1}{E_r k_c f_{agg}} + \frac{r_{agg} \delta}{a_{agg} D(r_{agg} + \delta)} \right]^{-1} \right) V_i \right]} \quad (6.6)$$

Since we wish to demonstrate the effect of a non-uniform agglomerate diameter distribution on the model predictions, we consider a simplified system where p_{O_2} is uniform in the gas phase – this could be considered as a small plane of electrode at constant depth within a catalyst layer, as depicted in Figure 6.2. Hence, for each current density considered, the gas phase p_{O_2} is the same regardless of the agglomerate size.

For the sake of simplicity in this demonstrative model implementation, we made the following further assumptions and generalizations regarding the agglomerate model:

- Because we are considering a planar volume of electrode with a uniform p_{O_2} , the overpotential, η_c is also uniform throughout the electrode plane.
- The effect of liquid water is not considered. This is in part a consequence of considering relative contributions within an idealized volume of constant p_{O_2} .
- The Nafion film thickness δ was taken to be 10 nm, as assumed in other works.¹ This thickness was also recently validated by energy-filtered TEM imaging, which found the thickness to be roughly 7 nm.¹⁹
- Excluding the ionomer film surrounding them, all agglomerates were assumed to have identical volumetric composition (i.e. ϵ_{agg} is the same for all agglomerates). The values of 22% and 34% for ϵ_{agg} and f_{agg} were estimated from the nano-CT reconstruction in concert with the assumed value of δ and the known ink composition.
- As in other implementations,^{1, 2, 4-13, 15, 16} the inside of the agglomerate is considered entirely solid material (C, Pt, and ionomer). This is a reasonable simplification: in our recent nano-CT work,²⁰ a comparison between the nano-CT-determined porosity and the expected porosity (calculated from the ink composition and electrode thickness) indicates that the inside of the agglomerates should be roughly 10% porous.

- The volume-average electrochemically active Pt surface area, a_{Pt} , of $1.04 \times 10^7 \text{ m}^2_{Pt}/\text{m}^3_{CL}$ was calculated using H_2/N_2 cyclic voltammetry performed in our lab on an electrode of composition identical to that of Figure 6.1.
- Other physical values are the same as in Ref. ¹.

6.3 Results and Discussion

Figure 6.3a shows the general effect of agglomerate diameter on the effectiveness factor at three different cathode overpotentials according to Eq. (6.1). Note that unlike r_{agg} in Equations (6.2) and (6.4), diameter values reported in this work include the ionomer film (see Figure 6.2). The discrepancy is because r_{agg} is a transport length and a model input, whereas diameter values are for comparison to physical agglomerate sizes as measured in morphological characterization. Figure 6.3b shows the contribution to the total reaction rate from agglomerates of different diameters, calculated by Eq. (6.5) in conjunction with each agglomerate diameter's percent volume from Figure 6.1b. The overpotentials in these plots of 0.5, 0.6, and 0.7 V were selected to represent a range in which mass transport effects are significant. An important observation of Figure 6.3b is that at the lowest overpotential, the reaction rate distribution follows the volumetric distribution of diameter, since all diameters are similarly effective and primarily activation limited. However, at higher overpotentials (and hence higher currents), the smaller agglomerates with their shorter diffusion length scales and consequently higher effectiveness factors contribute to more of the total reaction rate, despite still occupying the same physical volume fraction. Thus, the reaction rate distribution shifts to smaller diameters.

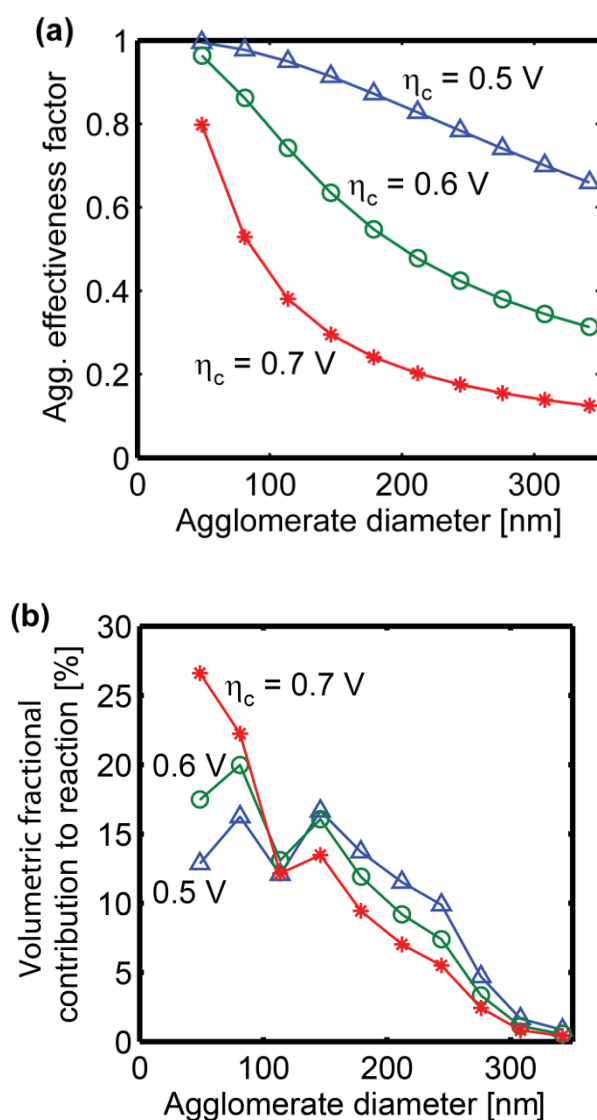


Figure 6.3 The agglomerate diameter and contribution to reaction rate. a, The effect of agglomerate diameter on effectiveness factor at cathode overpotentials of 0.7 V (red squares), 0.6 V (green circles), and 0.5 V (blue triangles). b, The volumetric fractional contribution to the overall cathode reaction for each agglomerate diameter, based on the volumetric distribution of effectiveness factors.

As noted earlier, prior uses of the agglomerate model have assumed a single agglomerate diameter¹⁻¹⁵ or an imposed size gradient.¹⁶ Consequently, a utility of the distribution in Figure 6.1b is to extract a single “effective” agglomerate diameter, d_{eff} , that yields equivalent ORR rates to predictions obtained using the agglomerate diameter distributions. In other words, if we assume a single agglomerate diameter, d_{eff} , and implement the agglomerate model, we obtain

some overall reaction rate, $j_{tot} = j_{ORR}(d_{eff}, \eta_c)$. Thus, instead of calculating a volume-average or surface-area-average diameter value, we are seeking the value of d_{eff} that yields the same overall reaction rate, j_{tot} , as when we calculate it based on the results from Eqs. (6.4) and (6.5) for the measured agglomerate diameter distribution:

$$j_{tot} = \sum_i PJ_i j_{ORR,i} \quad (6.7)$$

However, since both j_{tot} and each agglomerate-diameter's relative contribution to j_{tot} , PJ_i , depend on overpotential (see Figure 6.3b), d_{eff} must also depend on overpotential. Figure 6.4a presents the effective diameters calculated from the reaction rate. Note that the range of overpotentials plotted extends from 0 V all the way to 1 V. Overpotentials as high as 1 V are not common for PEFC operation, but are relevant nonetheless since they are used in studies of limiting current, which are often used to extract electrode transport parameters,²¹⁻²⁶ including estimates of the agglomerate radius.²⁶ At more common overpotentials near 0.6 V, Figure 4a still exhibits substantial departure from the low overpotential value. The plot exhibits the strong dependence of the effective diameter, d_{eff} , on the overpotential. The trend toward smaller values of d_{eff} at higher overpotentials (higher currents) is consistent with our earlier finding that as overpotential increases, the relative contribution to reaction rate by smaller agglomerates also increases.

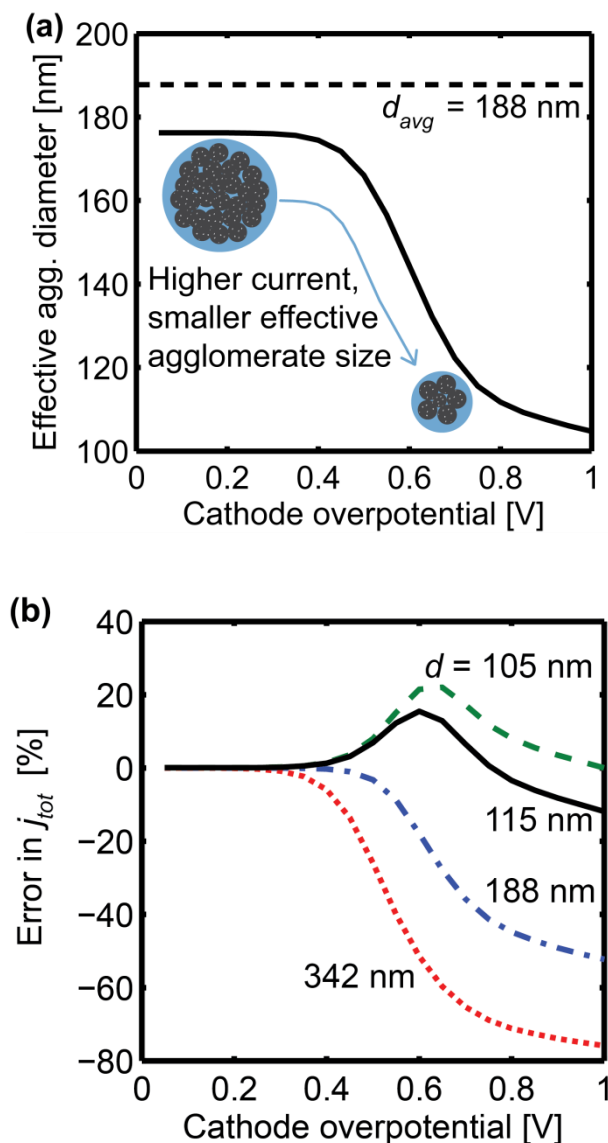


Figure 6.4: Relationship between agglomerate diameter choice and model predictions as a function of overpotential. a, The effective agglomerate diameter, d_{eff} , versus overpotential. The volume-average diameter d_{avg} is shown for comparison. b, For each choice of agglomerate diameter (shown on figure for each curve), the error in j_{tot} when assuming a single agglomerate diameter. The baseline for computing the error is the value found by Equation (6.7), which accounts for the experimental agglomerate diameter distribution.

The agglomerate diameters shown in Figure 6.1b are small compared to the assumed agglomerate diameter in many previous implementations of the agglomerate model.^{1, 2, 4, 6, 7, 10-14} However, the range of sizes used here are in good agreement with prior SAXS,²⁷ TEM,²⁸ and

FIB-SEM²⁹⁻³² studies. Even assuming a single, smaller diameter like those of Figure 6.1b, the errors possible are significant. If the resulting j_{tot} values from Eq. (6.7) are taken as the “correct” values, we can calculate the error incurred by assuming a single agglomerate diameter as a function of overpotential. Figure 6.4b shows these errors in j_{tot} over a range of overpotentials for several different choices of agglomerate diameter.

In Figure 6.4b, we display three possible agglomerate diameter choices based on the nano-CT reconstructions: the largest diameter (342 nm), the volume-average diameter (188 nm), and the smallest value of d_{eff} (105 nm) in Figure 6.4a. From among these choices, the model can over-predict the reaction rate by as much as 20% and under-predict it by as much as 70%. We also sought the agglomerate diameter that yields the lowest error across the entire range of overpotentials. A choice of 115 nm (± 2.5 nm) neither over- nor under-predicted j_{tot} by more than 15%; this choice is also shown in Figure 6.4b.

As evident in Figure 6.4b, the errors arising from assuming a single agglomerate diameter are highly sensitive to both the assumed agglomerate diameter and the overpotential. This indicates that one should exercise caution when assuming a single agglomerate diameter. However, if one does make this assumption, the analysis presented here suggests that one should assume an agglomerate diameter smaller than the volume average.

As discussed above, the error incurred by assuming a single agglomerate size is significant, but it can be kept reasonably small if one makes a wise choice of agglomerate size, and if the range of overpotentials being modelled is moderate. However, the effect of a distribution of sizes becomes more significant as the characteristic agglomerate size increases. This is particularly relevant considering that a recent push in PEFC research is to develop non-platinum-group-metal (non-PGM) catalyst layers to reduce reliance on expensive platinum catalysts.^{33, 34} In unpublished nano-CT studies (manuscript in preparation) of a particular non-PGM catalyst layer, our colleagues have found the agglomerates to be much larger and the CLs much thicker. In the particular CL measured, agglomerates ranged from 0.6 to 8 μm , with a mean diameter of 2.4 μm . At these larger sizes, the size distribution has a more severe impact. Figure 6.5 shows polarization curves generated by these colleagues using the agglomerate model, implemented in

full in a whole-thickness PEFC domain. The two curves show the results using the mean diameter of 2.4 μm , and using the full distribution of agglomerate sizes. The assumption of only one mean diameter causes the apparent maximum current density to be less than half of the values predicted by the distributed-size model. Hence, the findings in this work are particularly important in novel CL architectures with larger agglomerates.

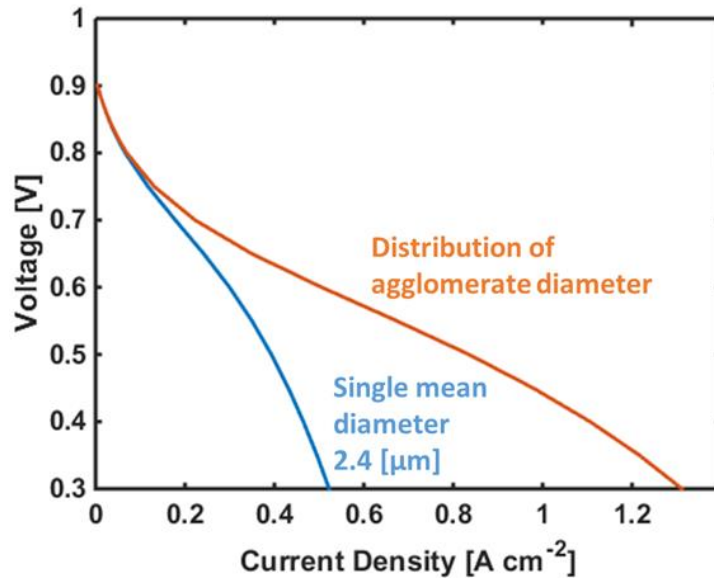


Figure 6.5 Output polarization curves of a full non-PGM PEFC performance model based on the agglomerate framework, calculated using a single, uniform agglomerate diameter (blue) and a real distribution of agglomerate sizes (red). The range of agglomerate diameters was 0.6 to 8 μm with a mean of 2.4 μm , which is a typical agglomerate size distribution for these particular novel non-PGM catalyst layers.

6.4 Implementing the Local Pt|Nafion Oxygen Resistance

6.4.1 Derivation in the General Agglomerate Model Framework

In order to implement the additional “local” ionomer/Pt-level O_2 transport resistance³⁵⁻³⁹ into the agglomerate model framework, we must first bring that resistance into familiar terms. The work by Suzuki et al.³⁵ defines the interfacial oxygen transport resistance k_{local} (units: m/s) in terms of the flux $N'_{\text{O}_2,G/L}$ at the binder/gas interface (denoted as G/L):

$$N'_{\text{O}_2,G/L} = -k_{local} (c_{eq} - c_{G/L}) \quad (6.8)$$

where c_{eq} is the equilibrium concentration (p_{O_2} / H by Henry's law) just inside the binder's surface, and $c_{G/L}$ is the actual concentration just inside the binder when there is flux.

Because we later define current in terms of the flux at the L/S (binder/catalyst) interface, $N'_{O_2,L/S}$, it behooves us to write the above expression in terms of that. While the flux at G/L and at L/S is not the same (due to the changing area), the molar transport rate (area times flux) is the same. In other words,

$$N'_{O_2,G/L} = N'_{O_2,L/S} \frac{4\pi r_{agg}^2}{4\pi (r_{agg} + \delta)^2} \quad (6.9)$$

Substituting (6.9) into Eq. (6.8) and solving for $c_{G/L}$, we obtain

$$c_{G/L} = \frac{N'_{O_2,L/S}}{k_{local}} \left(\frac{r_{agg}^2}{(r_{agg} + \delta)^2} \right) + c_{eq} \quad (6.10)$$

First, we must collect the necessary tools from the prior derivation done in the previous sections. Earlier, we used knowledge of mass conservation and Thiele's method to obtain the following relationship between $c_{L/S}$ and $c_{G/L}$:

$$\text{Prior knowledge:} \quad c_{L/S} \left[1 + \frac{E_r k_c f_{agg} r_{agg} \delta}{a_{agg} D (r_{agg} + \delta)} \right] = c_{G/L} \quad (6.11)$$

By similar methods, we also know that the flux at the L/S interface is:

$$\text{Prior knowledge:} \quad N'_{O_2,L/S} = - \frac{E_r k_c f_{agg}}{a_{agg}} c_{L/S} \quad (6.12)$$

And, finally,

$$\text{Prior knowledge:} \quad \nabla \cdot i = 4FE_r k_c f_{agg} c_{L/S} \quad (6.13)$$

Now, we are prepared to combine the new resistance with prior expressions. Substituting Eq. (6.10) into (6.11), and then replacing $N'_{O_2,L/S}$ using Eq. (6.12), we obtain:

$$c_{L/S} + \left(\frac{E_r k_c f_{agg}}{a_{agg}} \right) \left(\frac{r_{agg} \delta}{(r_{agg} + \delta) D} \right) c_{L/S} = \frac{r_{agg}^2}{k_{local} (r_{agg} + \delta)^2} \left(\frac{-E_r k_c f_{agg}}{a_{agg}} \right) c_{L/S} + c_{eq} \quad (6.14)$$

where the right side is the new part (formerly, it was simply $c_{G/L}$ which was treated by Henry's law.

Solving this for $c_{L/S}$, we obtain:

$$c_{L/S} = c_{eq} \left[1 + \left(\frac{r_{agg}^2}{k_{local} (r_{agg} + \delta)^2} + \frac{r_{agg} \delta}{(r_{agg} + \delta) D} \right) \left(\frac{E_r k_c f_{agg}}{a_{agg}} \right) \right]^{-1} \quad (6.15)$$

To prepare for a substitution, we multiply numerator and denominator by the same expression to obtain:

$$c_{L/S} = \frac{c_{eq}}{E_r k_c f_{agg}} \left[\frac{1}{E_r k_c f_{agg}} + \left(\frac{r_{agg}^2}{k_{local} (r_{agg} + \delta)^2} + \frac{r_{agg} \delta}{(r_{agg} + \delta) D} \right) \left(\frac{1}{a_{agg}} \right) \right]^{-1} \quad (6.16)$$

Finally, substituting Eq. (6.16) into (6.13) and using Henry's law ($c_{eq} = p_{O_2} / H$), and cancelling the $E_r k_c f_{agg}$ terms outside of the brackets, we obtain the final expression for the volumetric current density (expressed in some references as the divergence of current):

$$j_{ORR} = 4F \frac{p_{O_2}}{H} \left[\frac{1}{E_r k_c f_{agg}} + \frac{r_{agg}^2}{k_{local} a_{agg} (r_{agg} + \delta)^2} + \frac{r_{agg} \delta}{a_{agg} D (r_{agg} + \delta)} \right]^{-1} \quad (6.17)$$

Note that the existence of the middle term in the brackets is the only difference between Eq. (6.17) and our prior version where we did not incorporate the local resistance. We can also rearrange slightly to a more compact form:

$$j_{ORR} = 4F \frac{p_{O_2}}{H} \left[\frac{1}{E_r k_c f_{agg}} + \frac{r_{agg}}{a_{agg} (r_{agg} + \delta)} \left(\frac{r_{agg}}{k_{local} (r_{agg} + \delta)} + \frac{\delta}{D} \right) \right]^{-1} \quad (6.18)$$

6.4.2 Impact of Local Resistance

Once the expression for the volumetric current density including k_{local} is obtained in Eq. (6.18), we can combine it with the size distribution framework using Eqs. (6.6) and (6.7) – in other words, we simply replace the expressions for j_{ORR} in Section 6.2 with that in Eq. (6.18). After doing so, choosing a value of k_{local} of 0.004 m/s from Suzuki et al.,³⁵ we can perform the

same analyses presented in Section 6.2; the results of this are shown in Figure 6.6. As expected, the inclusion of k_{local} increases the severity of mass transport resistance. Since smaller agglomerates are less affected by mass transport resistance, the result is a shifting towards lower effective agglomerate diameters. In other words, similar to before, the more severe the mass transport effects, the more contribution comes from smaller agglomerates in the distribution, whether the increased effect of mass transport resistance is coming from higher reaction rate or from an additional resistance term.

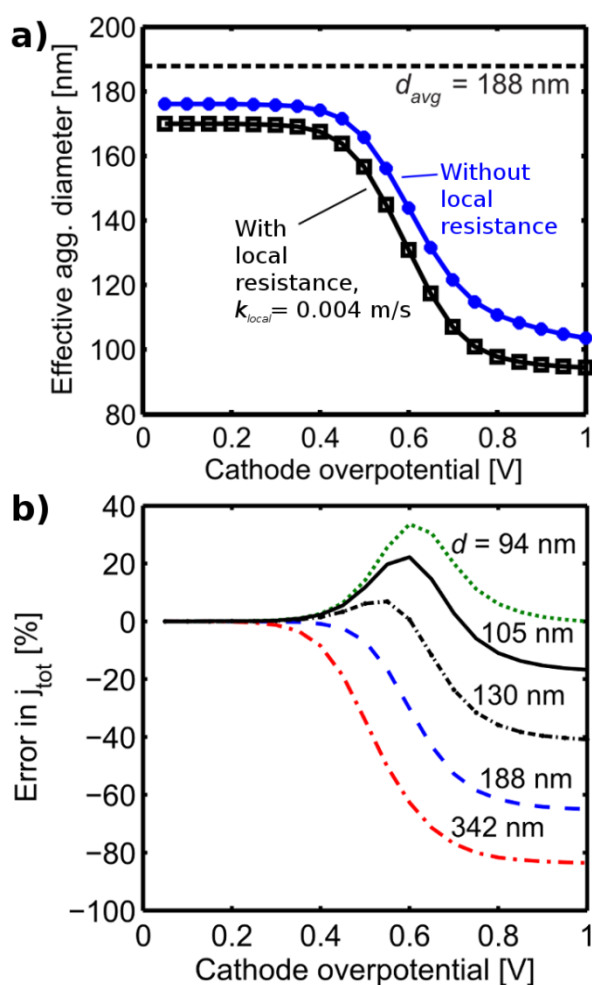


Figure 6.6 Effect of a small local Pt|Nafion level transport resistance on the results of Figure 6.4.

6.5 Summary

The agglomerate model of PEFC electrodes typically assumes a single agglomerate diameter when simulating PEFC performance. The primary goal of this chapter is to demonstrate the importance of an agglomerate size distribution for accurate predictions with an agglomerate model. For this reason, we did not employ a rigorous, full thickness model, as the development and implementation of it would detract from the simpler primary finding. Instead, we used a simplified agglomerate model on a representative elementary volume within the electrode without variations of the gas phase oxygen concentration in the secondary pores or of the electrolyte potential.

We investigated the effect of an agglomerate size distribution using a diameter distribution measured from nano-CT imaging of a typical PEFC electrode. We found a substantial difference between the results of a model that assumes a single agglomerate diameter versus a model that accounts for a size distribution. The error between the agglomerate model with a single diameter and the agglomerate model with a diameter distribution is highly sensitive to both overpotential and the choice of agglomerate diameter. For our particular geometry obtained from nano-CT imaging, we found that an agglomerate diameter of 115 nm yields the lowest error across a broad range of overpotentials, but it still errs by as much as 15%. Although we believe these results are representative, the exact values are not universal and do depend on the size distribution of a particular electrode. In our previous nano-CT measurements, we identified a notable change in the agglomerate size distributions with modest alterations of the electrode preparation procedure. A shift towards larger agglomerates causes the effect to become more significant. For example, with the dramatically larger (0.6 - 8 μm) agglomerates present in novel non-PGM catalyst layers, there is a difference of more than double the current in agglomerate model predictions depending on whether a single size is assumed or a distribution of sizes is considered. The inclusion of a local Pt|Nafion-level resistance to O_2 transport also enhances the difference between a distribution of sizes and a single agglomerate size.

In this chapter, we did not directly model an entire fuel cell electrode, but instead modelled a representative planar sub-volume with constant oxygen concentration. This framework could be used in a full-scale agglomerate model by using Eq. (6.7) for j_{tot} as the sink term in a model. In a

later chapter, we will do so by building a 0-D (no spatial variation in performance) PEFC model and calculating polarization curves to match experimental PEFC performance measurements.

6.6 References

1. W. Sun, B. A. Peppley and K. Karan, *Electrochim. Acta*, **50**, 3359 (2005).
2. D. Harvey, J. G. Pharoah and K. Karan, *J. Power Sources*, **179**, 209 (2008).
3. Z. T. Xia, Q. P. Wang, M. Eikerling and Z. S. Liu, *Can. J. Chem.*, **86**, 657 (2008).
4. M. Secanell, K. Karan, A. Suleman and N. Djilali, *Electrochim. Acta*, **52**, 6318 (2007).
5. S.-M. Chang and H.-S. Chu, *J. Power Sources*, **161**, 1161 (2006).
6. N. Khajeh-Hosseini-Dalasm, S. Ahadian, K. Fushinobu, K. Okazaki and Y. Kawazoe, *J. Power Sources*, **196**, 3750 (2010).
7. S. Obut and E. Alper, *J. Power Sources*, **196**, 1920 (2011).
8. A. A. Shah, G. S. Kim, W. Gervais, A. Young, K. Promislow, J. Li and S. Ye, *J. Power Sources*, **160**, 1251 (2006).
9. T. Sousa, M. Mamlouk and K. Scott, *Chem. Eng. Sci.*, **65**, 2513 (2010).
10. N. P. Siegel, M. W. Ellis, D. J. Nelson and M. R. von Spakovsky, *J. Power Sources*, **115**, 81 (2003).
11. K. Broka and P. Ekdunge, *J. Appl. Electrochem.*, **27**, 281 (1997).
12. F. Jaouen, G. Lindbergh and G. Sundholm, *J. Electrochem. Soc.*, **149**, A437 (2002).
13. F. Gloaguen and R. Durand, *J. Appl. Electrochem.*, **27**, 1029 (1997).
14. P. K. Das, X. Li and Z.-S. Liu, *J. Power Sources*, **179**, 186 (2008).
15. M. L. Perry, J. Newman and E. J. Cairns, *J. Electrochem. Soc.*, **145**, 5 (1998).
16. W. Yoon and A. Z. Weber, *J. Electrochem. Soc.*, **158**, B1007 (2011).
17. E. W. Thiele, *Industrial & Engineering Chemistry*, **31**, 916 (1939).
18. K. C. Neyerlin, W. Gu, J. Jorne and H. A. Gasteiger, *J. Electrochem. Soc.*, **153**, A1955 (2006).
19. M. Lopez-Haro, L. Guétaz, T. Printemps, A. Morin, S. Escribano, P.-H. Jouneau, P. Bayle-Guillemaud, F. Chandezon and G. Gebel, *Nature Communications*, **5**, 5229 (2014).
20. W. K. Epting, J. Gelb and S. Litster, *Adv. Funct. Mater.* (2011).
21. M. V. Williams, H. R. Kunz and J. M. Fenton, *J. Electrochem. Soc.*, **152**, A635 (2005).

22. J. St-Pierre, B. Wetton, G. S. Kim and K. Promislow, *J. Electrochem. Soc.*, **154**, B186 (2007).
23. U. Beuscher, *J. Electrochem. Soc.*, **153**, A1788 (2006).
24. D. R. Baker, D. A. Caulk, K. C. Neyerlin and M. W. Murphy, *J. Electrochem. Soc.*, **156**, B991 (2009).
25. S. Sambandam and V. Ramani, *Phys. Chem. Chem. Phys.*, **12**, 6140 (2010).
26. K. Kudo, T. Suzuki and Y. Morimoto, *ECS Trans.*, **33**, 1495 (2010).
27. F. Xu, H. Y. Zhang, J. Ilavsky, L. Stanciu, D. Ho, M. J. Justice, H. I. Petrache and J. A. Xie, *Langmuir*, **26**, 19199 (2011).
28. J. Xie, D. L. Wood, K. L. More, P. Atanassov and R. L. Borup, *J. Electrochem. Soc.*, **152**, A1011 (2005).
29. S. Zils, M. Timpel, T. Arlt, A. Wolz, I. Manke and C. Roth, *Fuel Cells*, **10**, 966 (2010).
30. C. Ziegler, S. Thiele and R. Zengerle, *J. Power Sources*, **196**, 2094 (2011).
31. C. S. Kuroda and Y. Yamazaki, *ECS Trans.*, **11**, 509 (2007).
32. H. Schulenburg, B. Schwanitz, J. Krbanjevic, N. Linse, R. Mokso, M. Stampanoni, A. Wokaun and G. G. Scherer, *ECS Trans.*, **33**, 1471 (2010).
33. M. Lefevre, E. Proietti, F. Jaouen and J. P. Dodelet, *Science*, **324**, 71 (2009).
34. G. Wu, K. L. More, C. M. Johnston and P. Zelenay, *Science (New York, N.Y.)*, **332**, 443 (2011).
35. T. Suzuki, K. Kudo and Y. Morimoto, *J. Power Sources*, **222**, 379 (2013).
36. T. a. Greszler, D. Caulk and P. Sinha, *J. Electrochem. Soc.*, **159**, F831 (2012).
37. Y. Ono, T. Mashio, S. Takaichi, A. Ohma, H. Kanesaka and K. Shinohara, *ECS Trans.*, **28**, 69 (2010).
38. J. P. Owejan, J. E. Owejan and W. Gu, *J. Electrochem. Soc.*, **160**, F824 (2013).
39. N. Nonoyama, S. Okazaki, A. Z. Weber, Y. Ikogi and T. Yoshida, *J. Electrochem. Soc.*, **158**, B416 (2011).

7 Oxygen Transport Resistance in Thin Nafion Binder Films in the Catalyst Layer

7.1 Introduction

Prior works regarding the local O₂ transport resistance at the Nafion|Pt level have not distinguished whether this resistance is due to O₂ transport into or through the Nafion, or whether it is an electrochemical phenomenon at the Pt surface, since all of these studies featured a Nafion film coating a Pt working electrode.¹⁻⁴ Therefore, the objective of the following work is to identify whether the thin Nafion films on their own, separate from a Pt electrode surface, introduce an interfacial resistance. This chapter presents a new method for simulating the local transport at Pt particle in an ex-situ experimental characterization of Nafion O₂ transport resistance without the presence of the Pt|Nafion interface. As Figure 7.1 illustrates, we achieve this by depositing thin Nafion film onto an inert substrate with widely spaced nano-pores. Here, we have used a track-etched polycarbonate membrane (PCM) that has widely spaced 10 nm pores. The pores are small enough that Nafion chains cannot enter the pores and only forms a film on the surface. In addition, the pores are small enough to mimic the length scales of a single Pt particle.

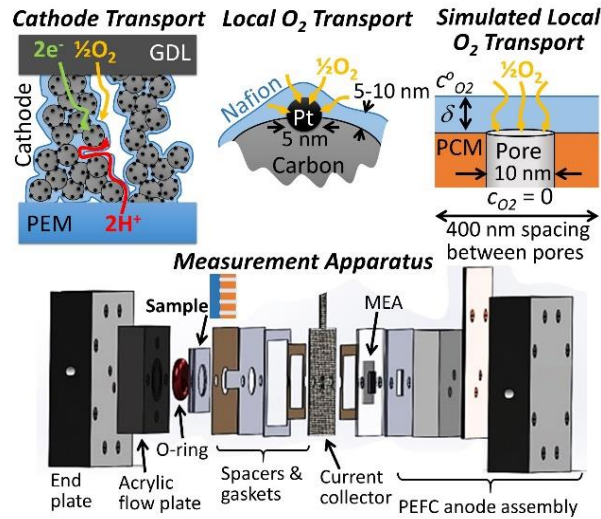


Figure 7.1 The local oxygen transport resistance within PEFC cathodes is simulated by supporting thin Nafion films on a track-etched PCM with widely spaced cylindrical 10 nm pores. The PCM-supported Nafion's oxygen transport resistance is quantified using the limiting current of a modified 1 cm² PEFC.

Similar to Suzuki et al.,¹ the transport resistance is measured by oxygen transport limited current with the apparatus shown in Figure 7.1, with the exception that Nafion film is not in contact with the Pt. The transport resistance R_{O_2} is defined in Chapter 2 using Fick's law of diffusion and an electrical resistor analogy. Whereas in that case, all transport was gas phase, in this work there is the solubility of O₂ from the gas phase into the Nafion film to consider, along with diffusivity through the Nafion. Measuring the solubility separately is not trivial, nor is it of interest in this study. For this reason, many previous researchers have lumped it into the measurement and reported the permeability K , the product of the solubility c_{film} and diffusivity D of a gas into a film. The transport resistance R_{O_2} used in this work can be related to permeability by combining R_{O_2} 's definition in Eq. (2.3), the definition of permeability, and Fick's law of diffusion:

$$R_{O_2} = \frac{c_{O_2,gas} L_{film}}{K} \quad (7.1)$$

where $c_{O_2,gas}$ is the oxygen concentration in the gas phase, and L_{film} is the thickness of the Nafion film.

Although the technique used here measures the series resistance of the PCM and Nafion, the diffusion transport resistance of the PCM is sufficiently low that the measured resistance is dominated by the Nafion. We present two versions of our results. First is the O₂ transport resistance experienced by the pores including the converging, three-dimensional transport to the small areas of the individual pores. In the second version, the resistance is geometrically corrected to the corresponding resistance if the flux was uniform over the area of the Nafion film. This second version is needed to extrapolate any interfacial resistance and to identify any non-geometrical changes in the O₂ transport resistance as the films become thinner.

7.2 Methods

We prepared Nafion thin-films by spin casting Nafion dispersions onto cleaned commercial track etched PCMs with 10 nm diameter pores and a nominal pore density of 6×10^8 pores/cm² (Structure Probe, Inc., West Chester, PA). The Nafion solution consisted of a commercial Nafion dispersions (D 521 and D 2020, Ion Power, Inc., New Castle, DE) that we diluted with varying amounts of a 50/50 vol. mixture of isopropyl alcohol and de-ionized water. Nafion dispersions with loadings of 1, 3, 5, and 20 wt%. Nafion were used to prepare Nafion thin films with a large variation in thickness. Multiple samples were prepared and characterized at each Nafion loading. Additional samples included a Nafion 211 membrane (Ion Power) and an uncoated PCM. The oxygen transport resistance of the thin-film was characterized by the limiting current density using a modified 1 cm² PEFC hardware (see Figure 7.1). The anode side was unchanged from the standard assembly of the endplate, current collector, and graphite flow plate. The fuel cell's membrane electrode assembly (MEA) featured in-house prepared 0.3 mg_{Pt}/cm² gas diffusion electrodes based on SGL 25BC gas diffusion layers (GDLs) (Ion Power) and 40 wt% Pt/C catalyst (Alfa Aesar, Ward Hill, MA). To prevent hydrogen crossover, we prepared the MEA's membrane by hot-pressing four Nafion 115 membranes on top of each other for a total thickness of 0.5 mm. On the cathode side of the PEFC, the cathode graphite flow plate was replaced with the sample holder and an additional current collector for the MEA's cathode. The sample holder assembly consisted of an acrylic plate to distribute air flow over the PCM-supported Nafion film and gaskets around the sample perimeter to force all O₂ consumed by the

cathode to pass through the sample film. The Nafion film was placed on the air inlet side to maintain the Nafion water activity at that of the incoming well-mixed, humidified air.

A fuel cell test stand (850e, Scribner and Associates, Southern Pines, NC) delivered humidified air and hydrogen to the measurement cell at pressures and flow rates of 1 atm and 100 sccm, respectively. Unless otherwise specified, the sample temperature was 80°C and the air's relative humidity was 68%. Higher relative humidities caused condensation between the sample and the MEA that interfered with measurements. A potentiostat was used for the electrochemical characterization (SP-50, Bio-Logic USA, Knoxville, TN). After an initial screening with cyclic voltammetry to identify a repeatable limiting current potential range, we obtained the limiting currents from the time averaged currents for chronoamperometric constant voltage holds at 0.3, 0.25, 0.2, and 0.15 V; this procedure was repeated for each sample.

We measured film thicknesses at each Nafion loading following the electrochemical characterization. We used a Hitachi 7100 transmission electron microscope (TEM) (Hitachi Group, Tokyo, Japan) to measure the film thickness from ultramicrotomed cross-sections of the 1, 3, and 5 wt% samples. The 20 wt% film thickness was measured using nano-scale resolution X-ray radiography in Zernike phase contrast mode (UltraXRM-L200, Xradia, Inc., Pleasanton, CA).

The measured resistance for the 3D transport within the Nafion to the dispersed 10 nm pores was converted to the corresponding transport resistance of uniform, one-dimensional oxygen flux through a film of the same thickness using a geometric correction factor. We determined the correction factor correlation curve by 3D finite element modeling (COMSOL v4.3, COMSOL, Inc., Burlington, MA) of the O₂ transport to a single pore in the center of 408 x 408 nm² area of Nafion film (nominal area per pore) with automated parametric variation in Nafion film thickness. Since the diffusion coefficient is significantly lower in the Nafion domain relative to the pore or air, the correction is purely a geometric factor.

7.3 Results and Discussion

In this work and similar to prior work on oxygen transport in thin-films, we report only the total transport resistance of the Nafion films and membranes rather than the diffusivity

reported in prior characterization of thick Nafion membranes. This is because the calculation of a diffusion coefficient requires an additional characterization of the oxygen solubility in order to resolve the oxygen concentration in the Nafion at the air interface. Fortunately, lumping the solubility and diffusivity together as a total transport resistance does not affect the expected proportional scaling of the resistance with thickness with constant diffusivity, nor does it affect the expectation of zero resistance at the extrapolated limit of zero thickness if there is no additional interfacial resistance.

We performed scanning electron microscope (SEM) imaging of the samples after electrochemical testing to ensure both integrity of the film as well as the specified pore density of the commercial PCM film. Figure 7.2 shows the coated and uncoated sides of the Nafion coated PCM. The film shown is the lowest Nafion solution loading of 1wt%, which yields the thinnest films studied here. We observe complete coverage and some apparent roughness in the film, but low resolution TEM imaging of large sample cross sections show the thickness variation is only on the order of 10's of nm. Any prolonged scanning time resulted in beam damage that exposed the pores of the PCM underneath thin Nafion film. The uncoated image highlights the sparse distribution of the highly aligned, through-hole pores in the PCM. From counting pores in the SEM images, we found the average pore density of three samples to be 6×10^8 pores/cm², matching the supplier's specification. Although, SEM imaging could not verify the small 10 nm pore diameter specification due to charging artifacts and beam damage, they roughly appear on the order of 10 nm.

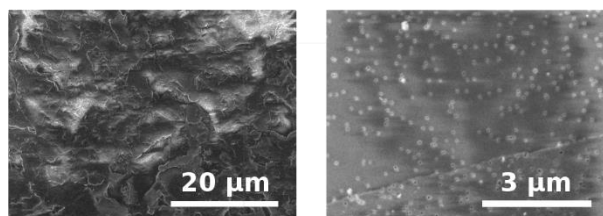


Figure 7.2 SEM images of the 1 wt% Nafion coated (left) and uncoated (right) surfaces of the PCM. The uncoated image shows the sparse distribution of 10 nm through-hole pores.

To verify our measurement accuracy, we measured the oxygen transport resistance of the NR 211 Nafion membrane and the uncoated PCM and compared them to expected value. The O₂

transport resistance R_{O_2} of the films is calculated from the limiting current, I , according to the expression $R_{O_2} = 4c_{O_2}AF / I$, where A is the film area, F is Faraday's constant, and c_{O_2} is the oxygen concentration in the delivered gas. Figure 7.3a shows the transport resistances of these membranes. Our NR 211 measurement shows good agreement with prior literature values given the significant variance among those values,⁵⁻⁸ where reported values have been converted to the corresponding resistance quantity (R_{O_2}) reported here. The measured transport resistance of 8.5×10^3 s/m for the uncoated PCM is shown in Figure 7.3b and agrees well with the theoretical resistance of 8.4×10^3 s/m for Knudsen diffusion through the 10 nm pores. The theoretical value for the bare PCM, based on Knudsen diffusion, is given by the equation $R_{O_2} = \tau L / \left(\varepsilon d_{pore} \sqrt{8RT / 9\pi M_{O_2}} \right)$, where ε is the porosity with a value of 0.047% based on pore density, τ is the estimated tortuosity of 1.07 based on a typical 15° angle off of normal for PCM pores, L is the PCM thickness, R is the universal gas constant, T is the temperature, and M_{O_2} is the molecular mass of oxygen. Thus, it is clear that the high diffusion coefficient in the GDL of the PEFC MEA and the cathode's high Pt roughness factor ($>100 \text{ cm}_{Pt}^2/\text{cm}_{film}^2$) mean that the MEA's transport resistance is negligible compared to that of the PCM, and the PCM's R_{O_2} is in turn is negligible compared to the Nafion films to be measured. The ratio of the cathode Pt surface area to the film measured is on the order of 200, so the impact of a 5-10 nm Nafion film on the MEA's catalyst is negligible.

Figure 7.4 shows example images from the nano-CT (Figure 7.4a) and TEM (Figure 7.4c) thickness characterizations of the Nafion films being studied. The nominal thicknesses of the Nafion films at the 1, 3, 5, and 20 wt% solutions were 50 nm, 200 nm, 500 nm, and 2 μm , respectively. Thus, the thinnest layer is well within the range of thicknesses that Page et al. observe significant confinement effects in Nafion thin-films.⁹ Figure 7.3 shows the uncorrected transport resistance R_{O_2} of the Nafion coated PCM films as a function of thickness, as well as the corrected resistance, which will be discussed later. The horizontal error bars illustrate the uncertainty in the thickness and vertical error bars show the standard deviation of multiple resistance measurements for multiple samples at each thickness. Compared to the corrected data, the uncorrected plots presents a higher resistance because of the concentrated flux at each of the 10 nm pores. The uncorrected data can be converted to an equivalent active site (i.e., pore) area

value by multiplying the uncorrected R_{O_2} values by the PCM porosity, yielding values of 9.5, 13, 27, and 45 s/m, respectively for the four thicknesses given above. For comparison, the transport resistance of the ~ 400 μm thick fibrous GDL is on the order of 0.1 s/m.

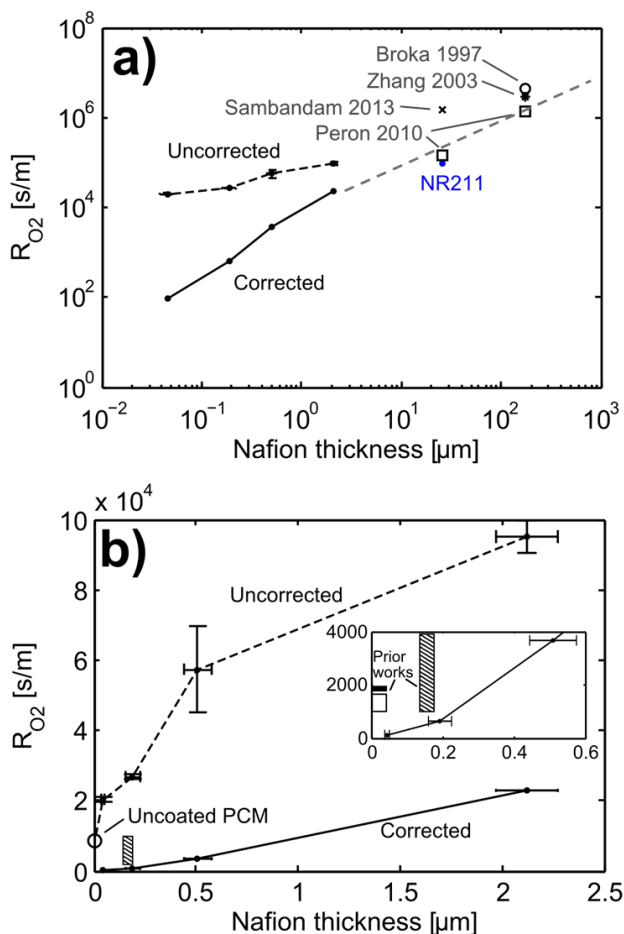


Figure 7.3 a) Log-log plot oxygen transport resistance of the Nafion coated PCM and Nafion membranes⁵⁻⁸ (NR211 from present study) as function of thickness. The corrected curve (solid) are the values when resistance is corrected for uniform 1D flux through a film of the same thickness using the correction factors in Figure 7.4e. The grey dashed line indicates a slope of 1 for expected proportionality between resistance and thickness. b) Linear plot of the same uncorrected and corrected oxygen transport resistance values, including the uncoated PCM and an inset near the zero-thickness intercept. The range of interfacial resistance estimation from prior work is shown at thicknesses they were estimated from in experiments; Suzuki et al.¹ (hatch fill), Ono et al.¹⁰ (black fill), Greszler et al.¹¹ (white fill).

The first goal of this work was to determine if there is a significant interfacial resistance to oxygen transport through Nafion films in addition to the diffusion across the film. A second

goal was to determine whether the Nafion films exhibit thickness dependent transport properties. To achieve these goals, our analysis has to eliminate the role of the 3D diffusion path through the Nafion from the air to the pore that will artificially increase resistance with thinner films. Figure 7.4 shows the results of the 3D FEM simulation of oxygen transport to a single pore that are used to compute a correction factor for uniform 1D transport. For the 2 μm film result in Figure 7.4b, the concentration contours show flux crowding at the 10 nm pore and a transition to the uniform 1D transport through the thickness. For the 200 nm case shown in Figure 7.4d, the O_2 contours show that the flux through the entire film thickness is concentrated over the area of the pore, increasing the effective transport resistance. The correction factor plotted in Figure 7.4e is calculated by the ratio of the effective diffusivity to the bulk diffusivity, $K_{geom} = D_{eff} / D$, where D_{eff} is calculated from the area-averaged flux at the air interface, thickness, and concentration difference $D_{eff} = \dot{n}_{\text{O}_2} L / \Delta c_{\text{O}_2}$. Toward the limit of zero thickness, the correction approaches the PCM pore volume fraction of 4×10^{-4} , whereas correction slowly approaches unity with increasing thickness as the resistance of the bulk diffusion outweighs the effective contact resistance of the PCM interface. The correction is significant even for 40 μm thick Nafion films.

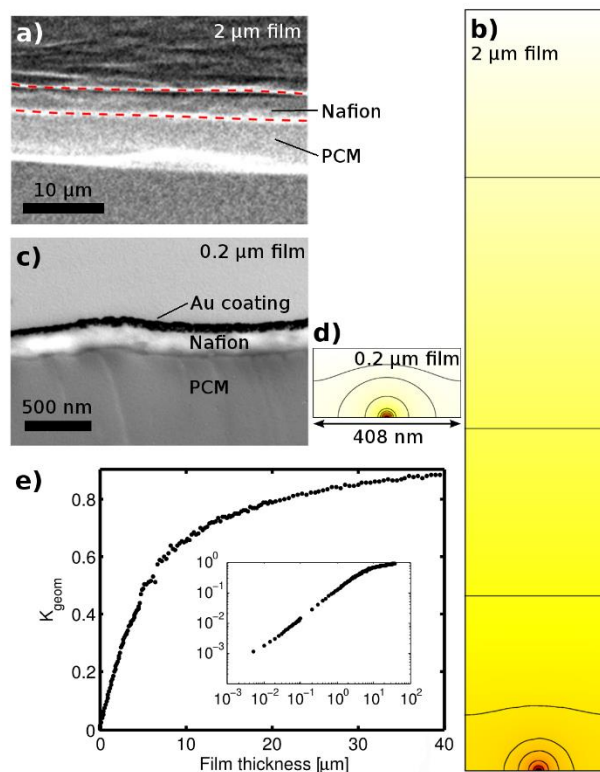


Figure 7.4 a) X-ray radiography characterization of the 20 wt% Nafion film thickness. Red dashed lines show Nafion interfaces from the Zernike phase contrast image. b) Simulation of O_2 diffusion in the 2 μm film from the 20 wt% Nafion coating. c) TEM measurement of the 3 wt% Nafion film thickness. d) Simulation of O_2 diffusion in the 0.2 μm film from the 20 wt% Nafion coating. e) Correction factors for converting measured resistance to the corresponding value for uniform 1D flux based on a parametric computational study of O_2 diffusion through films of varying thickness.

In addition to the directly measured, uncorrected R_{O_2} values, Figure 7.3 also shows the oxygen transport resistance when corrected for each thickness using the K_{geom} factors from Figure 7.4e. The corrected R_{O_2} values are lower and exhibit a more linear trend with a negligible non-zero resistance y-intercept. The gray dashed line in Figure 7.3a's log-log plot shows a slope of unity for ideal thickness scaling with constant diffusivity, which aligns well with the Nafion coated PCM and the membrane measurements of this work and prior work. This shows that our measurements are consistent with prior work, and also demonstrates that we don't observe a significant thickness dependence for the Nafion's oxygen diffusivity.

The negligible non-zero resistance intercept when extrapolating the corrected data to zero thickness in Figure 7.3b shows that there is no observable interfacial resistance over the range of thicknesses we have characterized. Any additional interfacial resistance that prior work suggests would have been observable as a significant non-zero y-intercept in Figure 7.3b's inset. In addition, the slight positive curvature of the corrected R_{O_2} data in Figure 7.3a indicates a slightly reduced diffusivity within thinner films, if any change at all. The curvature is minor enough that we do not conclude that there is a significant thickness effect – only that there is no y-intercept, and that the slight positive curvature supports this conclusion even further. Thus, the Nafion films we characterized here would not introduce the additional local resistance reported in the prior work. For comparison, Figure 7.3b shows the range of the reported additional Nafion interfacial resistance reported by Suzuki et al.,¹ Greszler et al.,¹¹ and Ono et al.¹⁰ in the vertical bars. The horizontal axis position of those bars indicates approximately the thinnest film evaluated in those studies. The ex-situ work of Suzuki et al. showed a large range for their estimate; however, the lower bound of their interfacial O_2 transport resistance is notably larger than our measured resistance at 200 nm. Recall, their work evaluated the resistance for a Nafion film deposited on the surface of a Pt working electrode. The other two estimates are from in-operando characterizations of operating PEFCs with 5-10 nm Nafion films coated on carbon-supported Pt catalyst. In contrast, this work measured R_{O_2} in Nafion films that were *not* in direct contact with a Pt working electrode, and no additional resistance was observed.

We now discuss the origin of the additional local oxygen resistance reported in the prior work in light of the present findings. In the prior work, we observe that the lower bound of Suzuki et al.'s¹ ex-situ measurements agrees well with the in-operando measurements of Greszler et al.¹¹ and Ono et al.¹⁰ The origin of the wide range of Suzuki et al. data is unknown. The Suzuki et al. films were spin coated, as were the samples herein, so it is not evident that the spin coating is the origin of our distinct result. One could question whether the additional resistance of the in-operando films is due to significant Nafion structural changes in thinner 5-10 nm films. However, the agreement of Suzuki et al.'s ex-situ lower bound with the in-operando results plus the fact that they measured that resistance and higher values using linear fits from thicker films (165 nm - 800 nm), suggests that their additional resistance does not originate from

a property change with thinner films. This is consistent with our film thickness range of 50-2000 nm, given the roughly proportional relationship between the film thickness and the oxygen transport resistance.

Based on the discussion above, the most significant difference between the prior ex-situ and in-operando characterizations of an additional Nafion interfacial resistance and our current findings of no additional resistance is the presence of a Pt|Nafion interface in the prior work. Greszler et al.'s mathematical analysis indicated the additional local transport resistance observed in the experiments could also manifest from a slow, first order chemical adsorption step in the oxygen reduction reaction. However, it is not clear from the prior or present work if the additional resistance is related to an adsorption mechanism or an additional, unknown transport resistance that evolves at the Pt|Nafion interface. Thus, the key conclusions from this work is that when there is no Pt|Nafion interface, there is no additional interfacial O₂ transport resistance in Nafion films as thin as 50 nm, and the diffusion coefficient in these thin films does not significantly depart from that of bulk Nafion.

7.4 Summary

By supporting thin PFSA films on inert, nano-porous supports, we have measured the oxygen transport resistance of films mimicking those present in PEFC cathodes. Our parametric study of the O₂ transport resistance as a function of film thickness showed no indication of an interfacial resistance. The observed resistance was roughly proportional to thickness, indicating no significant changes in the O₂ diffusion coefficient at thicknesses as thin as 50 nm. This result differs significantly from characterizations of O₂ transport in thin-films with polarized Pt interfaces, which have shown significant interfacial resistances. This contrast suggests that an electrochemical effect, such as an interaction between the ionomer's acid site and the polarized catalyst, may play a significant role in this apparent interfacial resistance.

7.5 References for Chapter 7

1. T. Suzuki, K. Kudo and Y. Morimoto, *J. Power Sources*, **222**, 379 (2013).
2. T. a. Greszler, D. Caulk and P. Sinha, *J. Electrochem. Soc.*, **159**, F831 (2012).

3. J. P. Owejan, J. E. Owejan and W. Gu, *J. Electrochem. Soc.*, **160**, F824 (2013).
4. Y. Ono, T. Mashio, S. Takaichi, A. Ohma, H. Kanesaka and K. Shinohara, *ECS Trans.*, **28**, 69 (2010).
5. K. Broka and P. Ekdunge, *Journal of Applied Electrochemistry*, **27**, 117 (1997).
6. J. Peron, A. Mani, X. Zhao, D. Edwards, M. Adachi, T. Soboleva, Z. Shi, Z. Xie, T. Navessin and S. Holdcroft, *Journal of Membrane Science*, **356**, 44 (2010).
7. L. Zhang, C. S. Ma and S. Mukerjee, *Electrochimica Acta*, **48**, 1845 (2003).
8. S. Sambandam, J. Parrondo and V. Ramani, *Physical Chemistry Chemical Physics*, **15**, 14994 (2013).
9. K. A. Page, A. Kusoglu, C. M. Stafford, S. Kim, R. J. Kline and A. Z. Weber, *Nano Letters*, **14**, 2299 (2014).

8 Modelling Through-Plane Oxygen Transport's Effect on PEFC Performance

8.1 Introduction

In this chapter, we build a simplified zero-dimensional performance model of a polymer electrolyte fuel cell (PEFC) cathode that draws upon the results from earlier chapters – specifically, the measurement of the oxygen transport resistance R_{O_2} in the diffusion medium (DM) and the catalyst layer (CL), the agglomerate size distribution measured by nano-CT and the associated modification to the agglomerate model, and the measurement of the local oxygen transport resistance, $R_{O_2,local}$, at the ionomer/Pt level. By comparing an experimentally obtained polarization curve with the outcome of this model using varying values of $R_{O_2,local}$, we go on to make a rough estimation of the value of $R_{O_2,local}$ and compare it to recent literature values.

The polarization curve we will compare the model to is the 62% RH polarization curve from Figure 2.4, which we chose because the 62% RH case did not show evidence of any liquid water during the c_{O_2} measurements. As further evidence that the 62% RH case did not have condensation of liquid water, we measured the Ohmic resistance of the PEFCs in the experiments of Chapter X – the resistance in the 62% RH case changed significantly at different cell current densities and did not reach a steady value, indicating that the water being generated was in the gas phase, as it did not cease changing in activity as more was produced. In contrast, the resistance of the 91% RH cell changed comparatively little over its range of cell current, which is consistent with the presence of liquid water in the cell and a constant 100% RH environment within the CL.

8.2 Model Framework

This model is based on the agglomerate approach to modelling, and the modification thereto using a distribution of agglomerate sizes, discussed in detail in Chapter 6. This model assumes negligible polarization in the anode, as anode polarization is typically minor compared to cathode polarization, especially in the high-current, mass-transport-limited regions in focus here. In this work, we model PEFC performance without any voltage loss from Ohmic resistance, calculating the so-called “IR-free” cell voltage, $V_{IR-free}$. We compare the IR-free

model results to the IR-free experimental polarization curve, where in the latter case the experimental Ohmic voltage loss was calculated using the current interrupt function of the PEFC test equipment used in that work, and subsequently compensated for in the polarization curve. As a result, we also ignore a number of effects, such as water transport in the polymer electrolyte membrane, that primarily affect the Ohmic behavior of the cell. This model is single phase in that we assume no liquid water is present in the pores of the CL or DM (which is consistent with the experimental results we use for comparison). The model is also “zero-dimensional” in that we do not model the variation of performance through space in any dimension. Instead, we treat gas-phase transport of oxygen as one lumped process, and assume that the gas phase of the agglomerate-filled CL exists as a single interface at a point past all of the O₂ transport resistors, as illustrated in Figure 8.1, which is a simplified version of Figure 1.3. Hence according to Fick’s law of diffusion using an electrical resistor analogy, the gas phase O₂ concentration in the CL is

$$c_{CL} = c_{ch} - \dot{n}_{O_2} R_{O_2} \quad (8.1)$$

where c_{ch} is the O₂ concentration in the channel, \dot{n}_{O_2} is the flux of O₂ to the CL (related to the PEFC current i_{cell} by Faraday’s law of electrolysis: $\dot{n}_{O_2} = i_{cell} / 4F$), and R_{O_2} is the total gas-phase O₂ transport resistance between the channel and the CL. The electrical resistor analogy used to define R_{O_2} was discussed in Chapter 2; the analogy is similar to Darcy’s law, only for diffusive gas flux instead of viscous flow. In this case, as the experimental polarization curve for comparison was collected using a differential cell configuration (i.e. no along-the-channel variation), we take c_{ch} as the concentration of oxygen in the inlet gas, which was air at 60°C and 62% RH. The total transport resistance in the gas phase is the sum of the gas phase O₂ resistance of the DM and the CL:

$$R_{O_2} = R_{O_2,DM} + R_{O_2,CL} \quad (8.2)$$

The value for $R_{O_2,DM}$ in a dry, un-flooded 10BC DM is taken as 65 s/m from the measurements in Chapter 2 of this dissertation. Note that in reality, the effective DM resistance is slightly higher due to the geometric effect of the lands (or ribs) between the flow channels,¹ but that effect is not considered in this work. We calculate $R_{O_2,CL}$ using the definition of $R_{O_2,CL}$ together with the definition of the formation factor K_{form} (defined in Chapter 2) and Fick’s law of diffusion:

$$R_{O_2,CL} = \frac{L_{CL}}{K_{form,CL} D_{O_2/N_2}} \quad (8.3)$$

using the K_{form} value of 0.15 obtained using Chapter 5's nano-CT results in a related work not included in this dissertation,² using a binary diffusivity D_{O_2/N_2} of 2.52×10^{-5} m²/s (corrected for temperature as per Litster et al.²), and an estimated CL thickness of 10 μm, resulting in 2.7 s/m for $R_{O_2,CL}$. Due to the low RH in this study, it is likely that the reaction is proton-limited and hence concentrated at the CL/membrane interface.³ Therefore, it may be a reasonable assumption that $R_{O_2,CL}$ can be simplified to diffusion through mostly the entire thickness of the CL. In reality, of course, oxygen is to some extent consumed throughout the thickness of the CL, and the effect of $R_{O_2,CL}$ is not so simple, as we studied in Chapter 4. Assuming that the oxygen must diffuse through the entire thickness of the CL can be viewed as a “worst case” scenario for single-phase transport. Nevertheless, the simplification to a single scalar value of $R_{O_2,CL}$ through which all O₂ flux must pass is reasonable in practice here because even this “worst-case” $R_{O_2,CL}$ value is much smaller than $R_{O_2,DM}$. Including $R_{O_2,CL}$ in the analysis has little impact on the results of the model. Considering that $R_{O_2,CL}$ has little impact, using the alternate literature value from Yu and Carter⁴ ($K_{form} = 0.09$, $R_{O_2,CL} = 4.5$ s/m) also changes the results very little. Despite the minor effect, for completeness, we include the effect of $R_{O_2,CL} = 2.7$ s/m taken from the microstructural work in this dissertation.²

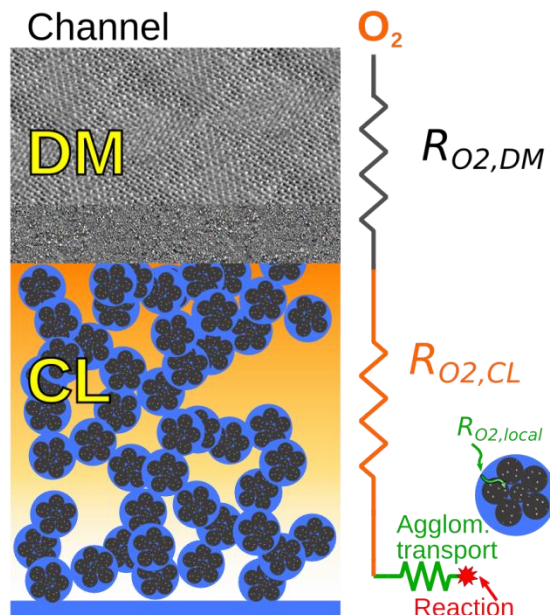


Figure 8.1 Schematic depiction of the treatment of single-phase oxygen transport resistance in this model.

After finding the gas-phase O_2 concentration in the CL using Equation (8.1), we solve for the cell's current density using Equations (6.7) and (6.18), the terms of which are explained in that chapter. The values for the agglomerate size distribution and their manner of implementation were taken from the same chapter (Chapter 6). The local “interfacial” O_2 mass transfer coefficient k_{local} (as defined in Chapter 6), can also be defined as the inverse of $R_{O_2,local}$ as described in Chapter 7. In that chapter, we did not observe any additional $R_{O_2,local}$ in a Nafion film that was independent of a Pt/Nafion interface. We did, however, observe that even in Nafion films on the order of 10 nm thick, $D_{O_2,Nafion}$ was consistent with literature values for bulk Nafion. Therefore, for bulk Nafion diffusion $D_{O_2,Naf}$ in this model, we use a value of 4.5×10^{-10} m²/s from literature (interpolated between $D_{O_2,Naf}$ at two RH values to match the RH in this work).⁵ For the local resistance, we consider a range of possible values of k_{local} : from 2.1×10^{-3} m/s to 5×10^{-4} m/s, which are calculated from the lower⁶ and upper⁷ limits of literature $R_{O_2,local}$ values in Chapter 7 (not counting the unusually high values from Suzuki et al.⁸). We also consider a k_{local} value of unity, which is equivalent to no additional local resistance at all.

The model was calculated and plotted for values of $V_{IR-free} \leq 0.8$ V; the kinetic, higher-voltage (or, lower-overpotential) region was not of interest here, and moreover this model makes

several well-established simplifications by assuming high (> 0.4 V) overpotential, e.g. using a single value for the cathodic transfer coefficient α_c . These and other parameters used in this model are summarized in Table 8.1. The ratio of the reference exchange current density to its reference O_2 concentration, $i_{0,ref}/c_{O_2,ref}$ was fitted at the point where $V_{IR-free} = 0.84$ V in the experimental polarization curve. Other than this, the only other fitted parameter was the additional local O_2 mass transfer coefficient k_{local} as defined in Chapter 6. This value was varied from its low to its high value until the best fit qualitative emerged, which provides a rough estimate of k_{local} from this experimental polarization curve.

Table 8.1: Table of parameters used in model.

Term	Value	Source
T (cell temperature)	60 °C	To match experiments in Chapter 2
c_{ch} (channel O_2 concentration)	6.77 mol m ⁻³	To match conditions in Chapter 2, accounting for water vapor at 62% RH
H (Henry's constant, O_2)	0.347 atm m ³ mol ⁻¹	Literature + temperature correction ⁹
$D_{O_2,Naf}$ (O_2 diffusivity in bulk Nafion)	4.5x10 ⁻¹⁰ m ² s ⁻¹	Interpolated from literature for RH ¹⁰
δ (Nafion film thickness)	10 nm	Chapter 6
ε_{CL} (CL porosity)	0.43	Chapter 5
L_{CL} (CL thickness)	10 μ m	Assumed
α_{ca} (Cathode transfer coeff.)	0.55	Literature ¹¹
$i_{0,ref}/c_{O_2,ref}$ (Exchange current density to O_2 concentration ratio)	1.8x10 ⁻⁵ A mol ⁻¹	Fitted in this work
$R_{O_2,DM}$ (Single-phase O_2 transport resistance through DM)	65 s/m	Measured in Chapter 2
$R_{O_2,CL}$ (Single-phase O_2 transport resistance through CL pores)	2.7 s/m	Equation (8.3) and nano-CT analysis ²
k_{local} (local O_2 mass transfer coeff.)	Low: 2.1x10 ⁻³ m s ⁻¹ High: 5x10 ⁻⁴ m s ⁻¹ None: 1 m s ⁻¹	Lower and upper ranges of literature values ^{6,7,12}

Using the framework described above, we mapped out the cathode overpotential η as a function of PEFC current density i_{cell} , with some iteration required as i_{cell} is a function of both η and c_{CL} , and c_{CL} is in turn a function of i_{cell} . We then computed the IR-free PEFC voltage $V_{IR-free}$ according to:

$$V_{IR-free} = V_{rev} - \eta \quad (8.4)$$

where V_{rev} , the thermodynamic reversible voltage for the reaction, is given by the Nernst equation:

$$V_{rev} = \frac{\Delta G^o}{2F} + \frac{(T - T^o)\Delta S^o}{2F} + \frac{RT}{2F} \ln \left(\frac{p_{H_2} p_{O_2}^{0.5}}{p_{H_2O}} \right) \quad (8.5)$$

In Equation (8.5), ΔG^o and ΔS^o are the Gibb's free energy and entropy for the reaction at the reference state at temperature and pressure T^o and p^o , F and R are Faraday's constant and the universal gas constant, and p_i is the partial pressure of each species i divided by p^o . Finally, to further explore the effects of mass transport voltage losses, we calculated a mass transport free version of the model's polarization curve, using the same method outlined above but assuming that c_{CL} is equal to c_{ch} at all values of i_{cell} , and that k_{local} is unity and has no effect.

8.3 Results and Discussion

The results of the model are summarized in the IR-free polarization curves in Figure 8.2. The model polarization curve with no local O_2 resistance ($k_{local} = 1$ m/s) correctly shows a limiting current consistent with the roughly 68 s/m O_2 transport resistance measured in this dissertation and implemented in this model. Its mass transport free version can be viewed as the polarization curve plotted from activation/kinetic voltage losses only. The most noteworthy feature of Figure 8.2 is that the model results for the upper and lower limits of k_{local} from the literature, given in Table 8.1, fall above and below the experimental polarization curve, indicating that the actual value of k_{local} in this experiment's electrode falls within the literature's expected range.

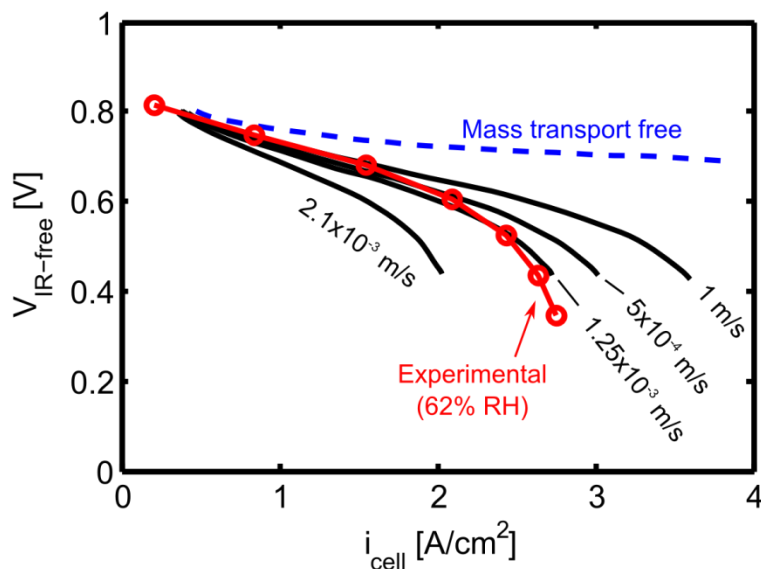


Figure 8.2 Experimental and model-generated IR-free polarization curves, with model curves for various values of the local O_2 transport resistance k_{local} (noted by each curve), ranging from the lower to upper limits of $R_{O_2,local}$ in the literature, and including the “best match” value of $k_{local} = 1.25 \times 10^{-3}$ m/s. Also depicted are the model results with no k_{local} effect, and with no mass transport effects.

We tuned k_{local} until a qualitatively good fit was found between model and experiment, and plotted that result in Figure 8.2 as well. The “best match” value of k_{local} was 1.25×10^{-3} m/s, which corresponds to a value of 800 s/m for $R_{O_2,local}$. This compares well to the range of values calculated in the literature for this effect – Owejan et al.⁶ found a $R_{O_2,local}$ value of roughly 480 s/m, Greszler et al.¹² found 1000 – 1700 s/m, and Ono et al. found values from 1800 to 2000 s/m. It is worth noting that in an *ex-situ* study, Suzuki et al.⁸ found much higher values, ranging from 1700 – 10^4 s/m. Considering the three other studies’ values, we are inclined toward the lower end of the range from the work by Suzuki et al, which still compares reasonably with the k_{local} value fitted in this work.

To further examine the individual contributions of each separate barrier to mass transport, we determined the voltage loss due to each mechanism of oxygen transport resistance, presented in Figure 8.3. This was done by removing one source of O_2 transport resistance, calculating the model polarization curve, and subtracting the resulting $V_{IR-free}$ from the original version with all O_2 resistance mechanisms in place. We did this cumulatively, i.e. we removed the first

resistance, then the first and the second resistance, etc. The final $\Delta V_{O_2 transp}$ curve in Figure 8.3 that represents all mass transport voltage losses at all (blue dotted curve) is equivalent to subtracting the “best-match” ($k_{local} = 1.25 \times 10^{-3}$ m/s) model curve in Figure 8.2 from the mass-transport-free curve in the same figure.

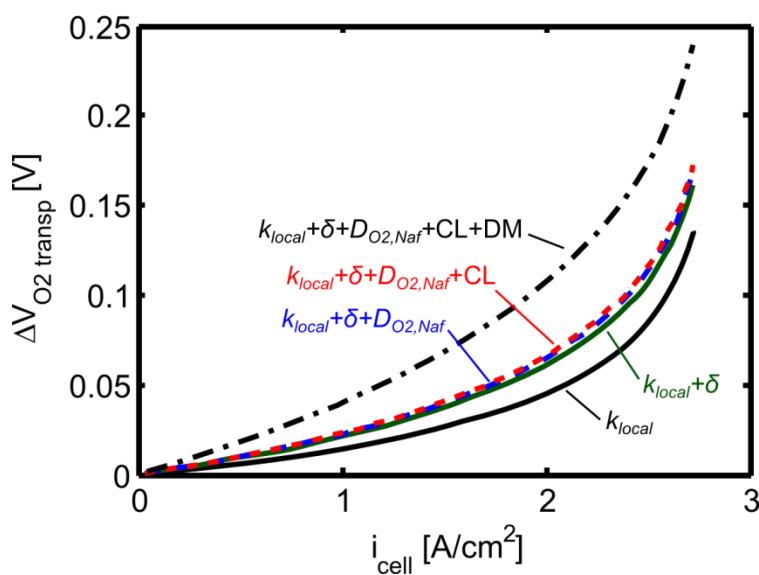


Figure 8.3 Voltage losses arising from different mechanisms of oxygen transport resistance, namely (from the bottom): the local ionomer/Pt resistance, the Nafion film covering agglomerates, Nafion diffusion within the agglomerate interior, CL pores, and DM pores. Curves are cumulative with respect to the mechanisms of transport resistance.

The first resistance we removed was the effect of k_{local} . This was one of the most significant sources of $\Delta V_{O_2 transp}$, showing that the local Pt|ionomer resistance is one of the most significant barriers to oxygen transport in this cell. Removing the impact of diffusion through Nafion film of thickness δ (by setting δ to 0.1 nm, 1/100th its original thickness) also had a significant (though smaller) effect. In other words, diffusion through this Nafion film covering the agglomerate is a substantial barrier to oxygen transport. Next, setting $D_{O_2,Naf}$ to a very high value to remove the contribution of diffusion inside of the active portion of the agglomerate had little effect. Gas-phase diffusion in the CL pores ($R_{O_2,CL}$) was the next barrier removed, which also had little effect. Finally, the diffusive resistance through the pores of the DM ($R_{O_2,DM}$) was removed, which had a large impact, roughly commensurate with that of k_{local} . To summarize what Figure 8.3 illustrates, the local Pt|ionomer resistance and the DM pores are the most

significant sources of mass transport voltage loss in this cell, with each contributing roughly equally, followed by bulk diffusion through the Nafion film surrounding the agglomerates. It is noteworthy that the local resistance contributes more to mass transport voltage loss than diffusion through the Nafion film and the agglomerate does – in other words, it is the largest Nafion-related oxygen resistance by far. This agrees with comments by Nonoyama et al.¹³ that $R_{O_2,local}$ is equivalent to tens of nanometers of Nafion film (while the actual thickness δ is only about 10 nm or less), as well as other works regarding the significance of $R_{O_2,local}$.^{6,8,12} Note that despite $R_{O_2,local}$ having a higher nominal value than $R_{O_2,DM}$ (800 s/m compared to 65 s/m), $R_{O_2,local}$ exists many times in parallel, or in other words, across a larger area according to the CL's Pt roughness factor, whereas $R_{O_2,DM}$ exists only once and all oxygen flux must pass through it. This is why $R_{O_2,DM}$ is still an equally significant resistance despite its seemingly lower value. We also note here that these resistances do not superimpose onto each other quite so simply in execution. If we performed this cumulative study of mass transport voltage loss by removing the sources in a different order, the results differed slightly. However, the conclusion of this study remained the same regardless of what order the resistances were removed: the most significant resistances are the DM pores and $R_{O_2,local}$, followed in third place by diffusion through the Nafion film of thickness δ that surrounds the agglomerate.

8.4 Summary

We performed a simplified 0-D, single-phase agglomerate model of PEFC performance, using results from throughout this dissertation. We employed the agglomerate size distribution and its implementation as described in Chapters 5 & 6; the oxygen transport resistance R_{O_2} through the DM and the CL derived from Chapters 2 and 5, respectively; the finding from Chapter 7 that oxygen diffusivity through Nafion is equivalent to the bulk value, and the knowledge from literature that there exists an additional $R_{O_2,local}$ at the Pt/Nafion level. After computing the model for multiple values of $R_{O_2,local}$ from the range in the literature, we found that the experimental results matched with $R_{O_2,local}$ value from within that range, and extracted an estimated $R_{O_2,local}$ for this electrode of 800 s/m (or its inverse, k_{local} , of 1.25×10^{-3} m/s). We find that the DM and the local Pt|Nafion resistance $R_{O_2,local}$ are the two largest sources of voltage losses due to oxygen transport in this PEFC.

8.5 References for Chapter 8

1. A. Z. Weber, *Electrochim. Acta*, **54**, 311–315 (2008).
2. S. Litster, W. K. Epting, E. A. Wargo, S. R. Kalidindi, and E. C. Kumbur, *Fuel Cells*, **13**, 935–945 (2013).
3. K. C. Hess, W. K. Epting, and S. Litster, *Anal. Chem.*, **83**, 9492–9498 (2011).
4. Z. Yu and R. N. Carter, *J. Power Sources*, **195**, 1079–1084 (2010).
5. S. Sambandam and V. Ramani, *ECS Trans.*, **25**, 433–441 (2009).
6. J. P. Owejan, J. E. Owejan, and W. Gu, *J. Electrochem. Soc.*, **160**, F824–F833 (2013).
7. Y. Ono et al., *ECS Trans.*, **28**, 69–78 (2010).
8. T. Suzuki, K. Kudo, and Y. Morimoto, *J. Power Sources*, **222**, 379–389 (2013).
9. D. Harvey, J. G. Pharoah, and K. Karan, *J. Power Sources*, **179**, 209–219 (2008).
10. S. Sambandam, J. Parrondo, and V. Ramani, *Phys. Chem. Chem. Phys.*, **15**, 14994–5002 (2013).
11. A. Parthasarathy, S. Srinivasan, a. J. Appleby, and C. R. Martin, **139**, 2530–2537 (1992).
12. T. a. Greszler, D. Caulk, and P. Sinha, *J. Electrochem. Soc.*, **159**, F831–F840 (2012).
13. N. Nonoyama, S. Okazaki, A. Z. Weber, Y. Ikogi, and T. Yoshida, *J. Electrochem. Soc.*, **158**, B416 (2011).

9 Resolving Heterogeneous 3D Microstructures in Commercial Solid Oxide Fuel Cells using Nanoscale X-ray Computed Tomography

9.1 Introduction

Anode-supported SOFCs,¹ such as those studied in this chapter, are typically comprised of 5 distinct layers: 1) a thick, porous, electron-conducting anode support layer that acts as a physical support for the rest of the cell; 2) a porous, composite anode active layer (AAL); 3) a dense YSZ electrolyte/separator layer; 4) a porous, composite cathode active layer (CAL); and 5) a porous, electron-conducting cathode current collector layer. The active layers will be the focus of this chapter. Oxygen is reduced at the CAL, and hydrogen (which may be internally reformed from methane and other fuels) is oxidized at the AAL. The CAL is typically composed of an ion-conducting phase (ICP) like YSZ, and an electron-conducting phase (ECP) such as lanthanum strontium manganite (LSM) or lanthanum strontium cobalt ferrite (LSCF). Similarly, the AAL uses an ICP such as YSZ, and an ECP, typically nickel.

In the active layers, reaction can only occur where the gas-carrying pores, the ECP, and the ICP all come together – these locations are known as triple-phase boundaries (TPBs). A high density of TPBs is important for a high reaction rate, as are the transport of ions, electrons, and gas to the TPB locations in the microstructure. Degradation in SOFC electrodes is also tied to overpotential,² which will depend in part on microstructure for a given reaction rate. For these reasons, a major research thrust in the SOFC field has been to understand the impact of microstructure on cell performance and degradation. A number of previous works have studied the 3D SOFC microstructure using focused ion beam sectioning combined with scanning electron microscopy (FIB-SEM)^{3–16} or various forms of nanoscale X-ray computed tomography (nano-CT).^{15,17–27} While many of these studies analyzed the microstructure to extract morphological parameters related to performance and durability, some works have compared the 3D microstructure imaged directly to experimental cell performance metrics^{4,5,7–12,23,24} or used the microstructural data to model cell performance.^{5,10,12,19,26}

Academic studies of SOFC microstructure have generally focused on cells made in-house, using controlled methods and yielding a fairly uniform microstructure. These studies have

yielded significant advances in basic understanding of the relationship between SOFC microstructure and performance. Most of these works have imaged volumes in the neighborhood of 5-10 μm on a side, though some have imaged volumes in the larger (15-25 μm)³ range.^{11,12,21-23} To our knowledge, few works have directly studied the question of how much volume is needed to adequately represent the overall microstructure and generate representative statistics. Notable exceptions are the works of Laurencin et al,^{21,22} who determined the representative volume of the anode support layer to be (35 μm)³ and of the AAL to be (13 μm)³; the works of Joos et al,^{13,28} who found that roughly (6 μm)³ was sufficient to represent their research-grade CAL; and Harris and Chiu,²⁷ who established a theoretical framework, applied it to experimental results on a research-grade material that was not SOFC but was made of similar materials with SOFCs in mind, and predicted RVEs on the order of (5-10 μm)³ for those materials.

The question of representativeness of imaged volume becomes even more relevant when one considers different methods of cell manufacture, which may yield more or less homogeneous electrode structures. There are two possible types of heterogeneity discussed in this work – high- and medium-frequency heterogeneity, such as local variation in phase fraction; and low-frequency, anomalous heterogeneity, such as particularly large particles of one solid material or particularly large pores. Any SOFC electrode will contain some amount of low/medium frequency heterogeneity, though the extent may differ. On the other hand, as we will show in this work, mass-produced, commercial SOFC electrodes can contain large, low-frequency heterogeneities whereas small-batch, lab-generated SOFCs in the literature generally do not appear to.

In this chapter, we use X-ray computed tomography (CT) to characterize the 3D microstructure of the CAL and AAL of a commercial, mass-produced SOFC. We employ two different methods of x-ray CT to study two different length scales – microscale (micro-CT) and nanoscale (nano-CT). We then discuss the level of heterogeneity evident in the microstructures of the different electrodes, with the aim of determining what volume is appropriate to study microstructure in commercial, mass-produced SOFCs, as opposed to research-grade SOFCs.

9.2 Experimental

This study concerns the CAL and AAL from an anode-supported, mass-produced SOFCs from a commercial supplier (Materials and Systems Research, Inc, Salt Lake City, UT). For the CAL, the ICP of this electrode is YSZ; the ECP is LSM. For the AAL, the ICP is YSZ, and the ECP is nickel. Additional details about the composition and fabrication are not available due to the proprietary nature of the commercial sample.

9.2.1 Synchrotron Micro-CT

For longer length scale analysis, we used a synchrotron-based micro-CT at the Advanced Photon Source (APS, Argonne, IL) with 1 μm resolution and a 1 x 1 mm field-of-view. A piece of the entire anode-supported SOFC was cut to a square of approximately 0.5 x 0.5 mm with a jeweler's saw outfitted with a 0.2 mm diameter diamond wire (DMT Inc, Colorado Springs, CO), and the sample was attached to a pin with epoxy, with the cathode side facing away from the epoxy. Radiographs were collected at the APS beam line 1-ID using monochromatic, 50 keV x-rays in a parallel beam geometry. 3600 images were collected spanning a 360° rotation. Custom, in-house software at the APS reconstructed the 3600 radiographs into a 3D greyscale reconstruction, where the greyscale values are a function of the x-ray attenuation in that location.

9.2.2 Nano-CT

For high resolution nano-CT imaging, we obtained images with an UltraXRM-L200 nanoscale X-ray CT system (Carl Zeiss Microscopy, Pleasanton, CA), a lab-scale system with 8 keV X-rays and, in the imaging mode used here, 150 nm resolution (65 nm voxels) and a 65 x 65 μm field of view. For the nano-CT imaging, it was important for samples from SOFC materials be 45 μm or less in diameter (along the beam direction), else the x-ray beam would be over-attenuated, yielding poor reconstructions of the sample interior. In order to prepare a pillar-type sample of this size, we first used a QuikLaze 50ST2 laser micro-mill (ESI, Portland, OR) to cut a roughly 300 x 300 μm square from the anode-supported cell. This piece was then mounted with epoxy to the flat side of a pin, cathode side up. Then, with the same laser micro-mill, all of the cathode material except for a 40 μm pillar was milled away carefully with a lower laser power.

The pillar contained some anode support, AAL, electrolyte, CAL, and cathode current collector, protruding up from the pin and the remaining anode support. It was mounted on the

UltraXRM-L200 nano-CT's rotating sample stage and imaged under monochromatic, 8 keV x-rays. We collected 901 radiograph projection images across 180° of rotation. The nano-CT radiographs were reconstructed using Zeiss' proprietary software, XMReconstructor, to generate a 3D greyscale map of X-ray attenuation. This 3D greyscale image was cropped to a rectangular prism within each active layer for further study, avoiding the outermost 3-4 μm on all sides due to possible edge effects from sample preparation.

9.3 Results and Discussion

9.3.1 3D Image Reconstruction and Segmentation

A virtual 2D slice of the 3D reconstruction from the synchrotron micro-CT scan of the SOFC is shown in Figure 9.1a. In that scan, the cubic voxels were 1 μm (this also means that the pixels in a virtual 2D slice are 1 μm). This voxel size is larger than the expected characteristic length scales for particles and pores in the CAL and AAL, which the nano-CT scan in this work and other works shows to be hundreds of nanometers. Because of this, most voxels located in the active layers of the micro-CT represent 1 μm^3 volumes that were partially filled with a combination of ECP, ICP, and pore. However, the variation in the brightness of these voxels still provides information on the overall distribution of materials.

Some features are fully resolved by the 1 μm voxels, as is evident in Figure 9.1a. For example, there are large, spherical pores in the cathode current collector, and large, irregular pores in the anode support layer, both of which are deliberately introduced to facilitate gas transport. As an example of a particularly large microstructural heterogeneity in the CAL, one can see large (> 5 μm), bright, roughly spherical pieces of LSM throughout the CAL, as well as a few large (> 2 μm) pores. At the interface of AAL and the electrolyte layer, one can also see particularly large pores, likely remaining from when the layers were cast together (though we note again that in this commercial sample, we did not have access to the manufacturing details).

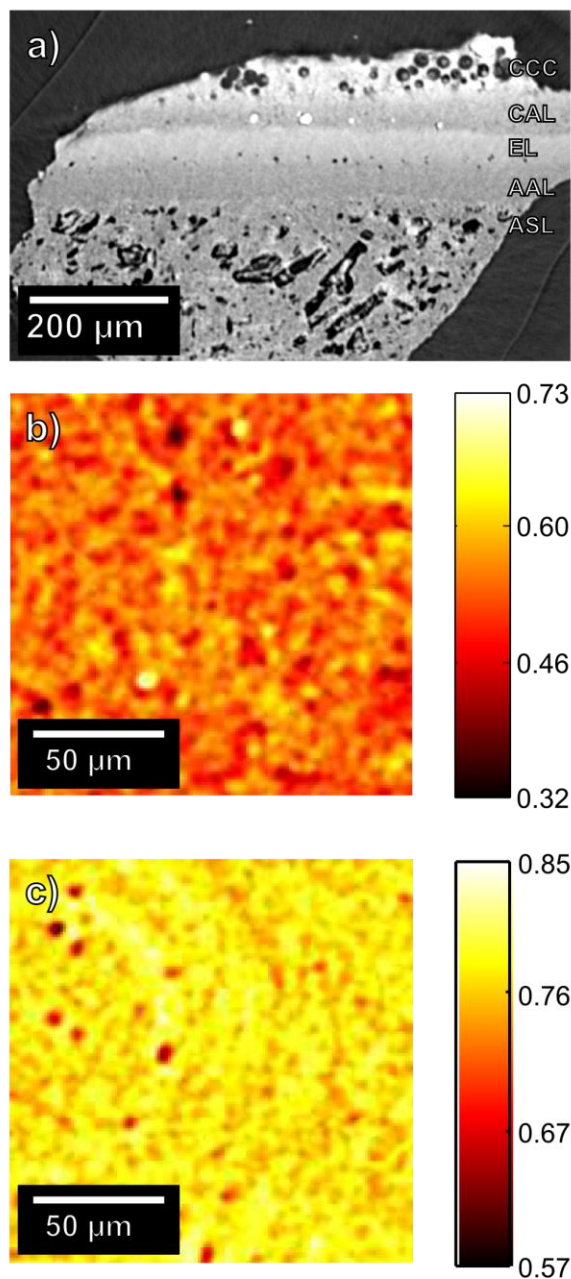


Figure 9.1 Synchrotron micro-CT of cell. a) Virtual 2D slice of 3D synchrotron reconstruction, with cathode current collector (CCC), CAL, electrolyte (EL), anode active layer (AAL), and anode support layer (ASL) labelled. b) 2D intensity plot depicting the integrated greyscale intensity through a $150 \times 150 \mu\text{m}$ sub-volume containing only the CAL, after correcting for linear gradient and normalizing based on Eq. (9.2).

To study the medium/high-frequency heterogeneity of the CAL and AAL independent of particularly heterogeneous, low-frequency features like the large LSM particles and pores, we extracted $150 \times 150 \times 9 \mu\text{m}$ regions of the CAL and the AAL in the synchrotron 3D reconstructed image that were free of these particularly large particles and pores, to the greatest extent possible. For the AAL, the large pores were more distributed, and so the region extracted did still contain a significant amount of large pores. Each $9 \mu\text{m}$ thick subvolume was the thickest rectangular prism that could be extracted from the CAL or AAL without intruding on other layers. Because of the coarser resolution of the synchrotron micro-CT image ($1 \mu\text{m}$ voxels), and because there exists deliberate, engineered variation in phase fraction in the through-thickness direction, the 3D sub-volumes were integrated across the subvolume thicknesses into two-dimensional $150 \times 150 \mu\text{m}$ images according to Eq. (9.1), where $G_{i,j}$ is the greyscale value in the flattened 2D image, $G_{i,j,k}$ is the greyscale value of a given voxel at coordinates i, j, k in the $150 \times 150 \times 9 \mu\text{m}$ region. The unit vector k points in the through-thickness direction.

$$G_{i,j} = \sum_{k=1}^9 G_{i,j,k} \quad (9.1)$$

Both of these projected intensity images initially contained an overall linear gradient from brighter to darker, which may have resulted from the reconstruction algorithm itself or other imaging artifacts. Whatever its origin, our objective is to study local variations in microstructure, rather than whether there is a cross-plane gradient in composition on the length scale of this large region of interest. Considering this, we fit planes to the overall trends in each $150 \times 150 \mu\text{m}$ image and subtracted them, effectively flattening out the linear trends while preserving local variations in each image.

To normalize the arbitrary scale of greyscale intensity in each image, we separately multiplied the greyscale intensity values for pure voxels of the brightest (G_{BP}) and darkest (G_{pore}) phase in each $150 \times 150 \times 9 \mu\text{m}$ 3D dataset by the numbers of voxels integrated across the thickness (9 voxels); these values were used as a range for normalizing the $150 \times 150 \mu\text{m}$ projected image, according to Eq. (9.2).

$$\overline{G}_{i,j} = \frac{G_{i,j} - 9(G_{pore})}{9(G_{BP} - G_{pore})} \quad (9.2)$$

In this arrangement, a value of 0 in one x-y location would correspond to all 9 voxels through the thickness of the layer having the lowest greyscale intensity value in the original 3D data (taken from a large pore). In other words, a value of 0 would mean the entire thickness at that location is one large pore. Similarly, since the maximum value in the normalization scheme corresponds to LSM (the ECP) in the CAL, a value of 1 in the CAL would suggest the entire thickness at that location was LSM. In the AAL, the brightest voxels are YSZ, the ICP, so a value of 1 in the AAL image would indicate the entire thickness at that x-y location was a large particle of YSZ. Such extreme cases of the entire CAL (or AAL) thickness containing all pore or all LSM (or YSZ) do not actually occur in the regions we studied. Using this normalization scheme, the smallest and largest values present in the CAL's 150 x 150 μm flattened image were 0.32 and 0.73, as shown in Figure 9.1b, and the mean value of this region was 0.54. The presence in Figure 9.1b of some lower-values regions close to 0.32 suggests that there are locations in the CAL plane where there is little LSM and much YSZ and pore through the thickness of the CAL. Similarly, the existence of higher-values regions close to 0.73 suggests that in some x-y locations, there is significantly more LSM and YSZ than pore through the thickness of the CAL. The slight bias above 0.5 of the 2D image's average, 0.54, suggests that there may overall be more LSM than pore or YSZ, though to accurately assess phase fractions, we must use the higher-resolution nano-CT reconstruction. The smallest and largest values for the AAL image (Figure 9.1c) were 0.57 and 0.85, with a mean value of 0.77, significantly higher overall than the CAL. This suggests an overall phase balance favoring YSZ, the brighter phase; or possibly that the ECP, nickel, appears to bright to X-rays too (though not as bright as YSZ). As with the CAL, the AAL's phase makeup will be clarified by the higher-resolution nano-CT reconstruction.

An example radiograph from the nano-CT scan can be seen in Figure 9.2a. Visible in Figure 9.2a is a large LSM particle, similar to those evident in the synchrotron reconstruction in Figure 9.1a. This represents one of the particularly heterogeneous features in commercial, mass-produced cells - in our observations and in our literature survey, features like this do not appear in research-grade CALs, but are common across multiple commercial samples.

The 3D reconstructions, after being cropped to a rectangular prism as noted in the experimental section, are shown as a virtual 2D slice in Figure 9.2b and d for the CAL and AAL, respectively. We segmented these volumes into the three constituent phases (pore, ICP, and ECP) using a watershed segmentation algorithm in commercial CT image analysis software (Avizo Fire, FEI, Hillsboro, OR). At the interfaces between brightest and darkest (pore) phases, the resolution limit of the 3D imaging caused the segmentation to yield a false ~2 voxel thick film of the intermediate brightness phase (ICP in the CAL, ECP in the AAL) between the darkest phase (pore) and the brightest phase (ECP in the CAL, ICP in the AAL). The film itself is below the resolution limit of the instrument, i.e. the large-field-of-view imaging mode used in the nano-CT by optic limit cannot distinguish features that small, further supporting the notion that it is an artifact of segmentation. Joos et al²⁹ reported a similar issue. We used image processing to remove this artifact by sequentially dilating the pore phase, then the brightest phase, and then the intermediate phase. The magnitude of the dilation was two 65 nm voxels (130 nm total), which is equivalent to the resolution limit of the nano-CT instrument in the large-field-of-view imaging mode. Virtual 2D slices of the resulting segmented images are shown in Figure 9.2c and e for the CAL and AAL, respectively. The final segmented volumes were 13.6 x 19.8 x 19.4 μm for the CAL, and 26.3 x 24.8 x 15.7 μm for the AAL.

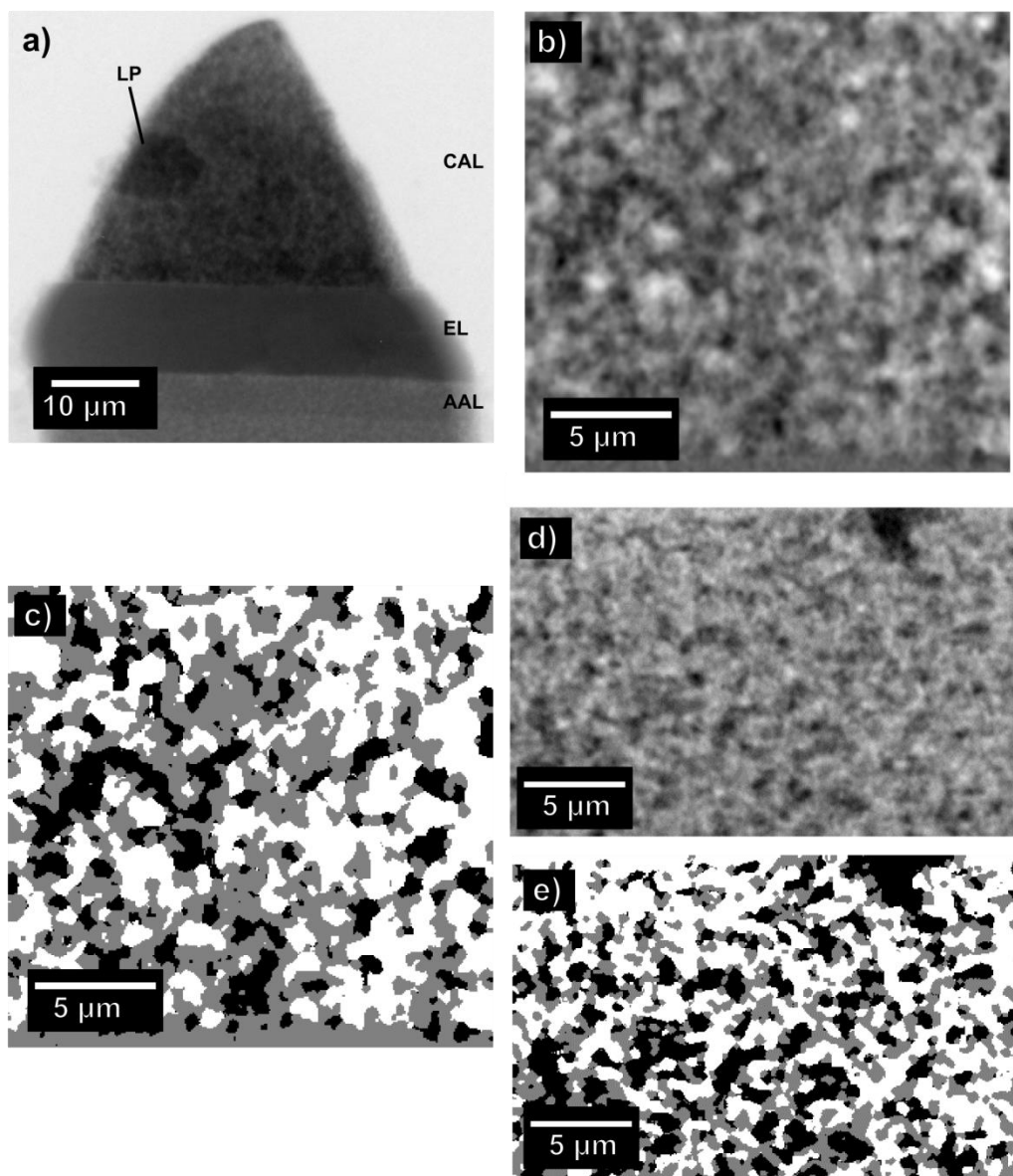


Figure 9.2 Nano-CT images. a) Radiograph of sample pillar, with CAL, electrolyte (EL), and AAL labelled, as well as a considerably large particle (LP) of LSM. From the 3D nano-CT reconstruction of the LSM-YSZ CAL, greyscale (b) and segmented (c) virtual 2D slices, with electrolyte situated at bottom (in segmented version, LSM is white, YSZ is grey, and pore is black). From the same reconstruction, the AAL's greyscale (d) and segmented (e) virtual 2D slices, with electrolyte situated towards the top (in segmented version, nickel is grey and YSZ is white).

One might observe in Figure 9.2 that some small features in the greyscale virtual slices are not evident in the equivalent segmented virtual slice. This is because of the watershed

segmentation algorithm (which takes into account not only greyscale intensity but also gradient) and the dilation-erosion artifact removal procedure, together with the 3D nature of the data. When a greyscale feature seems to be missing from the equivalent segmented 2D slice, that slice is usually the edge of that feature in the dimension not shown in the 2D slice. An adjacent segmented 2D virtual slice will generally contain an element of the apparently missing feature, and the adjacent slice in the opposite direction will show that feature to have ended. For example, in the case of an ECP-pore boundary in the CAL, a greyscale feature in question may have initially been segmented as a false layer of ICP that was successfully removed by the dilation-erosion artifact removal procedure. In short, the manner of segmentation and clean-up means that there is not always an exact mapping from greyscale value to segmented phase on a slice-by-slice basis, but this method provides a more meaningful representation of the cell's actual microstructure than simple greyscale threshold segmentation.

Following segmentation, we developed and used custom codes in MATLAB (Mathworks, Natick, MA) to locate the 3D coordinates of TPBs in each electrode. The program located and stored, in 3D space, vertices between voxels that had at least one immediate neighbor of each phase type (pore, ICP, and ECP). It then connected orthogonally adjacent vertices into contiguous paths. To provide a more accurate measure of length, the code up-sampled those paths to a higher resolution, and applied a 3D Gaussian kernel to the up-sampled paths to turn jagged, orthogonal TPBs into smooth, more physically representative ones. The standard deviation of the Gaussian kernel was set to 65 nm – twice this value represents the smallest distinct feature the nano-CT can resolve in this mode. Figure 9.3a shows an example of one such smoothed TPB path overlaid on the original vertices based path. Figure 9.3b shows 3D renderings of the CAL's and AAL's segmented phases and their TPBs, with a corner cut out to show some of the TPBs in 3D space. The global TPB density was calculated as total TPB length divided by total segmented volume, with the bottom few microns (containing only the electrolyte layer) being excluded from the total volume in the quotient. Phase fractions and phase-phase interfacial surface areas were also calculated using MATLAB, with the latter being calculated using MATLAB's isosurface patching algorithm. Phase fractions, TPB densities, and surface areas per unit volume (i.e. surface area divided by the total segmented volume) are summarized

in Table 9.1. Notably, the TPB density in the AAL is significantly higher than in the CAL. All values are in the correct range compared to literature values.²⁴

Table 9.1: TPB Densities and Phase Fractions from Segmented Nano-CT Data

	CAL	AAL
Image size [μm^3]	5,224	10,024
TPB density [μm^{-2}]	3.1	5.7
ECP fraction	43%	29%
ICP fraction	38%	43%
Pore fraction	19%	27%
Volumetric ECP-ICP surface area [μm^{-1}]	1.33	1.36
Volumetric ECP-Pore surface area [μm^{-1}]	0.31	1.03
Volumetric ICP-Pore surface area [μm^{-1}]	0.93	0.76

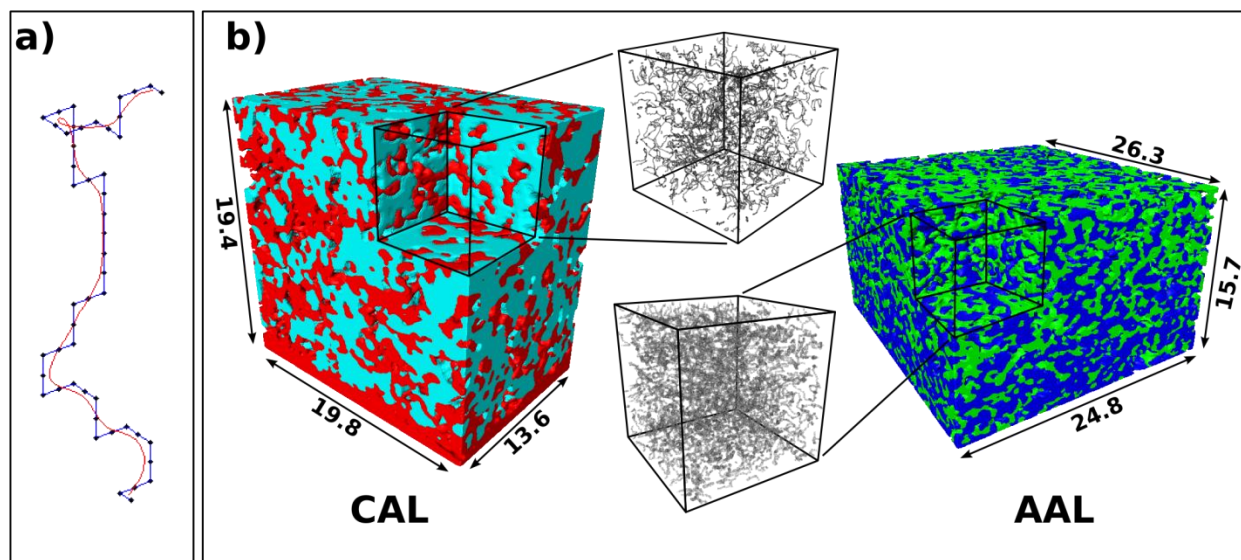


Figure 9.3 Determination of triple phase boundaries. a) Example of TPB vertices (black dots), orthogonal path connections (blue lines), and a final smoothed TPB curve (red curve) in 3D space. The orthogonal distance between each vertex is 32.5 nm (half a voxel). b) 3D renderings of CAL and AAL (dimensions shown in μm), each with a $(6.5 \mu\text{m})^3$ cube removed and the equivalent cloud of TPB curves shown for the cut-out volume. In 3D rendering of the CAL, red is LSM, light blue is YSZ, and pores are transparent. In AAL, dark blue is YSZ, green is Ni, and pores are transparent. The TPB densities for the specific cut-out sub-volumes shown here were $3.4 \mu\text{m}^{-2}$ and $5.6 \mu\text{m}^{-2}$ for the CAL and AAL, respectively.

9.3.2 Characterization of Heterogeneity

In order to study the heterogeneity of the microstructures of the two different electrodes, we developed a custom MATLAB code to simulate the acquisition of multiple smaller images out of the larger image available to us, similar to the analysis Laurencin et al. performed on the porous Ni anode support layer of an SOFC.^{21,22} Our code varied the size of the smaller sub-image to be extracted. For each sub-image size, it extracted as many non-overlapping sub-images as possible from the whole volume. Whatever metric of interest was being studied (phase fraction or local TPB density), the mean value of that metric was logged for each sub-image. We then quantified a 90% confidence interval (using a two-tailed student T distribution) that captures the variability of a given sub-image size within the larger image of fixed size. It is worth noting that, for these sub-image heterogeneity analyses, the largest sub-image to be studied

cannot be as large as the whole reconstructed volume. This is because more than one sub-image must be placed in order to characterize the variability.

9.3.2.1 Phase Fraction in Synchrotron Micro-CT Image

For the synchrotron micro-CT image, the 2D maps of integrated greyscale intensity shown in Figure 9.1b-c were subjected to heterogeneity studies where non-overlapping 2D square sub-images were placed throughout the larger image, in the manner described above in section 9.3.2. Greyscale intensity was used here as a proxy for phase fraction, since the greyscale intensity in the reconstruction is a function of the x-ray attenuation, which in turn depends on composition within that voxel. The heterogeneity calculated in this approach will be slightly under-estimated because the large (1 μm) voxels generally contained more than one phase based on our high resolution results, effectively smearing the phases together to some extent and reducing heterogeneity, and also because the greyscale intensities were those from integrating across the thickness of the layer.

For each square sub-image size, the mean greyscale intensity was stored. After all possible sub-images of that size had been placed, we calculated the variability among those mean greyscale intensity values, before moving on to the next sub-image size to be studied. Figure 9.4a shows the resulting quantification of x-y variation of greyscale intensity for both the CAL and the AAL. For both layers, the plot illustrates a rapid drop from 13% to 4% variability as the square sub-image size grows from 2 to 20 μm , followed by a more gradual decline in the 30-50 μm range. The largest sub-image size of 75 μm had only 4 sub-images to sample; even with the accordingly high Student-T multiplier, the variability here is close to 1% of the mean. At sizes above roughly 20 μm , the variability is low, and pushing to larger image sizes provides diminishing returns in terms of variability. This suggests that a sufficiently large area to study is one above 20x20 μm in either layer. The AAL has a slightly lower error at nearly all sizes, suggesting that it could be less heterogeneous (and have a smaller representative volume) than the CAL. The AAL's curve does slightly cross above the CAL's curve at only the largest sub-image size. We attribute this non-systematic behavior to the low number of 75 x 75 μm sub-images (four) that could be extracted from each whole 150 x 150 μm image. These results come from the 2D variability in integrated greyscale. In the next section, we use higher resolution

nano-CT to examine in more detail the 3D variability in segmented phase fraction and TPB density.

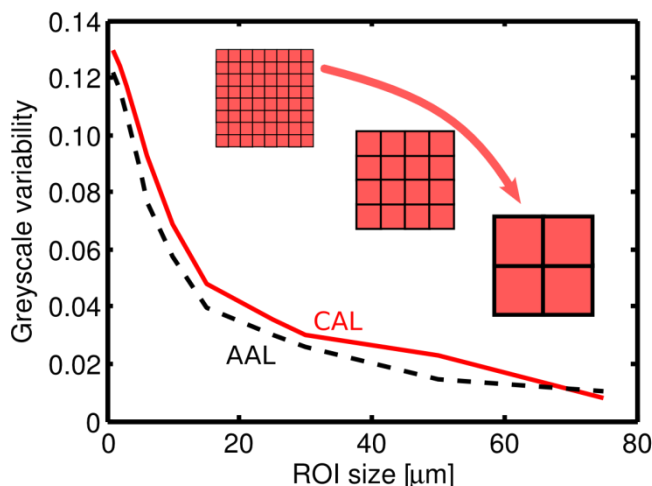


Figure 9.4 2D variability of greyscale intensity (x-ray attenuation) in synchrotron image of CAL and AAL, expressed as 90% confidence intervals based on two-tailed Student-T distribution.

9.3.2.2 Phase Fraction and TPB Density in Nano-CT Images

We performed similar analyses on the segmented nano-CT reconstructions of the CAL and AAL. Because of the more finely resolved 3D structure, we were able to place 3D, cubic sub-images, instead of 2D squares. For each sub-image of a given size, the three phases' phase fractions (the volume occupied by that phase in that sub-image, divided by the volume of that sub-image) was calculated. Once all possible sub-images of that size had been placed, the variability was computed, and the code moved on to the next size of sub-image. This analysis was performed based on phase fractions for each of the three phases. For both the CAL and the AAL, the three phases within each given sample yielded fairly similar curves. In Figure 9.5a we present variability curves for each phase in each layer (inset), and the averaged phase fraction variability for each layer, computed as the even average between the three possible phase-curves in that layer. (Note that the alternate approach of averaging the three separate phase curves

weighted by phase fraction had little impact on the resulting averaged curve.) The average curves show a 20% phase fraction variability in the CAL around sub-image sizes of $(8 \mu\text{m})^3$, with a flattening of the curve suggesting diminishing returns with larger volumes (we attribute the very slight rise on the right-end of the CAL curve to the student-T multiplier, as there were few samples at the largest volume). In contrast, the AAL drops more quickly to 10% close to $(6 \mu\text{m})^3$, before adopting a more gradual slope that, again, suggests diminishing returns at larger volumes. The inset shows that the most heterogeneous phase fraction in the CAL was the ECP (LSM), which is in line with earlier observations that the CAL's overall ECP phase fraction is high, and that it contains large ECP features like the large particle in Figure 9.2a.

In the nano-CT images, we employed the same approach to study variation in TPB density. That is, for each cubic sub-image placed, the TPB density in that sub-image was logged, and then the variability computed. The results of this analysis are shown in Figure 9.5b. Note that cropping out the large LSM particle from the CAL (visible in Figure 9.2a-c) did not significantly affect the results shown in Figure 9.5. The results shown here include the large particle. Similar to Figure 9.5a, the TPB density variability for the AAL drops off quickly to around 10% at a volume of $(6 \mu\text{m})^3$, whereas that of the CAL trails off more gradually, maintaining a higher value above 20% out to the highest sub-image size studied here of $(10 \mu\text{m})^3$.

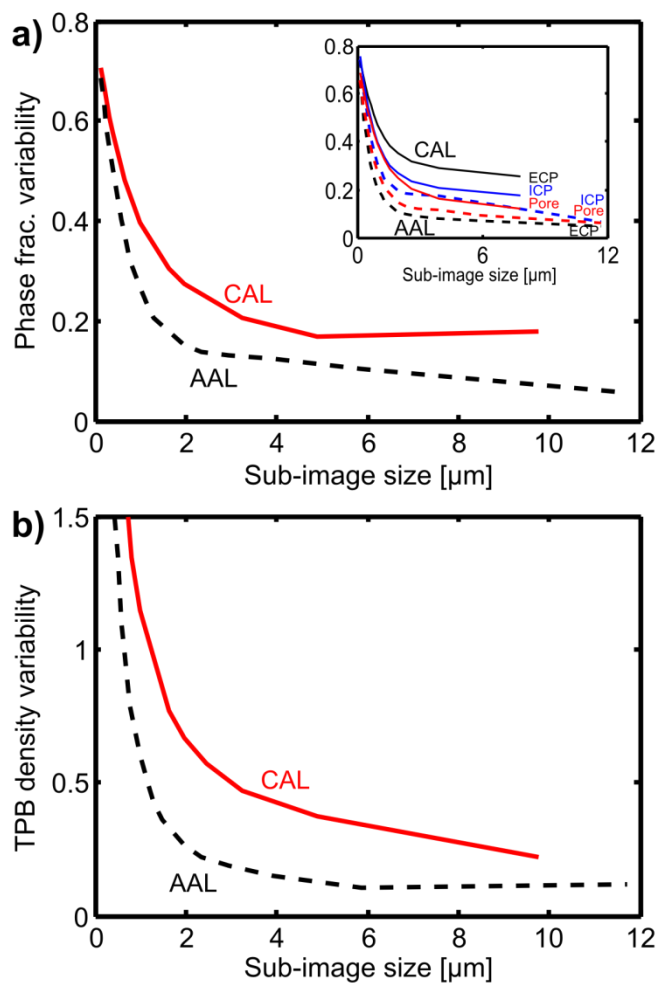


Figure 9.5 a) 3D variability of phase fraction based on size of placed sub-images. Curves shown are average variability for all three phases' volume fractions in that layer (shown separately in inset). b) 3D variability of TPB density based on size of placed sub-images. Both (a) and (b) are expressed as 90% confidence intervals based on a two-tailed Student-T distribution.

Because of the multiple metrics of interest and imaging methods employed in this study, we will not attempt to specify a particular value of variability that is acceptable. However, we can see in Figure 9.4 that the mass-produced CAL exhibits substantial variability in samples below about 20-30 μm . The analyses presented in Figure 9.5 support a similar conclusion, as they show that the CAL maintains a high level of variability for all of the sub-image sizes studied here. This is consistent with observations of mass-produced CALs from a different supplier in the work by Dillon et al.¹⁶ The large size of representative volume suggested here is in contrast with the roughly 5 x 5 x 10 μm representative volume determined by Joos et al.,¹³

which was found using a research-grade, small-batch CAL. On the other hand, the variability in the AAL cell drops off quickly and reaches a comparatively low, steady variability at a $(6\ \mu\text{m})^3$ sub-image size, suggesting that smaller volumes are appropriate for characterizing even commercial AALs.

9.4 Summary

Using 3D imaging techniques of multiple scales, we have shown that the variability in commercial, mass-produced SOFC electrodes can be significant compared to research-grade SOFCs, particularly in the CAL. Many past studies have generated and analyzed 3D microstructural images with volumes of roughly 5 or 10 μm on a side. Based on the foregoing analysis, that volume appears to be sufficient for analyzing the research-grade, house-made cells used in those works. However, if mass-produced cells are to be studied, it becomes important to image larger volumes of $(20\text{-}30\ \mu\text{m})^3$ in order for the analysis to adequately represent the entire CAL. For the AAL, on the other hand, smaller volumes of roughly 6-10 μm on a side appear to be sufficient.

Microstructural heterogeneity may have implications beyond the representativeness of a 3D volume under study. Microstructural parameters like phase fraction and TPB density correlate to cell performance metrics,^{4,9} so their variation through the cell volume may cause maldistribution in reaction rate through the electrode, perhaps diminishing overall performance and accelerating degradation at some sites. Some reaction sites may have significantly longer or more tortuous transport pathways than others in the different phases of the composite electrode; this disparity could cause similar reaction maldistribution. This may be a significant effect in commercially produced SOFC electrodes, given the high level of microstructural heterogeneity we have found in commercial cells.

9.5 References for Chapter 9

1. S. de Souza, *J. Electrochem. Soc.*, **144**, L35 (1997).
2. H. Yokokawa, H. Tu, B. Iwanschitz, and A. Mai, *J. Power Sources*, **182**, 400 (2008).
3. J. R. Wilson et al., *Nat. Mater.*, **5**, 541 (2006).

4. D. Gostovic, J. R. Smith, D. P. Kundinger, K. S. Jones, and E. D. Wachsman, *Electrochem. Solid-State Lett.*, **10**, B214 (2007).
5. J. R. Wilson et al., *Electrochem. commun.*, **11**, 1052 (2009).
6. H. Iwai et al., *J. Power Sources*, **195**, 955 (2010).
7. T. Matsui, R. Kishida, J.-Y. Kim, H. Muroyama, and K. Eguchi, *J. Electrochem. Soc.*, **157**, B776 (2010).
8. T. Matsui et al., *Solid State Ionics*, **225**, 50 (2012).
9. J. S. Cronin, J. R. Wilson, and S. a. Barnett, *J. Power Sources*, **196**, 2640 (2011).
10. M. Kishimoto, H. Iwai, M. Saito, and H. Yoshida, *J. Power Sources*, **196**, 4555 (2011).
11. K. Matsuzaki, N. Shikazono, and N. Kasagi, *J. Power Sources*, **196**, 3073 (2011).
12. D. Kanno, N. Shikazono, N. Takagi, K. Matsuzaki, and N. Kasagi, *Electrochim. Acta*, **56**, 4015 (2011).
13. J. Joos, M. Ender, T. Carraro, A. Weber, and E. Ivers-Tiffée, in *Electrochimica Acta.*, vol. 82, p. 268–276, Elsevier Ltd (2012).
14. P. S. Jørgensen, K. Yakal-Kremiski, J. Wilson, J. R. Bowen, and S. Barnett, *J. Power Sources*, **261**, 198 (2014).
15. G. J. Nelson et al., *Electrochem. commun.*, **13**, 586 (2011).
16. S. J. Dillon et al., *J. Am. Ceram. Soc.*, **94**, 4045 (2011).
17. A. Tkachuk et al., *Zeitschrift fur Krist.*, **222**, 650 (2007).
18. S. H. Lau et al., *J. Phys. Conf. Ser.*, **152**, 012059 (2009).
19. K. N. Grew et al., *J. Electrochem. Soc.*, **157**, B783 (2010).
20. P. R. Shearing et al., *Electrochem. commun.*, **12**, 1021 (2010).
21. J. Laurencin et al., *J. Power Sources*, **198**, 182 (2012).
22. J. Villanova et al., *J. Power Sources*, **243**, 841 (2013).
23. Y. C. Karen Chen-Wiegart et al., *J. Power Sources*, **218**, 348 (2012).
24. J. S. Cronin, Y. K. Chen-Wiegart, J. Wang, and S. a. Barnett, *J. Power Sources*, **233**, 174 (2013).
25. Y. Guan et al., *Mater. Express*, **3**, 166 (2013).
26. M. E. Lynch et al., *Nano Energy*, **2**, 105 (2013).
27. W. M. Harris and W. K. S. Chiu, *J. Power Sources*, **282**, 622 (2015).

28. B. Rüger, J. Joos, A. Weber, T. Carraro, and E. Ivers-Tiffée, *ECS Trans.*, **25**, 1211 (2009).
29. J. Joos, M. Ender, I. Rotscholl, N. H. Menzler, and E. Ivers-Tiffée, *J. Power Sources*, **246**, 819 (2014).

10 Conclusions, Contributions, and Future Directions

The primary focus of this dissertation was oxygen transport resistance in various components of a PEFC cathode. We made in-situ measurements using various types of oxygen microsensors in an operating PEFC to characterize oxygen transport resistances in the DM and the CL pores, and performed an ex-situ microscale x-ray CT characterization of the DM to aid in interpreting the results. Using 50 nm resolution nanoscale x-ray CT, we examined the 3D morphology of a PEFC's CL, which lent further insight into the oxygen transport characteristics of that layer's pores, and allowed us to improve upon the agglomerate-based approach to PEFC performance modelling. We also used an ex-situ approach to determine whether an additional local O₂ transport resistance in Nafion exists if there is no Pt|Nafion interface. Finally, we combined all of these findings into a 0-D PEFC performance model that allowed us to examine the contributions of each separate source of mass transport resistance. In short, what we found was that the DM is the dominant resistance in through-plane oxygen transport, with an R_{O_2} value of approximately 65 s/m in the absence of liquid water. Considering this, further studying and mitigating oxygen transport resistance in the DM should be a focus of future PEFC research.

The second-most significant oxygen resistance is the local Pt|Nafion-level resistance, which we estimate as 800 s/m (nominally a higher value than $R_{O_2,DM}$ because $R_{O_2,local}$ exists many times in parallel, or in other words, across a larger area according to the CL's Pt roughness factor). We also found the local Pt|Nafion-level resistance does not appear to exist in the absence of a Pt|Nafion interface – in other words, it is not a product of the Nafion|gas interface or of a nanoscale-versus-bulk-diffusion distinction. It appears to arise from the interface between the energized Pt catalyst and the Nafion ionomer film that surrounds it. Industry groups consider this local resistance to be one of the largest hurdles to PEFC commercialization, and so determining what causes it (or what doesn't) is a crucial contribution to PEFC research. A critical direction for PEFC research in the future should be determining the mechanism of this resistance, and how it can be mitigated or eliminated. One proposed mechanism for this resistance at the Pt|Nafion interface is the acidic side-groups of the Nafion adsorbing to the electrified Pt interface and blocking oxygen transport locally. If this is the mechanism, mitigating this resistance will likely

involve changing what ionomer is used as a binder in the CL, perhaps by altering the equivalent weight of Nafion, or by selecting a different compound for the acidic group.

Based on our microstructural characterization using nano-CT, the CL pores themselves in the single-phase case do not present a major resistance, amounting to only about 3 s/m (compared to 65 s/m in the DM). However, if liquid water floods the catalyst layer pores, their oxygen transport resistance could increase significantly. Using in-situ measurements with a microstructured electrode scaffold (MES), we measured a possibly flooded CL's pore phase to have an order of magnitude higher resistance than a dry pore phase.

Based also on our nano-CT results, the diffusion of oxygen through the Nafion binder inside of an agglomerate does not present a major barrier, though diffusion through the Nafion binder film that surrounds the agglomerate does. This is in part because we measured agglomerates to be significantly smaller than the 1 μm other agglomerate models assume. With smaller agglomerates, there is less internal Nafion for the oxygen to diffuse through, whereas there is the same amount of Nafion film surrounding the agglomerate.

In the process of analyzing through-plane oxygen transport at multiple levels of the PEFC cathode, we presented many other useful contributions in terms of methods, concepts, and experimental approaches. Using a commercial oxygen microsensor, we mapped out the location of liquid water in the DM in terms of space, PEFC current, and relative humidity. We also mapped out the O_2 resistance in flooded conditions through the DM as a whole, as a function of PEFC current, using a custom thin-film sensor. In both of those works, we presented the method of oxygen flux interrupt for on-the-fly re-calibration during oxygen concentration measurements, solving the issue of O_2 sensor calibration curves that change as a function of time, relative humidity, and temperature.

There is much potential for further work using the commercial oxygen microcapillary sensor, and similar sensors. For example, there are many different manufacturers and lines of DM with widely varying properties. The same oxygen sensor could be used to characterize oxygen transport through different kinds of DM, in-situ. Measuring the oxygen concentration profile and mapping out the location, current-dependence, and RH-dependence of liquid water

flooding in DMs with different PTFE loadings, MPL types, carbon fiber configurations (fiber vs felt vs cloth), thicknesses, and compressions could be highly instructive. Carbon fiber configuration and PTFE loading in particular are likely to have a significant impact on liquid water condensation. With another careful modification to PEFC hardware, the sensor could be inserted into the DM under the land/rib between flow channels, where both water content and oxygen transport are known to be different than under the channel. The addition of a septum to contain gas while still allowing the sensor through would also allow measurements at lower gas flow rates, allowing further study of channel-level losses and the effect of gas stoichiometry on flooding. We initially attempted to use a septum and frequently broke the fragile sensors, but further development of the insertion system or a different septum could make this more feasible. The microcapillary sensor manufacturer (Unisense A/S) also makes similar temperature and H_2 sensors. They could provide useful through-thickness profiles of gas-phase temperature in the cathode or anode DM, and of H_2 in the anode DM. A similar microcapillary RH sensor could also measure the sub-saturated water vapor profile through the DM, lending useful insight into both water and heat removal..

The thin-film sensor developed for the DM|CL interface can be further developed to sense oxygen concentration at multiple points across the plane of the electrode. This dissertation's focus was through-plane transport, but measuring the oxygen transport resistance of the DM at points throughout the plane of the cell is also a worthwhile endeavor that has attracted much research attention. With careful sensor placement, measurements could be made under the land/rib and under the channel. At different locations along the channel, in non-differential cell configurations, this could also lend insight into the channel-level resistance. One advantage of this thin-film sensor is its independence of both PEFC hardware and of MEA and DM type. With further development, a special gasket could be made with multiple such sensors protruding into the PEFC's active area at known locations. Any collaborator with access to PEFC testing hardware and a potentiostat could use such a gasket to characterize channel and DM level oxygen transport in nearly any PEFC configuration.

Further work can be done using the MES developed herein for measuring species concentrations through the thickness of the CL. We suggested several improvements in that

chapter – mainly a shorter time between measurements in each layer, and possibly implementing the oxygen flux interrupt method. The MES is particularly well-suited to studying non-platinum CLs, since they are typically much thicker than conventional CLs (50-100 μm compared to 5-20 μm) and therefore CL through-plane oxygen transport resistance is likely more severe. Additionally, in work not presented here, we investigated the possibility of using the MES to sense other species, such as the chloride ions that are suspected to poison some non-platinum PEFC catalysts. In an ex-situ proof-of-concept study, we successfully sensed Cl^- concentration changes using potentiometric sensing, with the aid of an ion-selective membrane material instead of Nafion to coat the side-walls of the MES.

Within our group, more research continues to be done regarding nano-CT of PEFCs, including studies of PEFC electrodes at various states of degradation, and of non-platinum CLs of various compositions. In this dissertation, we also presented new sample preparation methods for imaging solid oxide fuel cell (SOFC) materials using nano-CT, and microstructural analysis tools including surface area calculation and triple phase boundary mapping. We found the use of nano-CT to be very important in studying commercial SOFC materials when compared with FIB-SEM, considering the large representative volume sizes we determined for these heterogeneous structures, as it can be time-consuming and costly to collect such a large image with FIB-SEM. In the near future, we also plan to use the findings of this representative volume study of SOFC materials to determine, for different SOFC types, whether to use FIB-SEM or nano-CT, or even to use FIB-SEM to study a sub-region of a sample after an initial non-destructive nano-CT scan. Using these methods, and developing further analysis tools involving triple phase boundaries, phase connectivity, and phase transport simulations, we will correlate SOFC microstructure with various states of degradation and different fabrication methods. The methods we develop will heed the features of these microstructures that deviate significantly from the mean, as opposed to focusing on the global mean values, because we suspect that unusual features (e.g. regions particularly rich or poor in triple phase boundary density, or reaction sites located at the end of a particularly reactant tortuous transport path) may be a focal point of overpotential and hence degradation.

The behavior of fuel cells, like other electrochemical devices, is a holistic picture where many processes are closely inter-related. There are both theoretically causative and experimentally correlative relationships between the transport of each reactant and product, fuel cell performance, and performance degradation. In this work we have lent some experimental validation to some of those theoretically causative relationships, provided new experimentally correlative ones as food-for-thought for future research, and eliminated some hypothesized causative relationships from the field. We have provided new approaches to fuel cell modelling, new physical inputs to the models of others, and spatially resolved data for post-hoc validation of models. Finally, we have developed several characterization tools, sensing methods, and sensor architectures with productive futures. Apart from fuel cells, one can modify these methods and concepts and apply them to other electrochemical devices, such as batteries, flow batteries, and electrochemical capacitors. As for polymer electrolyte fuel cells, we recommend moving forward with a particular focus on oxygen transport resistance in the DM, and on the underlying mechanism and possible mitigation strategies for the local Pt|Nafion level oxygen transport resistance.

A. Derivation of Volumetric Current Density in Agglomerate Model

Below, we consider oxygen transport through the ionomer film surrounding a spherical agglomerate, as depicted in Figure A1. Note, this derivation focuses only on the flux through the ionomer film in order to illustrate the derivation of the correct flux expression to use in the overall agglomerate model derivation of Sun et al. [1].

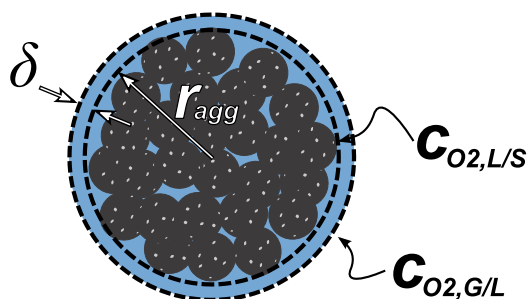


Figure A1: Schematic of a spherical agglomerate.

At steady state, there will not be constant flux along the radial coordinate of the Nafion film. This is because the area changes as we move through the radial coordinate. There will, however, be constant species transport (flux times area, [mol/s]).

Nomenclature	
N_{O_2}'	Oxygen flux
c_{O_2}	Oxygen concentration
r	Radial coordinate, outward
r_{agg}	Radius of agglomerate not incl. film
δ	Thickness of ionomer film
D	Diffusivity of oxygen through ionomer
B	Constant of integration
Subscripts	
L/S	Interface at $r = r_{agg}$
G/L	Gas/Nafion interface at $r = r_{agg} + \delta$

Flux [mol/m²s] at any point r is given by Fick's law:

$$N'_{O_2} = -D \frac{\partial c_{O_2}}{\partial r} \quad (A1)$$

The flux at any radius r times the spherical area at that point should be constant:

$$N'_{O_2} (4\pi r^2) = -D (4\pi r^2) \frac{\partial c_{O_2}}{\partial r} = \text{constant} = B_1 \quad (A2)$$

Separate and integrate Eq. (A2):

$$c_{O_2} = \left(\frac{B_1}{D4\pi} \right) \frac{1}{r} + B_2 \quad (A3)$$

Apply the following boundary conditions to Eq. (A3):

$$\text{BC 1:} \quad \text{at } r = r_{agg} \quad c_{O_2} = c_{L/S}$$

$$\text{BC 2:} \quad \text{at } r = r_{agg} + \delta \quad c_{O_2} = c_{G/L}$$

Using those boundary conditions, solve Eq. (A3) for the constants B_1 and B_2 .

$$B_1 = 4\pi D \frac{(r_{agg} + \delta) r_{agg}}{\delta} (c_{L/S} - c_{G/L}) \quad (A4)$$

$$B_2 = c_{L/S} - \frac{B_1}{4\pi D r_{agg}}$$

Now we return to Eq. (A2) and insert the expression for B_1 .

$$-D \frac{\partial c_{O_2}}{\partial r} = \frac{4\pi D (r_{agg} + \delta) r_{agg}}{4\pi r^2} (c_{L/S} - c_{G/L}) = D \frac{(r_{agg} + \delta) r_{agg}}{r^2} \left(\frac{c_{L/S} - c_{G/L}}{\delta} \right) \quad (A5)$$

In the Thiele method, it is the sphere of active material (here, the sphere bounded by the L/S interface, defined by $r = r_{agg}$) that is considered. For this reason, we will evaluate the flux at the L/S interface, and so we apply $r = r_{agg}$. Substituting the expression from (A5) into Eq. (A1), applying $r = r_{agg}$, we obtain $N'_{O_2,L/S}$.

$$N'_{O_2,L/S} = -D \frac{\partial c_{O_2}}{\partial r} \Big|_{r=r_{agg}} = D \frac{(r_{agg} + \delta) r_{agg}}{r_{agg}^2} \left(\frac{c_{L/S} - c_{G/L}}{\delta} \right) \quad (A6)$$

Simplifying Eq. (A6), we obtain:

$$N'_{O_2,L/S} = D \frac{(r_{agg} + \delta)}{r_{agg}} \left(\frac{c_{L/S} - c_{G/L}}{\delta} \right) \quad (A7)$$

This is similar to Eq. 8 in Sun et al. [1], except that the fraction $(r_{agg} + \delta)/r_{agg}$ is inverted.

Using the Eq. (A6) developed here in place of the version in the work by Sun et al. [1], one can follow through the remainder of Sun and coworkers' derivation to obtain the volumetric current density as it stands in Eq. (4) of our paper (note that in applying the Thiele modulus, the pertinent concentration is that at the surface of the active material, i.e. $c_{L/S}$):

$$j_{ORR} = 4F \frac{P_{O_2}}{H} \left[\frac{1}{E_r k_c f_{agg}} + \frac{r_{agg} \delta}{a_{agg} D (r_{agg} + \delta)} \right]^{-1} \quad (A8)$$

The inverting of the $(r_{agg} + \delta)/r_{agg}$ term has only a minor impact on simulation results, unless the agglomerates are small (order of 100 nm). Some of the agglomerate sizes in the present work are in fact small enough for the effect to be significant, but for the sizes modeled by Sun et al. [1] and many other works, there is little impact on the findings.

Reference for Appendix A:

- [1] W. Sun, B. A. Peppley and K. Karan, *Electrochim. Acta*, **50**, 3359 (2005).